NONLINEAR INVESTIGATION OF OSCILLATIONS IN RADIATING SHOCKWAVES

by

ERIK JASON KEEVER

A DISSERTATION

Presented to the Department of Physics and the
Graduate School of the University of Oregon
in partial fulfillment of the requirements
for the degree of
Doctor of Philosophy

March 2020

DISSERTATION APPROVAL PAGE

Student: Erik Jason Keever

Title: Nonlinear Investigation of Oscillations in Radiating Shockwaves

This dissertation has been accepted and approved in partial fulfillment of the requirements for the Doctor of Philosophy degree in the Physics by:

Gregory Bothun	Chair
James Imamura	Core Member
Jens Noeckel	Core Member
Allen Malony	Institutional Representative

and

Kate Mondloch	Interim Vice Provost and Dean of the Graduate School

Original approval signatures are on file with the University of Oregon Graduate School.

Degree awarded March 2020

DISSERTATION ABSTRACT

Erik Jason Keever

Doctor of Philosophy

Department of Physics

March 2020

Title: Nonlinear Investigation of Oscillations in Radiating Shockwaves

Strong shockwaves are a common phenomenon throughout the universe. Linear analysis indicates that when the postshock gas cools with a volume emission rate $\Lambda \propto \rho^2 T^\theta$ that for many physically realizable values of θ the cooling region should be subject to both one-dimensional ('radial' in the accretion context) and transverse instabilities. The hydrodynamic and numeric theory underlying the GPU-Imogen parallel GPU-accelerated fluid dynamic code is presented. This accelerated code was used to simulate over one thousand combinations of Mach, adiabatic index and radiation law θ to their final nonlinear state in one dimension, which gives a comprehensive dictionary of the expected observable output as a function of the input parameters. The same code was used to examine the fully nonlinear development of transverse instabilities in two dimensions. It is found that the same radial modes expected to dominate most of parameter space, the F and first overtone, suffer their cold zones degenerating into turbulence which shuts down the characteristic large, periodic luminosity fluctuations expected from the one dimensional case.

CURRICULUM VITAE

NAME OF AUTHOR: Erik Jason Keever

GRADUATE AND UNDERGRADUATE SCHOOLS ATTENDED:

University of Oregon, Eugene, OR, USA

DEGREES AWARDED:

Bachelor of Science, Physics, 2009, University of Oregon

AREAS OF SPECIAL INTEREST:

High performance physics programming
Astrophysical simulation

PROFESSIONAL EXPERIENCE:

Graduate Employee, University of Oregon, 2010-2020
Research Associate, Argonne National Laboratory, 2013

GRANTS, AWARDS AND HONORS:

2017 Weiser Senior TA Award
2014 Weiser Senior TA Award

PUBLICATIONS:

"Corrugation Instabilities in Slow MHD Shocks," Imamura, J.N., Ernst, S., Hadley, K., Dumas, W., Hickok, C., & Keever, E. 2010, The Energetic Cosmos: from Suzaku to ASTRO-H. Proceedings of the 3rd Suzaku Conference, 29 June-2 July, 2010, Otaru, Japan. JAXA Special Publication JAXA-SP-09-008E, ISSN 1349-113,Edited by K. Makishima, 312

"Nonaxisymmetric Instabilities in Self-Gravitating Disks: Linear and Quasi-linear Regimes," Hadley, K.Z., Fernandez, P., Imamura, J.N., Keever, E., & Tumblin, R. 2012, in AIP Conf. Proc., 1480, First Stars IV. From Hayashi to the Future," eds. M. Umemura and K. Omukai (Melville,NY: AIP Press), 361

"Nonaxisymmetric Instabilities in Self-Gravitating Disks: Angular Momentum Transport," Tumblin, R., Fernandez, P., Hadley, K.Z., Imamura, J.N., & Keever, E., 2012, in AIP Conf. Proc., 1480, First Stars IV. From Hayashi to the Future, eds. M. Umemura and K. Omukai (Melville,NY: AIP Press), 439

"Nonaxisymmetric Instabilities in Self-gravitating Disks. II Star/Disk Systems," Hadley, K., Fernandez, P., Imamura, J.N., Keever, E., Tumblin, R., & Dumas, W. 2014, Astrophysics and Space Sciences, 353, 191

"Nonaxisymmetric Instabilities in Self-gravitating Disks. III Angular Momentum Transport," Hadley, K., Dumas, W., Imamura, J.N., Keever, E., & Tumblin, R. 2015, Astrophysics and Space Sciences, 359, 10

"Nonaxisymmetric Instabilities and Star-Disk Coupling I. Moderate Mass Disks," Hadley, K.Z., Dumas, W., Imamura, J.N., Keever, E. & Tumblin, R. 2019, Astrophysics and Space Sciences, 364, 119

Imogen: A 3D MHD Code for GPUs, Keever,E. & Imamura, J.N. 2013, in Proc of ACM conference, International Supercomputing Conferene 13, ed. A. Malony, (New York: ACM Pub.), 479

Imamura, J.N., Dumas, W.,Hadley, K. Z., Keever, E., & Tumblin, R. 2015, "Effects of Radiative Cooling on Nonaxisymmetric Instabilities in Self-Gravitating Disks," in 16th American Physical Society meeting, Vol 60 #6 C1.000002

Imamura, J., Dumas, W., Hadley, K.Z., Keever, E. & Tumblin, R. 2016, "Nonaxisymmetric Instabilities Driven by Star/Disk Coupling," in 17th American Physical Society meeting, Vol 61 #7 C1.000004

Tumblin, R., Imamura, J., Dumas, W., Hadley, K., & Keever, E. 2017,
  "Non-Axisymmetric Instabilities in Circumbinary Disks: Giant Planet
  Formation," in 18th American Physical Society meeting, Vol 62 #7
  C2.000002

Dumas, W., Imamura., J., Hadley, K., Tumblin, R., & Keever, E. 2017
  "The effect of radiative cooling on clump formation in self-gravitating
  disks," in 18th American Physical Society, Vol 62 #7 D1.000020

ACKNOWLEDGEMENTS

Thank you to all who supported me for all these years and told me to keep going even when I wanted to give up.

TABLE OF CONTENTS

LIST OF FIGURES

xvii

CHAPTER I

INTRODUCTION

A high performance, parallel, gpu-accelerated general purpose fluid simulation code, GPU-Imogen, is developed. It is used to examine the instability of radiating planar shockwaves with parameterized optically thin cooling in the nonlinear regime for a broad range of astrophysically applicable parameters.

Radiative shockwaves can occur wherever a shock front propagating through a fluid is sufficiently intense to heat the postshock gas enough that the cooling time, measured as the internal energy density divided by the rate of radiative loss, becomes comparable to another relevant timescale. The term is perhaps something of misnomer as the shock front does not, itself, radiate.

They can occur on earth in the early stages of nuclear explosions and in laboratories using lasers to shock-heat materials. In space, they are an important part of the evolution of supernova remnants, coming after the adiabatic Sedov-Taylor phase. They are also found driven ahead of runaway stars with intense solar winds, in both protostellar and compact object accretion columns, and on grand scales in galactic jets. Shock heating followed by radiative loss is also an essential part of protostellar formation.

In many cases, postshock radiation renders otherwise invisible cold cosmic gas directly visible by heating it and driving it to emit detectable radiation, from visible to hard X-rays depending on temperature. Very strong shocks are expected to create a telltale emission from a structure which is much too small to directly resolve (e.g. white dwarf/neutron star accretion), and thereby allow these small scale structures to be probed without planet-sized telescopes.

1
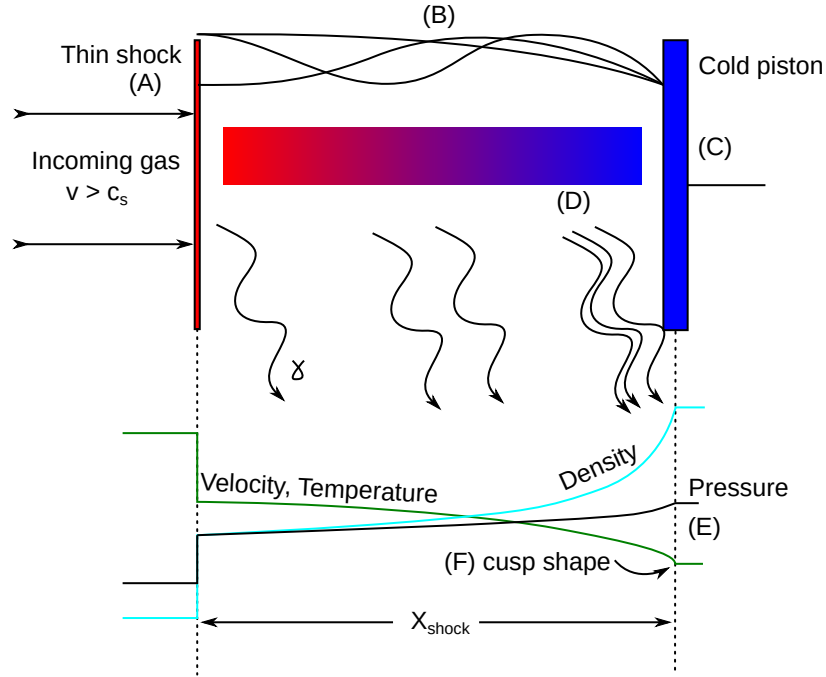
Figure 1. Qualitative depiction of a shock with cooling column ('radiating shock').
A: A thin shock superheats the incoming gas; Thin implies that the mean free
path is much shorter than the cooling length. B: The cooling region between
the shock and the cold layer behaves as an acoustic cavity, with the cold piston
"closed" and the shock front "open", and therefore contains standing modes at
a fundamental wavelength at 4 times the shock height and at odd harmonics. C:
The cold layer drives the shock forward, in the frame that considers the preshock
gas stationary. "Cold" is relative, and may mean either that the radiation rate
drops or that the gas becomes radiatively opaque. D: The volumetric radiation
emission rate Λ, driven by ρ^2, rises rapidly near the cold layer. E: Velocity and
temperature collapse to zero, while density blows up. The competition between ρ
and T contrives to keep pressure relatively constant. F: The shape of the cusps -
zero, finite or infinite slope - depends upon the radiation exponent.

It is realistic to model the radiation rate of a plasma as being proportional to the square of the density and, over restricted temperature ranges, a fixed power of the temperature, with different temperature ranges having very different values (and signs) of temperature exponent. The qualitative structure that results from postshock cooling is depicted graphically in figure 1. On dimensional analysis grounds, we expect that $X_{\mathrm{shock}} \approx v_{\mathrm{post}} t_{\mathrm{cool}}$ with cooling time $t_{\mathrm{cool}} = \epsilon_{\mathrm{int}}/\Lambda \approx \frac{(9/16)\rho_0 v_{\mathrm{in}}^2}{\Lambda_0 \rho_1^2 T_1^\theta}$. In fact, the competition between rising density and dropping temperature contrives to make this dimensional analysis far closer to correct than might be surmised, i.e. the prefactor really is close to one.

Is has long been known that in the strong shock limit, many values of temperature exponent are subject to linear instability of the overstability type. In this work, shocks from weak to strong, spanning the physical range of radiative exponents at three adiabatic indices (5/3, 7/5, 9/7) are tested for radial instabilities in a total of over 1000 fully nonlinear simulations.

Based on the depth of the (relative) luminosity fluctuation, potentially the presence of multiple simultaneous oscillations modes, and ratios of harmonics in the fluctuation it is possible to constrain the potential radiative emission laws, and by comparison of the emission law obtained with the known exponents associated with real cosmic gas, constrain the gas and shock parameters involved.

Two dimensional simulations of planar radiative shocks show that development of transverse structure is likely to greatly surpress spatially unresolved luminosity fluctuations due to development of turbulence in the cold layer. Based on visualization of the nonlinear 2D development, this is because the edge of the cold layer is an acoustic mirror, and just as an optical mirror must be

3

flat to show a coherent reflection, the cold layer boundary must remain something resembling flat in order to maintain coherent oscillation.

This work is organized as follows: In section 2, the theory of fluid dynamics is presented. This is followed in section 3 by the theory of the numeric methods of solving these equations implemented in GPU-Imogen. Section 4 presents a wide range of code verification tests used to confirm the veracity of code generated output. In section 5 the planar shock simulations are described and results from a large bank of 1D simulations are presented. These are followed by results in 2D and finally, some global 3D simulations of stellar bow shocks are presented in which the use of different radiation laws obtains completely different results.

CHAPTER II

THEORY

The theory of conservation equations in the general sense will be introduced, followed by application specifically to the formulation of the Euler equations of fluid dynamics. Key source terms applicable to the Euler equations in an astrophysical context will be introduced. This will provide a foundation for discussion of radiative shocks.

Conservation equations. Consider a closed (classical) volume where the only way for something to enter or leave the volume is by going through its surface if there are no source terms. In this case we would then define the evolution through time of the contents of the box, u in the convention of most literature pertaining to numeric hyperbolic PDEs, via the rate at which u is transported through the surface, defined as the flux $\vec{F}(u)$.

Consider a simply-connected finite volume V, with a boundary surface σ and differential normal surface elements $d\sigma$. There are two choices of orientation for the $d\sigma$ elements. The one in which they are oriented facing out of the volume is adopted; Put another way, the one which yields the sign conventions as in (2.1) below. In this case, a quantity u is described by a conservation equation if its time evolution is described as

$$\partial_t u = -\nabla \cdot \vec{F} \leftrightarrow \frac{d}{dt} \int_V u(x,t) dV = - \int_\sigma \vec{F}(x,t) \cdot \vec{d\sigma} \qquad (2.1)$$

where on the left we have the differential form and on the right the integral formulation. Put in words, the net rate of change of the amount of u within the volume equals minus the net rate at which $\vec{F}$ transports u across the boundary of the volume, which the integral formulation makes clear.

The integral form is applicable to most any "reasonable" volumes/surfaces. They must be orientable (e.g., no Klein bottles). Both V and σ should have integer dimensions such that the Riemann integrals converge upon refinement (e.g., no Koch snowflakes). Though not mandatory as a matter of analysis, numeric problems tend to arise if the aspect ratios of the cells are vastly different from 1 (e.g., no voxels of size 100x1x1 units). And as stated before, the volumes should be simply connected (topologically equivalent to a circle/sphere, e.g. no tori).

Volumes considered in practice are usually geometrically simple: Curvilinear coordinate surfaces (e.g. rectangles/boxes) are common on structured grids. Unstructured choices include tesselating triangles or tetrahedra, or quadrilaterals. Generally speaking, shapes with flat (or at least asymptotically flat) sides.

In GPU-Imogen the conservation form is applied on curvilinear coordinate systems. The integral (2.1) taken in a counterclockwise loop around a square X-T box in one dimension gives

$$\int_{x_0}^{x_1} u(x, t_0)dx - \int_{t_0}^{t_1} F(x_1, t)dt - \int_{x_0}^{x_1} u(x, t_1)dx + \int_{t_0}^{t_1} F(x_0, t)dt = 0. \qquad (2.2)$$

The space integrals are recognizable as averages. If the fluxes F are evaluated at t_0 and changes in them are assumed to be small (they may even be zero), all four integrals can be evaluated and a recognizable equation for the time evolution of the averaged quantity $\bar{u}$ appears:

$$\bar{u}(x, t_1)(x_1 - x_0) = \bar{u}(x, t_0)(x_1 - x_0) + F(x_0, t_0)(t_1 - t_0) - F(x_1, t_0)(t_1 - t_0) \qquad (2.3)$$

is the finite volume formulation of the conservation law in 1D. Replacing differences in x and t with deltas and rearranging slightly yields a more familiar form,

$$\bar{u}(x, t_1) = \bar{u}(x, t_0) - \frac{\Delta t}{\Delta x}\left[F(x_1, t_0) - F(x_0, t_0)\right] \qquad (2.4)$$

The fraction $\Delta t/\Delta x$ is the mesh ratio, sometimes written as λ, and it hints at the self-similarity of solutions to piecewise-constant initial conditions in one dimension. In more spatial dimensions, the resulting equations are

$$\bar{u}(x,y,t_1) = \bar{u}(x,y,t_0) - \frac{\Delta t}{\Delta x}\left[F(x_1,t_0) - F(x_0,t_0)\right] - \frac{\Delta t}{\Delta y}\left[G(y_1,t_0) - G(y_0,t_0)\right]$$

(2.5)

$$\bar{u}(x,y,z,t_1) = \bar{u}(x,y,z,t_0) - \frac{\Delta t}{\Delta x}\left[F(x_1,t_0) - F(x_0,t_0)\right] - \frac{\Delta t}{\Delta y}\left[G(y_1,t_0) - G(y_0,t_0)\right]$$

(2.6)

$$- \frac{\Delta t}{\Delta z}\left[H(z_1,t_0) - H(z_0,t_0)\right]$$

While these equations are correct and mathematically convergent for infinitesimal spacings Δx_i and Δt, they are as written only of first order space and time accuracy for finite spacings and appreciable further development is required to arrive at a practically useful scheme.

The chief defect present in (2.4) as written is that it is an application of Euler's Method, which is only of first order time accuracy. Nonetheless, it is the building block for higher order methods. Its higher order compatriots have a further serious defect originating from the assumption that the fluxes are constant, which near corners and edges they are not. This issue is depicted schematically in figure 2 and is (with specific attention to the Euler equations) is considered in detail in Vides, Nkonga, and Audit (2015).

As an illustrative example, consider constant speed advection. Suppose some scalar quantity ϕ is moving at constant speed c everywhere along the line. This is 1D constant velocity linear advection and is a model problem in first-order hyperbolic PDEs. It provides similar difficulties with numeric differencing stability and function reconstruction as the Euler equations while removing the complex
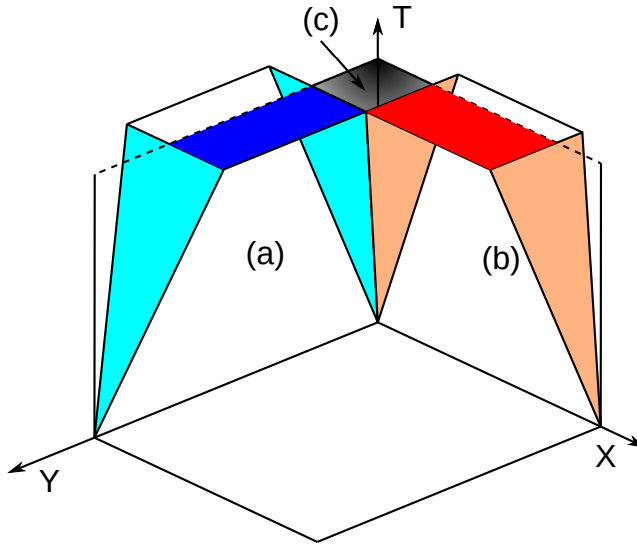
Figure 2. A depiction of the evolution of a corner of a two dimensional Riemann Problem through time. Referring to equation (2.5), the (a) region's flux is initially specified by $F(x_0, t_0)$ and the (b) region's flux by $G(y_0, t_0)$ but the region in which the fluxes determined by these 1D fans is valid shrinks as the corner interaction region (c) grows. Thus the kind of discretization described here, naively applied to multi-dimensional problems, is only first order accurate.
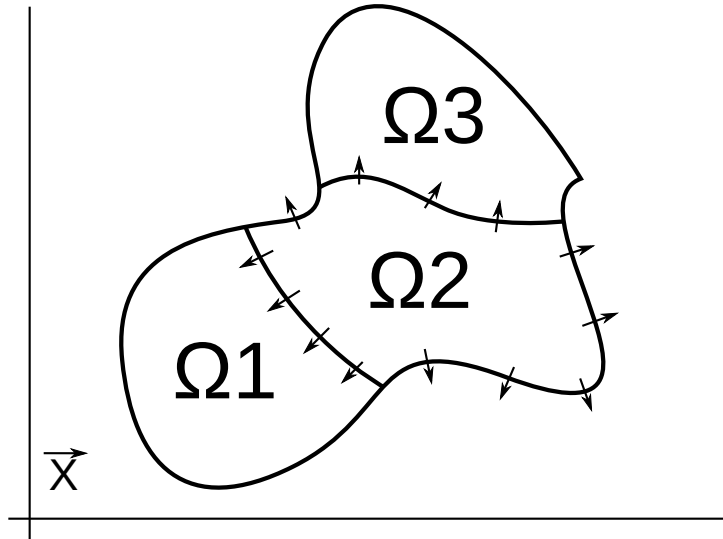
Figure 3. A depiction of the finite volume integral transform in (2.1) in two dimensions, showing three volumes with the outward normal ∂V_2 marked by arrows. Local conservation is clearly acheived because anything leaving V_2 immediately enters another volume.

flux calculation.

$$\partial_t \phi = -c \partial_x \phi \tag{2.7}$$

It can be seen by inspection that the solution, if formulated as an initial value problem, is

$$\phi(x, t) = \phi_0(x - ct, 0) \tag{2.8}$$

and as a conservation equation we can see that the flux equation is

$$F(\phi) = c\phi \tag{2.9}$$

Now let us take our volume to be an interval $[x_0, x_1]$ on the real number line, with boundaries at the endpoints of the interval. The advection equation (2.7) then reduces through the form of (2.4) to

$$\frac{d}{dt} \bar{\phi}(x, t) dx = -c\phi(x_1, t) + c\phi(x_0, t) \tag{2.10}$$

The rate of change ϕ on the interval is the rate at which it enters at point x_0 minus the rate at which it leaves at x_1 (in the view that $c > 0$). If we consider adjacent boxes,

$$\frac{d}{dt} \bar{\phi}_{01} = \frac{d}{dt} \int_{x_0}^{x_1} \phi(x, t) dx = -c\phi(x_1, t) + c\phi(x_0, t) \tag{2.11}$$

$$\frac{d}{dt} \bar{\phi}_{12} = \frac{d}{dt} \int_{x_1}^{x_2} \phi(x, t) dx = -c\phi(x_2, t) + c\phi(x_1, t) \tag{2.12}$$

with the ordering $x_0 < x_1 < x_2$, it is obvious why these are conservation equations. At any instant, whatever is exiting the right side of box 01 is entering box 12.

For conservation to be easily acheived with finite volumes, we note that simply connected finite element subdomains must *exactly* span the domain with neither gaps nor double-counting; Such a spanning is inherently achieved when curvilinear coordinate surfaces are subdivided (stacking line segments, squares or cubes). With less structured grids the subject of mesh generation is its own

substantial subject, although the exact-spanning property still guarantees identical conservation.

We note here the distinction between approximate and exact (identical) conservation. Given that (2.7) is conservative, an approximately conservative method would conserve the total amount of ϕ up to *truncation error*, the order of accuracy of the method. An exactly conservative method will conserve it perfectly (in real-valued arithmetic) and to the level of float point round off (in actual computer arithmetic).

Differential vs integral formulation. The key difference of interest between the integral and differential formulations of (2.1) is their ability to deal with solutions containing discontinuities. Differential formulations work fine with equations that have strong solutions. This is because a strong solution says that $u(x,t)$ exists everywhere in the domain of interest, and thus writing down u and its derivatives at all points does not present a problem. However, transport equations are infamous for generating solutions in which the solution becomes multivalued and discontinuities develop.

When a discontinuity exists, a strong solution is no longer possible because u cannot be written down at the locatin of the discontinuity. Here, weak solutions are necessary. They allow us to write down the solution arbitrarily close to the discontinuity and effectively "seal it off" as in e.g. linear analysis of a shock wave in which the solution is smooth almost everywhere except at the location of the shock.

While this is tractable for analyzing known geometries like the above plane shock, the scaling issues involved with deciding where and when to do this in a modern simulation that may contain billions of elements, or more, are self evident.

Moreover, when dealing with finite differences as on a computational grid rather than with infinitesimal differentials as in calculus, the solution being approximated need not actually be discontinuous. Spatial structure smaller than can be resolved is effectively the same: if a variable jumps from 1 to 2, what does it matter if the true solution does it in the space of 1/100 of a cell, or 1/2 of a cell? Neither is resolvable and are effectively discontinuous.

By using the integral formulation, the cripping inability to write down what $u(x, t)$ is at a discontinuity is avoided. The transform effectively "upgrades" the level of smoothness of the system by one order, in this case from not continuous to $\mathbf{C}^0$. Consider e.g. if a shockwave propagates into a box from the left, moving right. While point values jump instantly, the value of any box-averaged quantity q is Lipschitz continuous (with the Lipschitz constant equal to the magnitude of the jump in q times the speed of the shock divided by the size of the box).

An important feature of the integral formulation is the need to remember what the variables now represent; that is,

$$\bar{u}_V = \int_V u d\vec{x}. \tag{2.13}$$

As presaged in (2.11), "the" value of u in a domain is the integral average over the domain of the point values $u(x, t)$. This is why weak solutions are needed to deal with idealized transport equations (which are infamous for not only supporting the existence of discontinuous solutions, but creating discontinuities in initially smooth data in finite time). The integration over finite volumes "upgrades" the smoothness of the system from the discontinuous $u(x, t)$ to the $\mathbb{C}^0$ value $\bar{u}_V$. Thus the need to attempt to know point values of u is sidestepped.
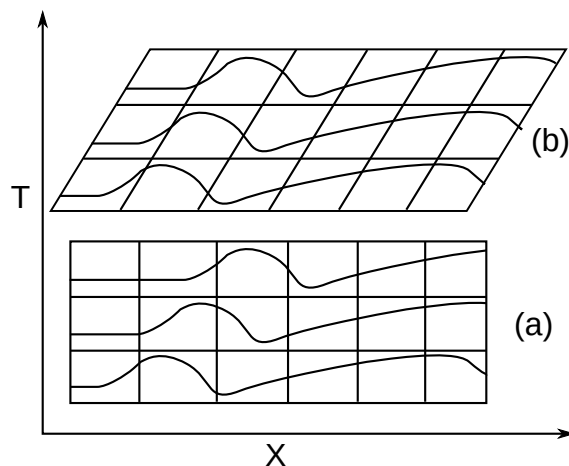
Figure 4. Depiction of an Eulerian grid, through which a wave is traveling (a). In the Lagrangian grid (b) which is translating in the lab frame, the speed of the wave relative to the grid will appear to be much smaller.

While there will follow many references to "u at x" it must always be kept in mind now that what this really means is "the average values of u over the volume surrounding x."

Choice of frame. In writing down (2.7) we have implicitly chosen an Eulerian formulation for the conservation law. The subdomains have (presumably) been chosen once, and we now sit on the space-time lattice with our notepads watching u move from one to another.

An Eulerian frame refers to one in which the coordinates at which the solution is evaluated remain stationary while the solution "moves through" them. It is often identified with the partial derivatives ∂_x and ∂_t. A Lagrangian frame (also possibly called a material or comoving frame, depending on who one talks to) is one which the solution points move with the flow, and is identified with comoving derivative operators, like $d_t = \partial_t + \vec{c} \cdot \nabla$ for physical flows.

The Eulerian formulation is exceedingly convenient in the following sense: Having chosen a set of domains within which to track the evolution of ϕ, we

are done setting up the problem immediately. This is because each domain V_i introduces both a new variable, $\bar{u}_i$, and a new equation constraining the evolution of $\bar{u}_i$: the (discretized) governing differential equation is all that is required to completely define the solution and the simulation is "ready to go."

The Lagrangian frame (of which the Eulerian frame is a restricted particular case) considers that the domain boundaries may move: that V_i are not time-independent. This provides formidable advantage in representing certain problems: Features which move, grow or shrink can be followed by the simulation domain as a whole or by parts of it. If ϕ contains both large and very small features, we may track the very small features in ϕ without the enormous burden of over-representing the large features with (unnecessary) equal fidelity.

The downside of the Lagrangian frame is that of considerably increased complexity because the finite domains used to construct the integral equations are themselves changing. By allowing d/dt to act on both ϕ and V_i we now have multiple variables added for each domain, but the governing (physical) differential equations still only give enough constraints for an Eulerian solution and so new governing equations must be invented to control the evolution of the frame itself.

In one dimension, the problem is highly tractable because ordering subdomains in one spatial dimension is trivial - in fact it is impossible for them to become disordered. However, ordering is only part of the problem. Equations are necessary to describe how cell boundaries move, and to decide when to refine (or unrefine) the grid in an area.

In more than one spatial dimension, the natural ordering of domains is lost. The management of Lagrangian grids is a whole subject in and of itself: Grid

generation, grid detangling, rezoning, remapping, and adaptive mesh refinement (AMR) are each formidable fields of study by themselves.

In view of these complexities, the work being built upon and the already formidable scale of the project undertaken the Eulerian frame is used (with some very limited relaxations wherein the grid as a whole moves or rotates).

Gas dynamic theory.

Fluid equations. In light of having (2.7) to describe constant velocity advection, suppose we consider ϕ as the density of mass in a fluid, ρ. In general fluids obviously do not flow with constant velocity so we would be forced to replace the constant c with $v(x,t)$, the velocity of the fluid at a given point in space and time. This leads to the continuity equation in one dimension,

$$\partial_t \rho = -\partial_x(\rho v) \tag{2.14}$$

Where for space's sake we are dropping the explicit reference to the space-time dependence of all the variables.

Having solved one problem - how to evolve the density variable - another has been created in the question of how to evolve the velocity variable. Matters can be improved by considering instead the momentum density $p = \rho v$. Thinking of this as pinned to parcels of fluid, we may argue for it to be transported around in the same manner by which we arrived at conservation of mass, such that

$$\partial_t p = -\partial_x(pv) = -\partial_x(\rho vv) \tag{2.15}$$

If a pattern appears to be emerging it's because one is: The above equations represent the first two terms in the expansion of the kinetic (Boltzmann) equation in powers of velocity. And the problem is already evident: The expansion is not closed. For each moment of the kinetic equation that is expanded in powers of

14

velocity, the Nth moment's evolution is coupled to the (N+1)th's moment. And not by an object of the same size, but by a tensor one rank higher.

The process of achieving closure, described in great detail in the classic monograph of Chapman & Enskog Chapman, Cowling, and Park (1962), provides a solution. Any remotely realistic collision operator, it turns out, generates a predictable pattern in velocity space. By keeping certain moments and contractions of the 3rd rank ρvvv object and assuming that the distance a particle can travel through the fluid before scattering $\lambda << L$ for a length scale of interest L, we can write an evolution equation for a scalar called the total energy density E in terms of ρ, p and E. This yields a closed set of equations, which when all non-ideal terms are dropped become the ideal fluid equations:

$$\partial_t \rho + \partial_x (\rho v) \qquad\qquad\qquad = 0 \qquad\qquad (2.16)$$

$$\partial_t (\rho v) + \partial_x (\rho vv + P) \qquad\qquad\qquad = 0 \qquad\qquad (2.17)$$

$$\partial_t E + \partial_x \left(vE + vP(\epsilon_{int}) \right) \qquad\qquad\qquad = 0 \qquad\qquad (2.18)$$

in which $E = \frac{1}{2}\rho v^2 + \epsilon_{int}$ is the total (kinetic plus internal) energy density.

One more relation to give pressure in terms of internal energy density is needed. For an ideal fluid of low density (number density $n \ll 1/V_{\text{molecule}}$, this is often an adiabatic equation of state

$$P = (\gamma - 1)\epsilon \qquad\qquad (2.19)$$

for ratio of specific heats $1 < \gamma \le 5/3$ in three dimensions. The limit of $\gamma \to 1$ is an isothermal equation of state, in which case an energy equation is no longer needed because pressure is a constant temperature times the density.

If an adiabatic equation of state is explicitly massaged into the energy equation, the result is

$$\partial_t E + \partial_x \left(v \left[\frac{1}{2}\rho v^2 + \frac{\gamma}{\gamma - 1}P \right] \right) = 0 \tag{2.20}$$

It is worth noting that ρv^2 has the same dimensions as pressure P. Naturally so, since the only difference is that ρv^2 represents ordered bulk kinetic energy while P represents disordered thermal energy.

In the context of dissipation of bulk kinetic energy to heat (pressure), especially as concerns strong shocks in which the preshock thermal pressure is negligible, the kinetic energy density is also known as the *ram pressure*.

Extension to multiple space dimensions. The extension of conservation laws to multiple dimensions is as above, however the line segment and endpoints are replaced by a square with a perimeter, or a box with a surface. Or in principle an N-dimensional hypervolume with an (N-1)-dimensional hypersurface, though it certainly appears that the macroscopic universe has only three spatial dimensions.

When the general conservation law (2.1) is integrated about a rectangle or a box, the equations for uniform flow through space in two and three dimensions are seen to be

$$\partial_t \phi + c_x \partial_x \phi + c_y \partial_y \phi = 0 \tag{2.21}$$

$$\partial_t \phi + c_x \partial_x \phi + c_y \partial_y \phi + c_z \partial_z \phi = 0 \tag{2.22}$$

We can see that advection (and by extension the continuity equation) is the divergence of a vector-type quantity, so that we have the multi-dimensional form of (2.16),

$$\partial_t \rho + \nabla_i p_i = 0 \tag{2.23}$$

16

Since we are not dealing with relativistic concerns, upper/lower indices are shamelessly mixed.

The same formulation may be applied to the components of 2.17 one by one, resulting in the divergence of a stress tensor

$$\partial_t(\rho v_i) + \nabla_j(\rho v_j v_i) + \frac{\partial P}{\partial x_i} = 0 \tag{2.24}$$

which leads to the nice compact form,

$$\partial_t v_i + \nabla_j(\rho v_j v_i + \delta_{i,j} P) = 0 \tag{2.25}$$

The Kronecker delta is often omitted, but it is useful to remember that the scalar we call P is just only the dominant hydrostatic part of the general pressure tensor (whose non-scalar parts generally only become relevant when considering the intimate details of shock structure, hence why they get ignored).

The energy equation in multiple dimensions is essentially unchanged save that the v^2 is recognized as $\vec{v} \cdot \vec{v}$,

$$\partial_t E + \nabla_i \left(\frac{1}{2} v_i \left[\rho v \cdot v + \frac{\gamma}{\gamma - 1} P \right] \right) = 0 \tag{2.26}$$

Combined, these five (in three spatial dimensions) equations have the beautiful short form,

$$\partial_t \begin{bmatrix} \rho \\ v_i \\ E \end{bmatrix} + \nabla_j \begin{bmatrix} \rho v_j \\ \rho v_i v_j + \delta_{ij} P \\ \frac{1}{2} v_j (\rho v \cdot v) + \frac{\gamma}{\gamma-1} v_j P \end{bmatrix} = 0 \tag{2.27}$$

This is the conservative form of the the Euler equations.

Nonideal terms of interest. Terms that can't be brought under the divergence sign are said to be nonconservative because they can't be written as the divergence of a flux. This is generically written as

$$\partial_t \vec{\phi} + \nabla \cdot \vec{F}(\vec{\phi}) = \vec{\Gamma}(\vec{\phi}) \tag{2.28}$$

17

where all source terms have been lumped under the Γ banner. In the case of the Euler equations $\vec{\phi} = [\rho, \rho\vec{v}, E]$ and F is the Euler fluxes. By dimensional analysis source terms must have dimension $\left[\vec{\Gamma}\right] = \left[\vec{\phi}\right]/t$. Nearly all astrophysical phenomena of interest originate from nonideal terms, as unlike in a laboratory or engineering setting there are no (physical) boundary terms to drive behaviors.

Source terms typically show up for one of three broad classes of reason. They may represent diffusivities (mass diffusion, viscous stress tensor, thermal diffusion), or even higher order derivatives in the kinetic equation. These represent the tendency of sharp structure to smooth itself, and when present are believed to formally prevent discontinuous structures from forming (a million dollar award awaits the formal proof). The second typical source is additional physics being taken into consideration: Turbulence modelling, radiation energy loss or absorbtion, gravity, magnetization, ionization, multicomponent flow, reactive flows (e.g. combustion), the list goes on: These are simply things going on that aren't part of the transport context of the fluid equations. Finally are geometric and frame terms: phantom "forces" originating from one's choice of coordinates or noninertial frame.

Microscopic diffusivities. The next terms originating from the kinetic equation append themselves to the right side of Eq. (2.27) giving us dissipations,

$$\Gamma = \begin{bmatrix} D\Delta\rho \\ \rho\nu\Delta v \\ \kappa\Delta T \end{bmatrix} \tag{2.29}$$

where D is the molecular diffusivity, ν is the kinematic viscosity and κ is the thermal conductivity. These tell us that mass, momentum and energy all prefer to diffuse away from local maxima and into local minima.

Their presence fundamentally alters the character of the partial differential equation system, from the Euler equations which are strictly hyperbolic (for temperatures greater than 0), to the Navier-Stokes equations which are parabolic.

The Reynolds number is a dimensionless value that compares momentum transport to momentum diffusion,

$$Re = \frac{VL}{\nu} = \frac{\rho VL}{\mu} \tag{2.30}$$

where V and L are some characteristic velocity/length scales and ν is the kinematic viscosity determined by gas microphysics (or alternatively, μ is the dynamic viscosity).

In an engineering context considering either internal (e.g. pipe/turbine) or external (e.g. airframe) flows, the diffusivities can never be entirely ignored because they control the transport of momentum and heat at solid boundaries. This led to one of the early mysteries of high-Re flow, which is that Re for the flow of seawater around a large vessel is so high as to be basically ∞, yet if viscosity is ignored as this suggests should be the case, the vessel should experience zero drag. Obviously this is not the case, and the resolution came in the form of the recognition of the textitboundary layer - that there is always a region near a fluid's interface with a mechanical surface where dissipation cannot be neglected.

Within an astrophysical context however, there are often no mechanical surfaces to introduce a small length scale, so the usually enormous global length scale contributes to a very large Re.

Plugging in ballpark numbers for protoplanetary disk at 300K at 10AU, for example, we get

$$Re \approx \frac{v_{kep}r\rho}{\mu_{H2}} \approx \frac{10^4 \times 10^{11} \times 10^{-7}}{10^{-6}} \approx 10^{14} \tag{2.31}$$

which means that viscosity will take a very, very long time to damp differential rotation. Not surprising: It is this dimensional analysis that tells us diffusion is exceedingly inefficient on large scales.

Noting that all three diffusivities (D, ν and κ) are of equal dimension ($[L^2/T]$); those of mass and heat are related to the viscous one by their own dimensionless numbers. The Schmidt number

$$Sc = \nu/D \tag{2.32}$$

gives the relative importance of mass diffusion to momentum diffusion (viscosity) The Prandtl number

$$Pr = \nu/\kappa \tag{2.33}$$

normalizes the efficacy of thermal diffusion to that of viscosity. In the context of boundary layer flow, these compare the relative thicknesses of the mass, momentum and thermal bounary layers.

Large Prandtl numbers occur in geologic flows, while very small ones (order of .001) are measured for liquid metals due to their quite high thermal conductivities. In the case of small-molecule gasses, both Sc and Pr are predicted to lie in the vicinity of unity by first principles calculations, and reassuringly they are in fact measured to be around 1 for real gasses as well.

Given the enormous global-scale Re above, these terms too may be imagined utterly irrelevant to accretion disks (and assuredly their microscope molecular values are). However, turbulent flows can experience substantially larger *effective* diffusivities if the process which drives the turbulence (e.g. the MRI) is assumed to satisfy certain reasonable isotropy assumptions (see Pringle (1981)). It is precisely the idea of an effective local viscosity that leads to the α-disk in thin

disk steady state accretion theory, and the search for the turbulence driver which can provide an α value appropriate to observed disk lifetimes is one of the central themes in accretion disk research.

__Gravitation.__ Gravitating flows are ubiquious in astrophysical scenarios. In the Newtonian case,

$$\Gamma = \begin{bmatrix} 0 \\ -\rho\nabla\Phi \\ -\rho v \cdot \nabla\Phi \end{bmatrix} \qquad (2.34)$$

$$\nabla^2\Phi = 4\pi G\rho \qquad (2.35)$$

for gravitational potential Φ. For plane waves in a uniform gas with wavevector k, $\Phi \approx k^{-2}\rho$ so that for large scales, gravity is expected to dominate.

The potential must be determined from either direct solution of the Poisson equation or by expansion in Green's functions. While this equation appears superficially innocent it is among the most difficult to solve at scale in parallel computing. The reason is because it is a PDE of elliptic character. Solutions of elliptic PDEs are generally characterized by complete *non*-locality: the solution at every point depends on every other point. In a parallel computer, this requires that every node communicate with every other node to solve the problem, which is among the worst scenarios possible.

For a uniform infinite medium, the pressure perturbation caused by an adiabatic plane wave density fluctuation with wavevector k of $\delta P = c_s^2 \delta\rho$ is independent of k, but the gravitational field fluctuation is $\delta\phi = -\delta\rho/k^2$ which diverges for large wavelengths. Linear analysis gives the dispersion relationship for self gravitating sound waves in an infinite medium as

$$\omega^2 = c^2 k^2 - 4\pi G\rho_0 \qquad (2.36)$$

21

Thus as the wavelength grows, the oscillation frequency drops. By solving for $\omega = 0$, the point at which propagation halts, we arrive at the Jeans length

$$L_J = \frac{2\pi c_s}{\sqrt{4\pi G\rho}} \tag{2.37}$$

which tells us the shortest wavelength which will undergo self-gravitational collapse. Then, the Jeans length is the characteristic scale at or larger than which self gravitation can not possibly be ignored in a uniform medium, as all scales larger than this are unstable against self gravity collapse.

In thin disks, the analogue of the Jeans length is the Toomre Q parameter,

$$Q = \frac{c_s V_k}{\pi G\Sigma} \tag{2.38}$$

first described in Toomre (1964). Here V_k is the Keplerian orbital velocity and Σ is the surface (vertically integrated) mass density. Anywhere $Q < 1$ the disk is locally linearly unstable against gravitational collapse. Examination of the components suggests the obvious condtions for Q to be low: cold (c_s low), large radius (low V_k), and dense (large Σ) parts of the disk, which are not surprisingly the conditions which imply that self gravitation will matter.

While self gravity is the dominant player in the early life of a star system (from the collapse of the molecular cloud core and the duration of active accretion from cloud, which maintains a large disk-to-star mass ratio), by the time a disk reaches the protoplanetary stage self gravity has been a victim of its own success: Self gravitation appears to drive efficient accretion in the early stage of disk life, such that by the time the disk becomes visible the disk to star mass ratio is down to a few percent.

Direct imaging of massive disks in the embedded phase reveals global structure dominated by low angular wavenumber modes (e.g. see Meru et al. (2017) for discussion of the now famous Elias 2-27 disk).

In the inner (Less than some tens of AU) parts of a thin disk, Q is expected to be large and self gravity is not dynamically important, though self gravitationally generated turbulence propagating in from the outer disk may still be a factor (See Armitage (2011) section 3.1).

Magnetism. Magnetism is a major player in all kinds of accretions disks because the conditions for it to arise - an ionized medium that couples to magnetic fields and differential rotation to power a dynamo - are ubiquious.

Neglecting several entire chapters' derivation, it turns out that the idealized form of the magnetized plasma equations are the Euler equations with additional conservative source terms, forming a beautiful set of equations called the ideal MHD equations,

$$\partial_t \begin{bmatrix} \rho \\ \vec{v} \\ E \\ \vec{B} \end{bmatrix} + \nabla \cdot \begin{bmatrix} \rho\vec{v} \\ \rho v\vec{v} - \vec{B}\vec{B} + \delta_{ij}(\frac{1}{2}B \cdot B + P) \\ \vec{v}(\frac{1}{2}\rho v \cdot v + \frac{\gamma}{\gamma-1}P + \frac{1}{2}B \cdot B) + \vec{B}(v \cdot B) \\ \vec{v}B - \vec{B}v \end{bmatrix} \tag{2.39}$$

The evolution of these equations in a manner which does not cause any magnetic divergence to appear is distinctly nontrivial even in Cartesian coordinates. They have many nonideal extensions associated with expansions in electron mass (i.e. finite relative e^--ion drift velocity), finite conductivity and new and interesting isotropy-breaking, tensor-valued parameters.

Because of the great difficulty of solving these equations, and the general expectation that they will lead to small-scale turbulent structure which there is no hope of numerically resolving anyway, MHD will not be considered directly.

In disks, magnetism (and magnetic turbulence) will be intimately coupled with the local ionization level and whether it is high enough to sustain electric currents and couple the gas motion to magnetic pressure. Outside the innermost edge of the disk that can thermally ionize alkali metal atoms directly, in turn, ionization is intimately coupled with external drivers of ionization and recombination. Ionization is expected to be driven by the impingement upon the disk of external ionizing photons, cosmic rays, and self ionization due to radioactive atoms, while recombination will be substantially aided by dust particles mopping up free electrons.

Radiation physics. Radiation is a key effect in astrophysical objects, if for no other reason that (outside of LIGO) it is only through radiation that anything in the outer universe becomes visible and knowable to us. The full radiation transfer function of a classical fluid lives in a six dimensional space (the radiation emission rate as a function of frequency and angular orientation, at every point in physical space) which means that simulating the full equation directly is firmly on the "hopelessly intractable" list.

Some reasonable assumptions can render radiation transfer tractable, or at least less intractable, in many important cases. In a gas medium without a clear breaker of isotropy, it is often reasonable to assume that the emission is isotropic (reducing the general problem to 4 dimensions).

The real radiation rate of a gas is a sum over an infinite number of atomic/molecular transition lines, continuum blackbody emission, bremsstrahlung

in hot plasmas, and cyclotron emission from magnetized plasmas, and in highly dynamic systems (where thermal equilibrium does not necessarily hold) becomes a history-dependent function as well, which steps back towards "intractable."

The wavelength of a photon determines how much it will interact with its environment.

At the lowest energy scale useful outside of a laboratory, electron-proton spin coupling results in hyperfine splitting. These couplings typically have energies in the high RF to microwave region. The neutral hydrogen 21cm line is the best known of these and is used to track the presence of neutral molecular hydrogen. Electron-electron spin coupling has higher energies. It is responsible for e.g. the ortho/para hydrogen split, which is responsible for the anomalous specific heat of molecular hydrogen below about 70K.

At higher energies, rotation states of molecules with a dipole moment have large transition rates because they can directly change J by emitting or absorbing photons. Rotation states of smaller molecules observed in astrophysical scenarios may most often be associated with millimeter radiation ($\approx$1THz) into the far infrared ($10\mu \approx 40$THz). Their long wavelength relative to the haze of submicron dust that obscures many objects from optical view makes them valuable for probing stellar birth and the galactic center. Both the SMA and ALMA have taken direct images of disks using the carbon monoxide $J = 1 \to J = 0$ transition at 850um.

Excited vibrational states of molecules can have energies of an appreciable fraction of an electron-volt, which is beyond the reach of thermal excitation except in or very near stars (1eV / $K_b \approx 11000$K) or compact object accretion disks. In

general by the time the temperature is high enough to enter these states the tail of the energy distribution is beginning to cause molecular dissociation and ionization.

Dust particles may be expected to radiate as black (or grey-)bodies, glowing with characteristic infrared peaks that trace the temperature of the dust emitting them as a function of radius if it can be spatially resolved, or generating a convolution over the emitting area if it cannot. As far as any possibility of inducing the oscillatory instabilities that are the subject of this thesis goes, dust blackbody emission may be ruled out completely because its temperature dependence, as T^4, is a far too rapidly decreasing function of falling temperature.

Molecular binding energies are typically on the order of 1-10eV, corresponding to temperatures of around 10^4 to 10^5K. Temperatures in this range are associated with an extremely sharply increasing radiation rate as a functon of temperature due to the prevalence of partially ionized states and excited molecular states with very high transition rates.

Per Gehrels and Williams (1993), temperatures from about 2×10^5 to around 10^7K have an overall *decreasing* radiation rate as the atomic cores become completely stripped of their electrons. Finally, at temperatures above around 10MK all atoms trend towards completely ionized and the radiation emission function quickly becomes dominated by bremsstrahlung, which increases as $\sqrt{T}$.

The detailed shape of the predicted plasma radiation curve has evolved with research and increasing computing resources. Compare e.g. Tucker and Gould (1966) and Gehrels and Williams (1993) and Schure, Kosenko, Kaastra, Keppens, and Vink (2009). However the essence depicted in 5 is consistent, and substantially more precise models generally become dependent on the atomic composition of the plasma.
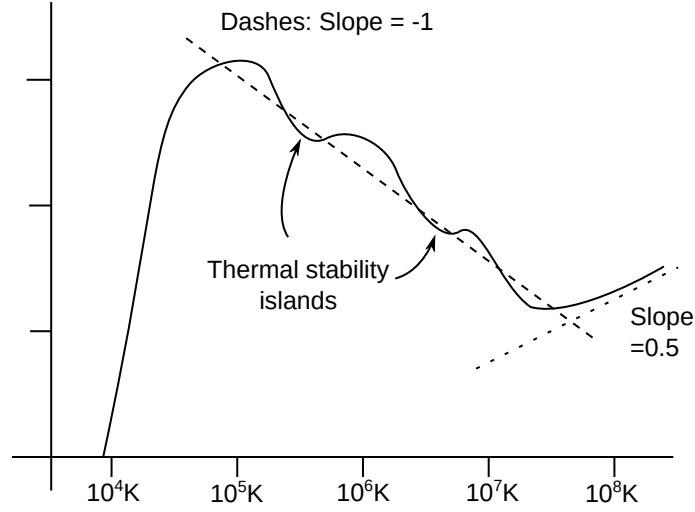
Figure 5. A qualitative depiction of a modern plasma radiation emission rate curve spanning 10^4K to $10^8 K$. The rate is an extremely rapidly increasing function of temperature below 10^5K. It peaks around $1 - 2 \times 10^5$K, then acquires an overall decreasing trend with roughly $\Lambda \propto 1/T$, although two islands of thermal stability exist. It becomes minimal around $1 - 2 \times 10^7$K, before rising with bremsstrahlung as $\Lambda \propto \sqrt{T}$.

The ability of radiation to escape (or not escape, as the case often is) is described by the optical depth

$$\tau(\lambda) = \int_0^L n\sigma(\lambda)dl \tag{2.40}$$

which is the number of times a photon of wavelength λ would expect to get scattered if it tried to follow a path of length L through a uniform medium.

In the limit that $\tau << 1$, radiation (at that frequency) flies freely out of the optically thin volume and this manifests itself as an energy loss rate per time per volume of Λ,

$$\Gamma = \begin{bmatrix} 0 \\ 0 \\ -\Lambda(\rho, T; ...) \end{bmatrix} \tag{2.41}$$

27

Alternatively if an optically thin volume is irradiated with microwaves/heat/light from a source like a star, the result may be a volume heating function. All else being neglected, optically thin volumes may be expected to hunt the equilibrium whereat their frequency-integrated radiation emission and absorbtion powers are equal.

Because opacity is very strongly dependent on wavelength, it is often the case that energy at one wavelength can enter a region, be absorbed and re-radiated, and the new wavelength find itself trapped. Such it the case of the greenhouse effect, where Earth's atmosphere is essentially transparent to near IR and visible light, but highly opaque to significant parts of the thermal IR spectrum that its surface glows in.

Depending on the slope of the radiation function $\partial_T \Lambda$, it is possible for a radiating gas where radiation absorbtion and emission are competing to be thermally unstable if the derivative is negative. This can be seen from a simple perturbative stability argument: If an increase in temperature perturbs the radiation loss rate down, the temperature will rise further, leading to even less radiation: linear instability and runaway.

In the opposite limit where $\tau >> 1$ lies radiative diffusion: The photons cannot get anywhere in a straight line and instead conduct a random walk. Radiative diffusion adds an additional term to normal heat diffusion,

$$
\Gamma = \begin{bmatrix} 0 \\ 0 \\ k\Delta\Lambda(\rho, T; ...) \end{bmatrix}
\tag{2.42}
$$

Sophisticated radiation transfer and radiation rate functions are not considered in this work, however temperature parameterized cooling ($\Lambda \propto T^{\theta}$) is implemented efficiently.

Dust dynamics. A natural extension to equations (2.27) for a single fluid is to consider two or more superimposed fluids which can exchange momentum, energy and perhaps particle numbers (e.g. ionization/recombination or reactive flows).

In the case of a multi-phase fluid consisting of mixed atomic/molecular species, the coupling time will be spectacularly short - on the order of the mean free flight time - such that decoupling will be virtually nonexistent except under the most extreme conditions. An exception to this is a neutral-ion fluid, in which the persistent application of electromagnetic forces only on the ions can eventually accumulate a substantial displacement though the integration over time of the relative velocity, even though the δv itself is limited to roughly the free particle acceleration times the scattering time.

Many interesting effects in electron-ion plasmas are caused by effects which depend on the electron- to-proton mass ratio or its square root, introducing separations of scale by factors of around 45 or 2000. In the case of gas-dust coupling, the ratios are vastly larger still. Even the smallest dust particles, the sub-micrometer sized 'monomer' spherules, are likely to have millions of times the mass of a hydrogen molecule.

Pressureless, isothermal fluid. To a good approximation, we may think of the dust embedded within a disk as a pressureless and isothermal ($\gamma \rightarrow 1^{+}$), so that compression causes neither heating nor any introduction of pressure) second fluid, coupled to the gas by drag.

Suppose the dust is an ideal gas. In this case, in thermal equilibrium, we have the ideal gas law

$$P = nk_bT \tag{2.43}$$

with pressure P, number density $n = N/V$, Boltzmann constant $k_b = 1.381 \times 10^{-23}$ in S.I. units, and T the temperature. Using the particle mean mass μ_d we can replace the number density with the mass density

$$P = \frac{\rho}{\mu_d}k_bT \tag{2.44}$$

The mass of a solid particle scales as the cube of its size. The dust agglomeration process is capable of creating extremely 'fluffy' structures of low fractal dimension (In Mannel et al. (2016) a dust agglomerate was examined which had a fractal dimension of only 1.7), whose mass grows much more slowly than the cube, but even so the "molecular" mass quickly becomes so large that pressure is suppressed to effectively zero. This is the familiar result in granular physics on earth that grain "fluids" have no thermal pressure.

As a reference point, using $c_s^2 = \sqrt{P/\rho} = \sqrt{k_bT/\mu}$, the isothermal soundspeed in a "gas" made of 10nm iron spheres is about 2.8m/s, and that of 10μm iron spheres is about 46μm/s per second at room temperature. By way of comparison, the adiabatic sound speed in molecular hydrogen under these conditions is around $1,300$m/s, and the Keplerian orbital velocity 10 A.U. from the Sun is about 9,400m/s.

To substantiate the belief that the grains have an adiabatic index indistinguishable from 1, consider the shortest wavelength phonon accessible to a thermal bath at temperature T,

$$E = \hbar\omega = \hbar(c_s2\pi/L) = k_bT \tag{2.45}$$

if we assume this phonon is in the linear-acoustic region of the solid dispersion relation. If we suppose for normal-density solids that the sound speed is about 2000m/s, this suggests a shortest phonon wavelength of $L_0 = 300$pm at room temperature. Then there would be something like $(D_{particle}/L_0)^3$ phononic degrees of freedom that the heat bath can access compared to precisely three translational and two solid-body rotational. So, then, a 100nm monomer dust particle would have about 37 million accessible internal DoF and an adiabatic index of about 1.00000005, which is close enough to 1!

If (2.45) is solved for length and is equated to length derived from mass and solid density, we can estimate the mass of a particle not dominated by thermal DoF (i.e. which is not totally isothermal).

$$\frac{4}{3}\pi \left[\frac{\hbar c_s 2\pi}{k_b T} \right]^3 \rho_{solid} = M \tag{2.46}$$

The result is only valid for masses containing many atoms which can support a near-continuum of phonon states. However, even at 10 K, solid particles much larger than a nanometer will have accessible phonon DoF.

While the actual phonon density of states in solids and the structure of protoplanetary dust grains both are whole complex fields by themselves, this back of the envelope analysis is sufficient to see that for any reasonable conditions the grains will not heat up upon compression.

Back of envelope bounds. Some back-of-the-envelope calculations may be applicable to determine/bound the cases of interest. First, the Reynolds number: Assuming a 75/25 H_2/He mix with a surface density of 2000g/cm^2, with a scale height at 1AU of .1AU, yields an approximate number density of 3×10^{14}/cc and a mass density thus of 10^{-9}g/cc. The dynamic viscosity of the gas is about

8×10^{-5}g/cm-sec. Suppose on the larger end that a 100cm diameter particle experiences a headwind of 100 meters/sec.

In this case we would have a Reynolds number of $Re = \rho v l / \mu \approx 12$. Given that the potential headwind for a large particle is set by the deviation of the disk's rotation from Keplerian, which is fairly small for real post-class-0 young stellar objects, the primary avenue for increases in Re is the formation of larger aggregates. Certainly 10- or 100-meter class objects could reach the point of turbulent flow ($Re \approx 100 - 1000$), but smaller particles will not.

In similar conditions, the mean free path is about 9cm, so our 1-meter object would have a Knudsen number $Kn \approx 0.1$ such that non-rarefied flow must definitely be accounted for in the inner areas of the disk.

These represent likely upper bounds on Re and lower ones on Kn.

The viscosity used above is accurate at room temperature. For a hydrogen-helium mix the dynamic viscosity varies as roughly the 2/3 power of T, such that temperature ranges of a factor of ten (e.g. between 1000K in the innermost disk and 100K in the outer) the viscosity may range over a factor of roughly 5.

Taking a fiducial upper limit on relative speed of around 100m/s, over a likely range of gas temperatures (very roughly 1000K on the inner edge, perhaps 50K on the periphery) the speed of sound in the H_2/He mix will vary from about 500m/s to 2300m/s, such that the Mach is unlikely to exceed about 0.2; Certainly supersonic relative motion is unlikely!

Drag Force Equations. The motion of dust particles relative to the gas they are embedded in results in a drag term which opposes the relative motion and so tends to couple the motion of the gas and dust. If the coupling is presumed to be linear (opposition force $\propto |\delta v|$) then the relative velocity, absent drivers,

decays over a characteristic timescale

$$\tau_{cpl} = \delta v / (F/\mu) = 1/K_d \qquad (2.47)$$

In the case that τ_{cpl} is much shorter than the other timescales, coupling is strong and the behavior is perturbatively different from that of a single fluid. In the case it is very long, the two fluids flow through each other nearly independently and it is their coupling which is perturbative. When τ is neither, things are interesting.

An understanding of drag across a wide range of τ_{cpl} is needed because it is expected to evolve across many, many orders of magnitude relative to an orbital period, from a tiny value for microscopic grains to essentially infinity for kilometer sized boulders.

There are three principle dimensionless parameters relevant to determining how the drag behaves. These are the Reynolds number

$$Re = \frac{\rho v L}{\nu} \qquad (2.48)$$

where ρ is the fluid density, v the relative velocity, L a relevant length (e.g. the diameter of an obstructing body in a flow) and ν is the microscopic viscosity, the relative Mach

$$M = |v_g - v_d|/c_s, \qquad (2.49)$$

and the Knudsen number

$$Kn = \lambda_{mfp}/d, \qquad (2.50)$$

with

$$\lambda_{mfp} = (\sqrt{2} n \sigma(T))^{-1} \qquad (2.51)$$

defining the mean free path of a single species in terms of its number density n and kinetic cross section $\sigma(T) = \pi D_{11}(T)^2$ where the effective molecular size

depends on temperature, which is the dimensionless ratio of gas mean free path to particle diameter. When Re is small, the flow is linear, laminar and viscous while when Re is large it is turbulent. When Kn is small, the particle is much larger than a free path and experiences the gas as a continuum. When Kn is large, the particle is small and experiences rarefied particle dynamics.

At very large mass densities, as the specific volume decreases, the equation of state, viscosity, and all other parameters computed here begin to deviate markedly from the predictions of the low-density formulae as rates of ternary, quaternary, etc interaction are no longer vanishing. The issue of interparticle spacing is not at issue for gasses, however it is not impossible that at substantial dust loads the dust volume fraction

$$\theta_d = \rho_d/\rho_s, \tag{2.52}$$

where ρ_d is the mass of dust per volume and ρ_s is the intrinsic density of the solids, may increase to appreciability. If a dust overdensity created by the streaming instability undergoes rapid self gravity collapse into a bound compact object (a proto-asteroid of the rubble pile type), θ_d will become large and this is not accounted for.

In the process of searching the literature it has become apparent that some parameters or their inputs are routinely expressed in one of multiple ambiguous ways with the determination left to context. Most particularly, the meaning of 'size' must more often than not be deduced as meaning one of radius or diameter based on the numeric prefactors on formulae. **We take the *diameter* of the (presumed) spherical dust particles as** l. The Epstein drag term requires a thermal mean speed, and the value $\bar{c} = \sqrt{\frac{3k_bT}{\mu_g}}$ is used (which differs from the averge particle speed by 8%).

The drag is described by another dimensionless value, the drag coefficient, which relates the actual drag force to the ram force (ram pressure times cross section),

$$C_d = \frac{F_{actual}}{\frac{1}{2}\rho_g \delta v^2 \times A} \tag{2.53}$$

At low speeds, drag force is linear in δv rather than quadratic so $C_d(v \to 0) \propto 1/v$. Under other conditions, the drag coefficient is lower and typically acheives values between $1/2$ and 2 for a very wide range of Re, M and Kn values.

Formulating a single function that accurately describes $C_d(Re, M, Kn)$ without restriction upon any of the parameters is impractical. Not that it is impossible - given enough degrees of freedom in an appropriate fitting function ANY curve can be fitted - but the resulting morass of empirical coefficients and forms would be expensive to evaluate.

Reliable analytic forms are available in two limits: At low Re, the force on the sphere is given by Stokes drag,

$$F_{stokes} = 3\pi n u d v \tag{2.54}$$

as first derived by Stokes (1851) for an incompressible liquid, which gives the coefficient of drag as

$$C_{d,st}|_{Re<<1,Kn=0,M<<1} = 24/Re \tag{2.55}$$

The force on a sphere in free molecular flow was derived by Epstein and a much simpler expression that matches Epstein's very large exact expression to within 1% at all speeds was derived in G. Stokes (1850),

$$C_{d,ep}|_{Kn>>1} = v\rho_g \sigma \sqrt{v^2 + \frac{16}{3}(\gamma - 1)e_{int}} \tag{2.56}$$

35

Where $v = |v_g - v_d|$ and $e_{int} = \frac{P}{(\gamma - 1)\rho_g} = (E_{tot} - KE)/\rho_g$ is the specific internal energy density. This is the RMS sum of the leading terms of the high- and low-speed limit of the full function for Epstein drag on a polished hard sphere.

The first successful calculation that merged these regimes together for low-speed flow was that of Cunningham in 1910 (Cunningham (1910)) who recognized that for small particles the no-slip condition at the particle's surface needed to be modified to a partial-slip condition, with the partiality of the slip increasing as the particle shrank. Today the drag equation for small particles bears his name in the form of the Cunningham correction,

$$C_{d,cu}|_{Re<<1,M<<1} = \frac{24}{Re}(1 + kn \times A)^{-1} \tag{2.57}$$

In fact, (2.57) has been superceded by modern empirical measurements which yield excellent agreement with data using a correction of the form

$$C_{d,cu}|_{Re<<1,M<<1} = \frac{24}{Re}(1 + kn(\alpha + \beta e^{-\gamma/Kn})^{-1}. \tag{2.58}$$

The difference, it is seen, occurs for $Kn \approx 1/\gamma$. In Allen and Raabe (1985), the Cunningham correction was measured using plastic spheres in a partial vacuum of air. Their measurements have $\alpha = 1.142$, $\beta = .558$ and $\gamma = .999$, which values are adopted here.

In continuum flow, when Re is not small, the drag coefficient deviates from $1/Re$. Expansions in powers of Re (e.g. Oseen equation) have not proven practically useful at large Re in that they fail to much extend the valid range of the equation, however empirical fits provide excellent results. For $Re <\approx 905$,

$$C_{d,st}|_{Re<905,Kn=0,M<<1} = 24Re^{-1} + 4Re^{-1/3} \tag{2.59}$$

Back of the envelope calculations for dust in a disk suggest that $Re > 10$ is unlikely to be acheived. However, for completeness' sake, general utility, and to

36

avoid flagrantly wrong results in the event of unexpected circumstances, it is a good idea to maintain some degree of correctness in the drag coefficient for large Re.

Smooth spheres in a quiescent background flow enter the *Newton* regime from $\approx 1000 < Re <\approx 250000$ where the drag coefficient is 'about .44.' Either roughness on the sphere's part or turbulence in the background flow decrease the upper critical Re. The upper limit marks the change from a laminar to a turbulent boundary layer around the sphere and is associated with a huge decrease in drag coefficient, to roughly 0.1, after which C_d slowly increases again. This is the supercritical Re regime and will not be modelled; The adopted curve asymptotes to $C_d(Re \to \infty) = .407$.

Rather than making a piecewise function, which introduces numeric convergence problems (or increased complexity) when solving the drag ODEs and problematic branching statements into tight-grained parallel code, a single drag function correlation is used,

$$C_{d,st}|_{Re<2\times10^5,Kn=0,M<<1} = 24Re^{-1} + 3.6Re^{-0.319} + \frac{.407Re}{8710 + Re}. \tag{2.60}$$

Variations of the first two terms are often quoted with the coefficients of Schiller & Naumann as $4Re^{-1/3}$, or similar. Using drag data corrected for wall effects, Brown and Lawler (2003) provided the above coefficients as their equation 19 based on previous proposed C_d equations of the same form.

The Cunningham correction is applied to this generalized continuum drag equation without proof of correctness other than that it reproduces the correct results in appropriate limits to yield the following equation implemented in the

code:

$$C_d|_{Re<2\times10^5,M<\approx0.2} = \frac{24Re^{-1} + 3.6Re^{-0.319} + \frac{.407Re}{8710+Re}}{1 + Kn(1.142 + .558e^{-.999/Kn})} \tag{2.61}$$

This equation reproduces extremely accurate drag curves for the parameters which may be expected in dusty disk conditions, and is widely applicable to a very broad range of flows in other conditions as well.

No serious attempts to accurately model the effect of M in the drag coefficient equation were made, simply because supersonic relative velocities between gas and dust will not occur, and even if they were unphysically specified as an initial condition, would rapidly decay and so accounting for them adds a considerable amount of computational effort to no end.

Comparisons with published drag equations that use both M and Re find that the corrections in continuum flow due to compressibility to be less than a few percent below $M = 0.2$. This is not surprising since compressibility corrections are as the square of Mach to leading order. The exact behavior of Epstein drag in the supersonic limit is obvious, $C_d \to 2$; The deviation in (2.61) caused by high speed is only about 20% at Mach 1.

Other forces on particles. In a more general case than under consideration here, the rotation of the particles may be taken into account, which adds an equation for the evolution of their angular momentum and introduces e.g. the Saffman effect (rotating particles attracted towards shear gradient) and the Magnus effect (rotating particles pushed towards $\omega \times \delta v$). If the particles are large enough that the flow field is not uniform over their area, effects which scale as higher powers of particle diameter become relevant (Faxen terms) and can either dominate or alter propagation speeds. If particles are sufficiently large or intense acoustic waves are present, the Froude-Krylov effect matters (force on particle

from integral of pressure over area). Naturally, if the particle density becomes sufficiently large that the particles occupy a nontrivial fraction of the geometric volume, this greatly modifies the dynamics. If the particles are embedded in a fluid with a large mass density (e.g. air bubbles in water), the virtual mass effect (fluid entrained in the boundary layer effectively forced to move with the particle) can be very large. Particles dragging a turbulent wake which are subject to acceleration experience an effective hysteretic/memory force due to the finite time required for the boundary layer to reaccomodate (Basset effect).

On astrophysical timescales, the Poynting-Robertson effect (Robertson and Russell (1937)) eventually removes smaller particles from debris disks, given long enough for the radiation pressure from special-relativistically-abberated sunlight to sap the particle's orbital angular momentum. Per Roberton's equation 4.5, the time t

$$t = (7\text{MY})(a/\text{cm})(\rho/\text{g/cc})(R/\text{au})^2 \tag{2.62}$$

is how long a spherical blackbody in thermal equilibrium of radius a and density ρ takes to spiral in to an orbital radius touching the sun's photosphere, provided it is not *so* small that the radial radiation pressure term defeats the gravity entirely (which can happen to ionized molecules whose radiation scattering cross section is enhanced). However, if we want a $t_{pr} < t_{disk} \approx 1MY$ then plugging in 10AU and a density of 1 implies a particle size of less than about 60ish micrometers. Particles can definitely grow beyond this size via known agglomeration mechanisms.

All of the effects fluid dynamicists associate with particles embedded in fluid have, at least in principle, an analogue operating upon dust particles embedded in a gas disk even if the parameters of the flow regime are sometimes wildly different.

The forces potentially influencing a small particle (low Re), and some relevant scalings, as described by the Basset-Boussinesq-Oseen (BBO) equation are Stokes drag (dv), Froude-Krylov force (action of pressure gradient on particle surface area, d^3k), virtual mass effect ($d^2a\rho_{gas}$), and Basset effect (effective force associated with delayed development of stable boundary flow, $\approx d^2v$). Except for viscous drag, all decrease in importance rapidly for small particles.

The BBO equation does not cover the Saffman effect Saffman (1965), in which a small particle in a viscous fluid is attracted to a shear gradient with a strength proportional to

$$F_{saffman} \propto \rho_g \sqrt{\nu}\sigma_d(v_g - v_d)\sqrt{|\dot\gamma|} \tag{2.63}$$

where $\dot\gamma$ is the strain rate. However, it is difficult to forsee sufficiently intense sustained shearing for it to generate sustained lift.

For the most part, these effects (while in and of themselves certainly interesting) can generally be written off in astrophysical circumstances because the particles are too small and the scales of flow gradients and curvature are too large.

Viscosity model. In the above equations for the drag force in the continuum regime (i.e. (2.61)), reference is made to the molecular viscosity μ.

As described in Chapman et al. (1962) (or any other edition of *The Mathematical Theory Of Nonuniform Gasses*), the point center of force (PCOF) model provides a quite accurate description of the viscosity of hydrogen, helium, and hydrogen-helium mixtures across a very wide range of temperatures, including all those of interest (C&C chapter 12 table 14), and so this model of viscosity is adopted for use in gpu-Imogen's gas-dust drag calculation.

Simply quoting the input equations and the final answers, the PCOF model assumes that spherical molecules repel each other with a force along the line connecting their centers which is of magnitude

$$F = \kappa r^\nu = F_0 (r/r_0)^\nu \tag{2.64}$$

In the limit that $\nu \to \infty$ the hard sphere result is recovered with spheres of radius r_0. This model is effective for relatively spherical molecules and especially for relatively small ones, which lack low-energy molecular vibrational modes.

The viscosity and kinetic cross section of a single species PCOF gas behave as

$$\mu = \mu(T_0)(T/T_0)^{1/2+2/(\nu-1)} \tag{2.65}$$

$$\pi D_{11}^2 = \sigma(T_0)(T/T_0)^{1/(\nu-1)} \tag{2.66}$$

where D_{11} is the effective diameter of species 1 and πD_{11}^2 is the kinetic cross section. Again when ν is large, $\mu \propto \sqrt{T}$ and the kinetic cross section becomes constant as expected for hard spheres.

The viscosity model introduces somewhat of a problem of overdefinition in application to partly rarefied flow: Kn is defined through the mean free path, which scales as the inverse of the gas kinetic cross section. Thus we are not free to look up both experimental measurements for the Cunningham correction and gas kinetic cross sections, because the requirement that (2.57) equal (2.56) when Kn is large has already fixed their ratio.

This is resolved here by accepting the Knudsen number definition via mean free path, (2.51) and using the Epstein equation (2.56) to compute the kinetic cross section,

$$\pi D_{12}^2 = \sigma_0 = \sqrt{\frac{2}{27}} A \sqrt{k_b m_g T} / \mu \tag{2.67}$$

in which A is the coefficient on Kn in the Cunningham correction at large Kn (the values adopted from Allen and Raabe (1985) have A equal to precisely 1.7), m_g is the molecular mass, T the temperature and μ the dynamic viscosity at that temperature.

Thus as inputs, we accept a viscosity, the reference temperature at which that viscosity is measured, and the temperature dependence exponent. For example, the NIST REFPROP database gives the viscosity of H_2 at $25\,\text{degC}$ as 8.9153×10^{-6} kg/m-sec for a molecular diameter of 123.8pm, and that of air 18.492×10^{-6} kg/m-sec for an effective molecular diameter of 167.4pm. These values are slightly smaller than printed values (136pm and 174pm respectively), but those values refer to hard spheres.

Viscosity models (and other relevant thermodynamic parameters like adiabatic index) for several relevant gasses are coded in GPU-Imogen in the file `fluidDetailModel.m`.

Fluid-Dust Coupling Equations. Once the form of the drag force for a single particle embedded in fluid is available the next step is to apply this to the equations that couple two fluids. The presence of multiple fluid fields can potentially cause notational difficulties. Here, x_g denotes a gas quantity while x_d denotes a dust quantity. Functions which are unambiguous may not be subscripted.

The first move to apply the drag force to the coupled fluid equations is to go from the force on one particle to the volume force density and convert to vector

form,

$$F_{one} = C_d(Re, Kn)\frac{1}{2}\rho_g\sigma_d|\delta v|^2 \tag{2.68}$$

$$F_{vol} = C_d(Re, Kn)\frac{1}{2}\rho_g\sigma_d|\delta v|^2 frac\rho_d m_d \tag{2.69}$$

$$\vec{F}_{vol} = C_d(Re, Kn)\frac{1}{2}\rho_g\sigma_d|\delta v|\frac{\rho_d}{m_d}\vec{\delta v} \tag{2.70}$$

$$\tag{2.71}$$

Where $\delta\vec{v} = \vec{v}_g - \vec{v}_d$, σ_d is the dust particle cross section. The volume force density is just the force on one particle times the dust number density.

This completes suffcient preparation to present the equations for coupled gas-dust drag. These are a collection of ten first-order hyperbolic PDEs with source terms, given here in conservative form. They are two copies of the Euler equations, coupled by exchange of momentum and energy:

$$\partial_t \begin{bmatrix} \rho_g \\ \vec{p}_g \\ E_g \\ \rho_d \\ \vec{p}_d \\ E_d \end{bmatrix} + \vec{\nabla} \cdot \begin{bmatrix} \rho_g\vec{v}_g \\ \rho_g\vec{v}_g\vec{v}_g + P(\rho_g) \\ \vec{v}_g(E_g + P(\rho_g)) \\ \rho_d\vec{v}_d \\ \rho_d\vec{v}_d\vec{v}_d \\ \vec{v}_d E_d \end{bmatrix} = \begin{bmatrix} 0 \\ -\vec{F}_{vol}(dv) \\ -\vec{v}_d \cdot \vec{a}_d \\ 0 \\ \vec{F}_{vol}(dv) \\ \vec{v}_d \cdot \vec{a}_d \end{bmatrix} \tag{2.72}$$

Because of operator splitting, we now concern ourselves with outlining an efficient method to handle just the drag term. For finite amounts of dust, the gas experiences a matching reaction and so the relative acceleration is given by

$$\vec{a}_{rel} = \partial_t\vec{\delta v} = (-\vec{F}_d/\rho_g - \vec{F}_d/\rho_g) \tag{2.73}$$

The familiar reduced mass appears, this time as the reduced density:

$$\vec{a}_{rel} = -\vec{F}_{dr}\frac{\rho_g + \rho_d}{\rho_g\rho_d} = -\vec{F}_{dr}/m_r \tag{2.74}$$

Similar application of kinematics to forces and velocities, followed by remembering to append the word 'density' to everything, gives explicitly the equations for the gas and dust velocity:

$$\vec{v}_{st} = \frac{(\rho_g \vec{v}_g + \rho_d \vec{v}_d)}{\rho_g + \rho_d} \tag{2.75}$$

$$\vec{v}_g(t) = \vec{v}_{st} + \vec{dv}(t)\rho_d/(\rho_g + \rho_d) \tag{2.76}$$

$$\vec{v}_d(t) = \vec{v}_{st} - \vec{dv}(t)\rho_g/(\rho_g + \rho_d) \tag{2.77}$$

where $\vec{v}_{st}$ is the sticking speed. To get the gas and dust momentum, we simply multiply by the appropriate mass density. Under the assumption that the Basset term is irrelevant (i.e. that the drag force is instantaneously opposed to the relative velocity at all times), we can solve a single *scalar* equation for the decay of δv.

The last aspect of concern is the desire to keep track of heating while solving the drag equations since heating will, of course, alter the gas' thermodynamic properties.

Because of the overwhelming mass of a dust particle relative to a gas particle, the gas is assumed to walk away with 100% of the dissipated heat caused by drag. Within the total energy formulation used for the gas, heating is handled by simply adding to the gas' energy any kinetic energy lost by the dust due to drag:

$$\frac{d}{dt}E_{total} = 0 = KE'_{gas} + KE'_{dust} + U'_{int,gas} \tag{2.78}$$

This permits exact conservation of energy and yields an exact expression for the heating of the gas as a function of velocity decay, independent of the details of the drag force

$$U_{int}/\rho_g = U(v_{rel} = v_0) + \frac{\rho_d(v_0^2 - v_1^2)}{\rho_g + \rho_d} \tag{2.79}$$

44

This equation comes from a work integral and is only valid when the relative velocity is undriven (e.g. no pressure gradient). An analagous but more complex equation is available if a constant gas acceleration a_0 introduces a steady-state drift velocity,

$$U_{int}/\rho_g = U_0/\rho_g + ka_0^2 t - 2\vec{a}_0 \cdot (\vec{v} - \vec{a}_0) \text{expm1}(-k*t) - (\vec{v} - \vec{a}_0)^2 \text{expm1}(-2*k*t) \quad (2.80)$$

where $\text{expm1}(x) = \exp(x) - 1$. If the acceleration $\vec{a}_0 = -\nabla P/\rho$ vanishes, the final term yields the difference in velocities squared in (2.79).

These expressions provide useful approximations, however it is simpler and much more reliable to apply (2.78) to determine the final total energy density of cells after the new velocities are known: This guarantees that energy is identically conserved.

Qualitative insight into the behavior of dusty gas is obtainable by considering plane waves in a medium which is uniform and otherwise at rest with itself.

Wave motion in dusty gasses has three regimes, one of which can efficiently convert kinetic energy into heat. In a uniform background initially stationary and at rest with itself, the plane wave eigensystem has the matrix

$$M_{gd} = \begin{bmatrix} -i\omega & i\rho_g k & 0 & 0 & 0 \\ 0 & \hat{K}_d/\rho_g - i\omega & ik/\rho_g & 0 & -\hat{K}_d/\rho \\ 0 & ikc_0^2\rho_g & -i\omega & 0 & 0 \\ 0 & 0 & 0 & -i\omega & ik\rho_d \\ 0 & -\hat{K}_d/\rho_d & 0 & 0 & \hat{K}_d/\rho_d - i\omega \end{bmatrix} \quad (2.81)$$

where k is the magnitude of the wavevector and $\hat{K}_d = K_d \frac{\rho_g \rho_d}{\rho_g + \rho_d}$ where K_d is the stopping time of a single dust particle and c_0 is the gas-only soundspeed.

This system has five eigenvalues. Two of them are zero and correspond to arbitrary dust and gas density fluctuations (entropy waves). One does not propagate, and corresponds to opposing gas/dust motion that damps, independent of wavenumber. The final two are the ones of interest and correspond to the modified sound waves going in the $+k$ and $-k$ directions.

When the systems are weakly coupled (K_d much smaller than oscillation period), the dust trends toward the inviscid Burgers equation. Linear solutions become weakly stable at short times in the folowing sense: a superimposed dust velocity disturbance causes a dust density disturbance that grows linearly in time, such that adjacent solutions with different δv_d drift apart from each other in density norm proportional to time.

The behavior of the two sonic modes is outlined in figure 6. When coupling is weak, the structure of the unperturbed sound wave is modified by damping (it acquires an imaginary part). The dust is always trying to follow the gas sonic motion but never really succeeds. When coupling is intermediate, dissipation is large (top middle of figure): because the gas and dust velocities are significantly out of phase. When the coupling becomes strong, there is effectively only one eigensystem because v_{dust} is locked to v_{gas}. Dissipation again becomes small, but wave phase speed decreases (top right of figure): the pressure restoring force is the same, but the density being dragged along is now $(\rho_g + \rho_d)$ in $c_s \propto \sqrt{P/\rho}$. The perfect coupling limit recovers single-fluid behavior with a modified equation of state.

GPU-Imogen's ability to handle dusty wave propagation is prodded by the DustyWave test problem. As discussed in Laibe and Price (2011a) and seen in the
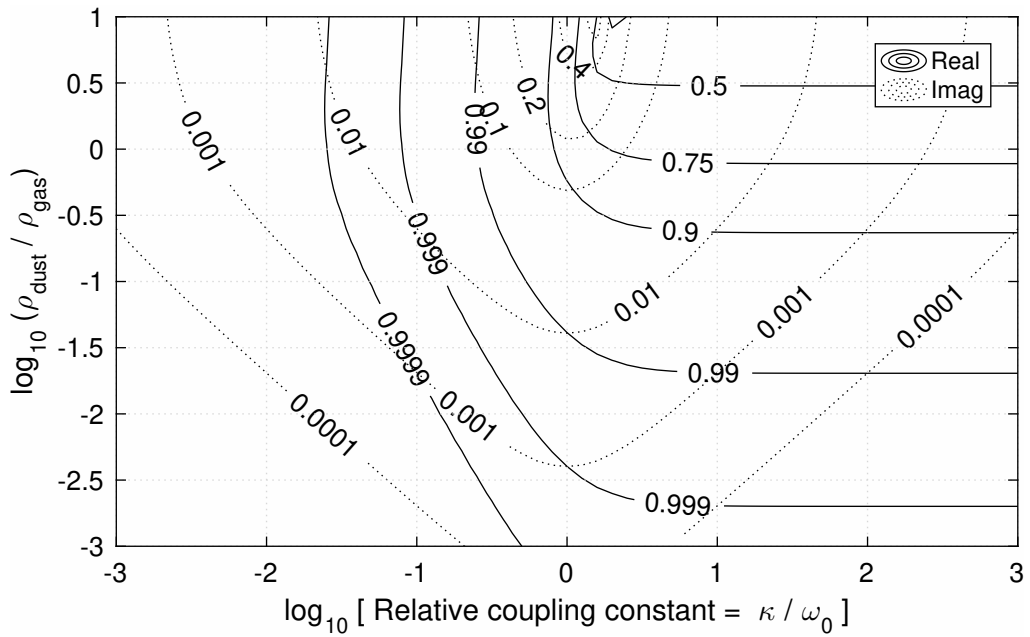
Figure 6. Relative real and imaginary parts of the sonic eigenvalue as functions of the coupling strength (horizontal) and dust load (vertical). Dissipation (imaginary part) is significant only when the relative coupling is in the vicinity of unity. Substantial modification of wave propagation speed occurs only when coupling is strong and dust content is high (upper right).

DustyWave rest results, a resolution problem exists in which for

$$h_{grid} \geq c_s t_{stop} \tag{2.82}$$

dusty sound waves are inappropriately damped due to an inability to resolve the tiny phase difference between the gas and dust wave components.

Real dust grains. In realistic astrophysical dusty flows, there exist two major deviations from the model presented and analyzed above. First, the particles described above would be known as a monodispersion, with all grains having exactly the same size. Real dusty flows in nebulas and especially accretion disks are expected to span a very large range in size, from sub-micron sized particles to centimeters and eventually to boulders, asteroids and planetesimals.

The dynamic range represented by kilometer-class asteroids to the original circa 100nm sized particles believed to form as a supernova remnant enters the cold snowplow phase is a factor 10^{10} in size. Such a polydispersed flow cannot realistically be simulated with the fluid approach taken here as the number of dust fluid particle size bins required would be large and the computational burden excessive. Such situations are instead considered using either fully Lagrangian methods (gas and dust "particles") or with particle-in-cell (PIC) dust in a gridded fluid.

The second major issue, hinted at in the viscosity model discussion, is that real dust grains are not hard spheres. They aren't even soft spheres. In fact the growth process tends to lend itself initially to the creation of fractal "fluff" of often remarkably low fractal dimension (see again Mannel et al. (2016)). The main aerodynamic effect of this is to yield particles with stunningly low effective densities, and thus surprisingly short drag times.

CHAPTER III

NUMERICAL METHODS

Having presented the theory of the differential equations describing the physics GPU-Imogen can solve, now the numeric methods needed to solve them are described.

First methods for solving the fluid equations in one spatial dimension will be presented, followed by the natural operator splitting that extends the reliable one-dimensional solver to multiple space dimensions will be. Then a number of additional algorithms implementing the various non-ideal terms will be presented.

All of these algorithms have been implemented in the CUDA parallel programming language and extensively tuned to execute with high efficiency. The code is supported by two levels of test codes which provide full self-test assurance that everything is in working order.

Building blocks of Imogen. The size and complexity of the equations that Imogen attacks can easily seem overwhelming, especially if it is insisted to write the entire set out at once. Upon examination, the steps to evaluate this enormous set of equations can be broken into a tree like structure whose individual leaves are tractable and practical to evaluate.

The first and most important building blocks are those that solve the Euler equations. This requires the discretization of the Euler equations (2.27) into a form suited for numeric solution.

$$\partial_t \vec{u} + \partial_x \vec{F}(\vec{u}) + \partial_y \vec{G}(\vec{u} + \partial_z \vec{H}(\vec{u}) = \Gamma(u, ..., t) \qquad (3.1)$$

where

$$\vec{F} = \left[\rho v_x, \rho v_x^2 + P, \rho v_x v_y, \rho v_x v_z, v_x(E + P)\right] \tag{3.2}$$

$$\vec{G} = \left[\rho v_y, \rho v_y v_x, \rho v_y^2 + P, \rho v_y v_z, v_y(E + P)\right] \tag{3.3}$$

$$\vec{H} = \left[\rho v_z, \rho v_z v_x, \rho v_z v_y, \rho v_z^2 + P, v_z(E + P)\right] \tag{3.4}$$

into a form suited for numerical solution. While discretizing any one of flux terms in (3.1) stably and with second order accuracy is not excessively difficult to do, methods to do so simultaneously in two or three dimensions, which are known as unsplit methods, are substantially more difficult and for reasons described in the operator splitting subsection are not used in the code.

The 1D problem

$$\partial_t \vec{u} + \partial_x \vec{F}(\vec{u}) \tag{3.5}$$

can be efficiently solved with three building blocks: a flux assignment scheme (FAS) and a reconstruction algorithm to provide a stable space discretization, combined with a standard time integration scheme for the resulting system of ODEs. Once these are developed, the operator splitting which permits extension to multiple space dimensions is presented. Finally, the solvers which handle source terms and their part within the operator-split scheme are described.

Flux assignment scheme (FAS). The one-dimensional flux assignment scheme (FAS) is a formal implementation of the map

$$F := (\vec{u}_L, \vec{u}_R) \to \vec{F} \tag{3.6}$$

That is, it maps a presumed-constant left and right fluid (or other conservation law) state onto the resulting flux through the location of the original discontinuity.

One option, certainly, is to actually compute the true solution for the flux through $x = x_0$. For constant fluid states u_L and u_R this is known as a (1D)

Riemann Problem. It is the case that the true flux from a Riemann Problem of this type is constant (for a finite time), and one option for flux assignment is to "just" solve it, with $\vec{RP}$ representing the exact solution to the problem:

$$\vec{F} = \vec{RP}(\vec{u}_L, \vec{u}_R)_{x_0}. \tag{3.7}$$

In simple cases, such as a single ideal gas, an exact solution has been available for a long time. And recently, completely general exact results have become available for more complex systems (such as ideal MHD, Takahashi and Yamada (2013)).

However, even for a simple ideal gas, the exact solution requires a number of branching if-else decisions and worse yet, the numeric solution of a transcendental algebraic equation. This is rather problematic for an equation that must be solved twelve times per cell per timestep in a 3D problem, and more over represents a waste of time solving fine detail that will just be absorbed by averaging over two blobs anyway.

It is for this reason that considerable attention was historically focused on the development of approximations to $\vec{RP}(\vec{u}_L, \vec{u}_R)$.

The original proposition to treat the flux calculation as a Riemann problem was presented by Soviet physicist Sergei Godunov (Godunov and Ryabenki (1964)), for which these methods based on the breakdown of a discontinuity into a fan of primitive waves are named. Godunov methods are a subset in the broader classification of known schemes of a type known as *flux difference splitting* or FDS.

These, again broadly speaking, decompose the flux emitted from the decomposition of the RP into a series of different waves. Godunov solvers - either exact or approximate - represent one physically valid way of computing the flux in this manner.

Another major subset of FDS methods involves a decomposition of the form

$$\vec{F} = \frac{\partial \vec{F}}{\partial \vec{u}} \partial_x \vec{u} = \mathbf{A}\vec{u}' \tag{3.8}$$

in which an appropriate Jacobian $\mathbf{A}$ is determined by some method, at which point the problem is reduced to one of linear algebra and eigenvalue/eigenvector expansion. Methods of this type are generally known as Roe methods for their introduction by Phillip Roe in Roe (1981).

The second broad strategy subsumes methods known as flux vector splitting methods, after van Leer (1982), and include the well known AUSM (Advection Upstream Splitting Method) family of methods and its descendents/improvements. These propose to compute the flux vector directly, and then break the vector up into its upwind and downwind components (i.e. to split the vector). This is advantageous over Godunov methods in the sense that complex, often computationally intense models of the physical RP are avoided. It is particularly advantageous when facing a problem for which the characteristic decomposition is unknown, or is very complex (e.g. the page-filling decision tree for the completely general ideal MHD's RP solution given in Takahashi and Yamada (2013)) as it is not required to explicitly know the characteristics, or the Jacobian/eigenvalues/etc.

The GPU-Imogen code implements the well-known HLL (Harten-Lax-van Leer) and HLLC (HLL with Contact) approximate Riemann solvers.

Properties of HLL/HLLC. The HLL (Harten, Lax, and Leer (1983)) and HLLC (Toro, Spruce, and Speares (1994)) methods are golden classics in approximate solution of the Euler equations.

The HLL method assumes that a single intermediate state (and associated intermediate flux value) exist when the RP discontinuity decomposes, while the
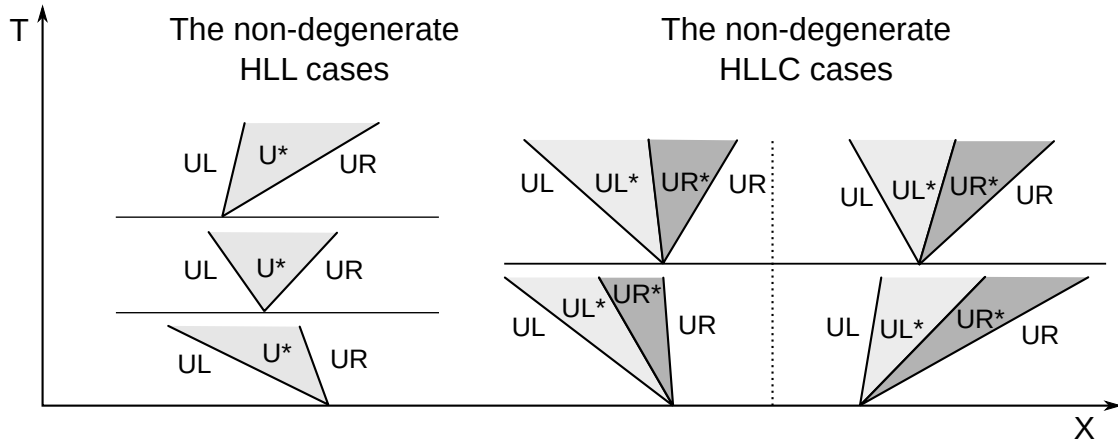
Figure 7. Graphic depiction of all non-degenerate (all wavespeeds unique) outcomes for the HLL and HLLC approximate Riemann solvers. Shaded regions have interacted with the emitted waves. Black angled lines trace wave front speeds. HLL has two, S_L and S_R, and HLLC has a third, S^*, defined by the requirement that the separation between U_L^* and U_R^* be a contact discontinuity. The HLL cases, bottom to top, are those of supersonic leftgoing convection, subsonic convection, and supersonic rightgoing convection. The HLLC cases, clockwise from bottom left, are supersonic leftgoing convection, subsonic leftgoing convection, subsonic rightgoing convection, and supersonic rightgoing convection. Degenerate cases: Both methods, with appropriate choices of wavespeeds, capture stationary shocks (vertical characteristic line) exactly, in which case the change in state across the other characteristic line(s) vanishes. In the case of HLLC, this also implies that $S^* \to S_{\text{not shock}}$.

HLLC method assumes that two (a left and right) intermediate states exist, and that the separation between them is a contact discontinuity.

These methods must be given as input values for the left and right wave speeds; They make no prescription for them. In order that the resulting fluxes be physical, the input wave speed estimates must bound the physical waves departing from the RP (i.e. the leftgoing wavespeed estimate must go left faster than any wave from the exact solution, and similarly the rightgoing estimate). The recommended choice of wavespeeds given in Batten, Clarke, Lambert, and Causon (1997) satisfies these requirements, and furthermore captures stationary shocks exactly for HLL, and stationary shocks and contacts exactly for HLLC.

Because of these properties and other desirable outcomes such as positivity preservation and physicality of the resulting flux, GPU-Imogen uses the wavespeeds given in Batten et al. (1997) Eq. 51.

Positivity preservation is a property of a numeric method that, given a transported scalar ϕ which has evolution equation

$$\partial_t \phi + \partial_x v(x,t)\phi = 0 \tag{3.9}$$

then

$$\phi(x,0) > 0 \rightarrow \phi(x,t) > 0 \ \forall \ t > 0 \tag{3.10}$$

The intuitive explanation is simple - If we start with some ϕ everywhere and can only move it around, obviously a situation cannot be arranged with less than no ϕ. In the Euler equations, the mass density is such a scalar, as is the total energy.

In simulations which may have extremely large dynamic ranges in these variables (e.g. the gas disk used to test some of the solvers has a dynamic range in density of 10^8, the assurance against unphysical outcomes is very valuable.

1D State Reconstruction. Once a method to assign a flux to an interface given the interface's two states $\vec{u}_L$ and $\vec{u}_R$ is available, the next step is to consider how to compute the left and right states abutting the cell boundary.

For labelling purposes, suppose we are interested in the state at the interface between cells i an $i + 1$, designated $i + 1/2$. The $1/2$ implies constant cell spacing, though this is not required and the extension to non-uniform cell spacing is not difficult to intuit.

The labelling has at times proven quite confusing: the *left* state is the *right* side of cell i and the *right* state is the *left* side of cell $i + 1$.

The obvious and simplest method is to consider the states of cells as piecewise constant,

$$\vec{u}_L = \vec{u}_i \tag{3.11}$$

$$\vec{u}_R = \vec{u}_{i+1} \tag{3.12}$$

This is a good idea if we believe that there is a shock present in cells i or $i + 1$ where the true solution $\vec{u}(x,t)$ jumps discontinuously and no derivative can reasonably be approximated. But if $\vec{u}(x,t)$ is assumed to be smooth as it generally is almost everywhere in a real flow, this is a poor idea because clearly for cells of size h we are making an error of order h.

However, any naive attempt to use cells in the vicinity of $\vec{u}_i$ to compute $\vec{u}_i'$ is destined to fail, in the sense that success means not oscillate. A tendency of a solver to introduce oscillations (new extrema) is here defined as a failure in the sense that the true solution never does this, and the introduction of oscillations is infamous for leading to the catastrophic failure of numerical schemes for the Euler equations.

The problem is depicted schematically in figure 8. While that uses central differences, there is always a particular slope that will break any linear scheme. Backward differences and left-biased weights in general will fail at negative steps, while forward differences and right-biased weights in general will fail at positive steps. This inevitable failure of any attempt to build a stable higher-than-first-order method out of *linear* corrections is embodied in the Godunov Theorem, which states that stable (monotonicity preserving) linear methods can be of at most first order accuracy.

The keyword permitting a run-around of Godunov's theorem is "linear." If a correction could be introduced that were a *nonlinear* function of cell values (and
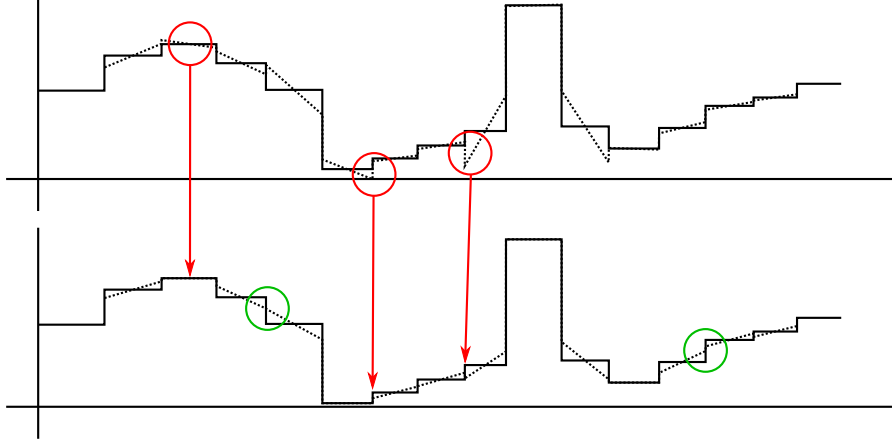
Figure 8. Results of extrapolating from cell centers to edges using naive central-difference linear slopes (top) and with the van Leer slope limiter (bottom): Note that the disastrous monotonicity-violating overshoots are cured, while the slopes in smooth regions are still smooth.

approximate derivatives found from them) at and around a given cell, it may be possible to construct stable higher order methods.

Slope limiter functions. The total variation of a function defined at points y_i is defined by the sum of absolute value of successive differences,

$$TV(y) = \Sigma_i |y_{i+1} - y_i| \tag{3.13}$$

This applicability of this property to the Euler equations was introduced in Harten (1983) under the name Total Variation Not Increasing (TVNI) which is now known better as Total Variation Diminishing (TVD). This is one of the central properties of solution of the Euler equations to the point that it, or a close relative, is now built into nearly all schemes for solving them.

The enforcement of monotonicity by synthesizing two (or potentially more) "naive" derivative approximations into a trustworthy estimate that does not induce oscillation is described in great detail in van Leer (1982), who described several slope limiters which are still in widespread use. Sweby presented a detailed

description of the operation of the slope limiter in terms of the ratios of adjacent derivatives and introduced the Sweby Plot to describe slope limiters, along with a number of slope limiter functions, in Sweby (1984).

A slope limiter accepts two 'plausible' corrections for what the interface state might be extrapolated to - such as the naive forward and backward differences - and returns a slope such that the now piecewise-linear reconstruction, when plotted, is guaranteed to maintain monotoncity and positivity.

Limiter functions are generally presented in dimensionless form, acting on the *ratios* of adjacent derivatives, e.g. $\phi(a,b) \to a\phi(1, b/a) = a\phi(r \equiv b/a)$. If the proposed corrections a and b have opposite signs, $r < 0$, we don't know what the slope is really doing, and must assume it to be zero for safety: all limiters have

$$\phi(r \leq 0) = 0 \tag{3.14}$$

This in mind, some of the classic limiters include the minmod (ϕ_{mm}) and superbee (ϕ_{sb}) limiters which bound all other 2nd order limiters, the van Leer limiter (ϕ_{VL}), the Ospre limiters (ϕ_{Osp}), the van Albada limiter (ϕ_{VA}) and the monotized central (MC) limiter (ϕ_{MC}):

$$\phi_{mm}(r) = \begin{cases} 1, & r > 1 \\ r, & r \leq 1 \end{cases} \tag{3.15}$$

$$\phi_{sb}(r) = \begin{cases} \phi_{mm}(2r), & r < 1 \\ 2\phi_{mm}(r/2), & r \geq 1 \end{cases} \tag{3.16}$$

$$\phi_{VL}(r) = \frac{2r}{1+r} \tag{3.17}$$

$$\phi_{Osp}(r) = \frac{1.5(r + r^2)}{1 + r + r^2} \tag{3.18}$$

$$\phi_{VA}(r) = \frac{r + r^2}{1 + r^2} \tag{3.19}$$

$$\phi_{MC}(r) = \max[0, \min(r, (1+r)/2, 2)] \tag{3.20}$$
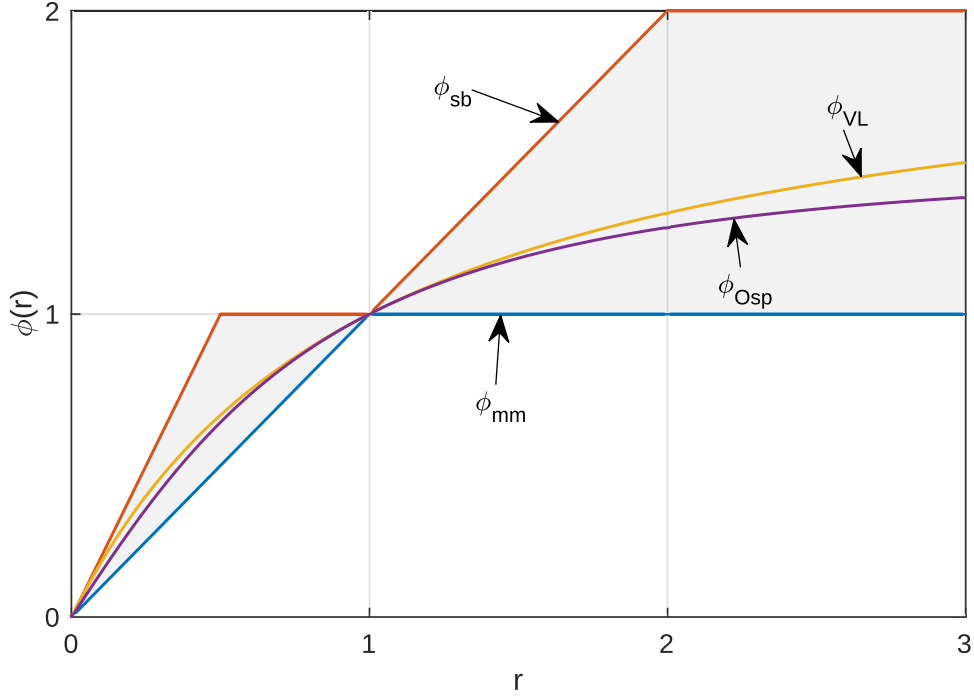
Figure 9. Sweby plot showing the 2nd order TVD region (gray shaded) as well as the Minmod, Superbee, van Leer and Ospre slope limiter curves. For all limiters, $\phi(r < 0) = 0$. The region $0 \leq \phi < \phi_{mm}$ is TVD but it is not second order; In particular, the curve must pass through $\phi(1) = 1$ to exactly reconstruct a linear input, as a 2nd order scheme must.

PLM reconstruction encounters a problem at legitimate extrema, because at them adjacent derivatives have opposite signs. This forces the slope limiter to return zero derivative, such that the reconstruction at extrema is first order. Thus, second-order methods using PLM reconstruction suffer first-order accuracy at extrema, and thus (asymtotically) the convergence plots tend to deviate from second order.

A very desirable property of the slope limiter is symmetry. The Euler equations are even under parity, but if the state reconstruction lacks the property

that

$$\phi(u'_a, u'_b) = \phi(u'_b, u'_a) \tag{3.21}$$

then the calculation will break mirror symmetry. All of the limiter above and implemented in GPU-Imogen are symmetric.

Reconstruction algorithm. Given a choice of slope limiter $\phi(a, b)$ and a uniformly spaced set of variables u_i, the reconstruction algorithm used is as follows. The division by h that would yield derivatives is dropped since the next step just multiplies by $h/2$ again.

(1) Form the simple backward and forward differences,

$$BD_i = u_i - u_{i-1} \tag{3.22}$$

$$FD_i = u_{i+1} - u_i \tag{3.23}$$

(2) Find the nonlinearly limited slope

$$u'_i = BD_i\phi(FD_i/BD_i) = \phi(BD_i, FD_i) \tag{3.24}$$

(3) The desired state information for the cell boundary is then

$$u_{L,i+1/2} = u_i + \frac{1}{2}u'_i \tag{3.25}$$

$$u_{R,i+1/2} = u_{i+1} - \frac{1}{2}u'_{i+1} \tag{3.26}$$

Now that we are equipped with the machinery to compute the fluxes through cell boundaries given their interface states, and the algorithm to compute those interface states, the spatial part of the one dimensional Euler equations is fully discretized.

Time integration methods for conservative equations. With a slope-reconstruction algorithm and a flux assignment scheme, we have a reliable method of mapping a series of states $\vec{u}_i$ onto the instantaneous fluxes at their

59

interfaces $\vec{F}_{i+1/2}$. Thus taking the cell-average values $\vec{u}_i$ as discrete variables sampling the true solution $\vec{u}(x,t)$, these two parts provide a stable and accurate discretization of the spatial part of the Euler equations.

Through the finite volume integral transform (2.1) this yields the time derivative of the discretized system,

$$V\frac{d\vec{u}_i}{dt} = \sigma_{i-1/2}\vec{F}|_{i-1/2} - \sigma_{i+1/2}\vec{F}|_{i+1/2})$$ (3.27)

where having assumed that we are in an Eulerian frame and that the geometric elements remain unchanged we can move the volume V and interface cross sections σ outside of the derivative signs.

As is almost always done for PDE evolution equations, we have translated the non-time part of the equation into a discrete form and left the time part continuous in order to apply the Method of Lines. This yields a very large and sparse system of nonlinear, coupled ODEs at which any applicable ODE method may be thrown.

Because of the inescapable constraints imposed by $\delta t \approx c\delta x$, the increased storage required by high-order temporal methods is seen as insufficient to justify implementing them for the main fluid equations.

By exploiting certain coincidences in the evaluation of the 2nd order Runge-Kutta methods (both the explicit midpoint and explicit trapezoid) Imogen requires only one temporary storage array ($5 \times$ number of cells) to solve the discretized equations with second time order accuracy.

A third time order Runge-Kutta method has been implemented, but shows no improvement in the convergence characteristics. This indicates that the spatial discretization error almost always dominates the temporal one. This is not surprising: The *time* step is limited by the time for a wave to propagate one cell,

but the smallest wave-like structure in *space* that is usefully resolved is around twenty cells long.

Temporal methods for the Euler equations in GPU-Imogen.

The space of all possible methods for marching an ODE solution forward in time, i.e. to generate approximate solutions to the continuous equation

$$\frac{du}{dt} = F(u) \tag{3.28}$$

where u is a vector of solution points, and F is a vector valued function, is enormous.

Let the solution vector at the Nth time point be denoted u^n. Systems which compute u^{n+1} using $u^{n,n-1,\ldots n-s}$ are called multistep methods. Those based on linear combinations of $F(u^{n+k})$ with $-1 \leq k < s$ are the linear multistep methods:

$$u^{n+1} - u^n = \sum_{k=-1}^{s} \alpha_k F(u^{n-k}) \tag{3.29}$$

When α_{-1} is nonzero, the method is implicit. The explicit LMMs - with equal timesteps - are known as Adams-Bashforth methods. The first two are

$$u_i^{n+1} = u_i^n + tF(u^n) \tag{3.30}$$

$$u_i^{n+1} = u_i^n - \frac{t}{2}F(u^{n-1}) + \frac{3t}{2}F(u^n) \tag{3.31}$$

Unfortunately, even at second order, the α vector contains negative entries, a matter which to say the least does not improve at higher orders. This is a fatal problem for solving the Euler equations, because if the 2nd order Adams-Bashforth is considered as a sum of two Euler steps, one step has a negative timestep. Negative timesteps (or, as here, negative stage weights) are not acceptable when solving the Euler equations because the Euler equations are not time reversible.

The reason that methods with all-positive weights are so important is because of the TVD theorem (Harten et al. (1983): If the spatial method is

TVD, then forward Euler steps are monotonic and stable; If in addition the flux is physical, a forward Euler step is guaranteed to output a physical state. Because convex weights of stable methods (and physical cell states) are themselves guaranteed to be stable (and physical), higher order methods with convex weights are the key to building methods that have higher time order accuracy without sacrificing stability in space.

The TVD condition is an example of a *strong stability preserving* property. Numeric methods that have the strong stability preserving (SSP) property at high time order are an active area of research; See e.g. Kennedy, Carpenter, and Lewis (2000), and Ketcheson (2008).

However, since the spatial discretization in use is only second order accurate, classic results for second-order SSP methods are sufficient. All explicit second order RK methods can be parameterized by the choice of a single parameter α in the following scheme:

$$u_i^\alpha = u_i^n \qquad\qquad\qquad\qquad\qquad +\alpha t F(u_i^n) \qquad (3.32)$$

$$u_i^{n+1} = u_i^n \qquad\qquad +(1 - \frac{1}{2\alpha})t F(u_i^n) + \frac{t}{2\alpha}F(u_i^\alpha) \qquad (3.33)$$

which is convergent for $\alpha \in (0, 1]$, though evidently the full step weights suggest that α not be too small. Named choices of α include the explicit midpoint method ($\alpha = 1/2$), Ralston's method ($\alpha = 2/3$) and Heun's method (aka explicit trapezoid), $\alpha = 1$.

Of these, the explicit trapezoid is unconditionally stable and nonoscillatory (TVD) for the largest timestep, all the way to the maximum timestep permitted by forward Euler. It is for this reason that the trapezoid is the default time method for the Euler equations in GPU-Imogen, though the explicit midpoint may be selected when GPU modules are compiled if for some reason desired.

Furthermore, the trapezoid method is observed to be substantially more reliable than the midpoint method at handling corner cases. E.g., tests find that the midpoint is likely to crash and cause a checkpoint restore (which also automatically shrinks the CFL prefactor described below) when running the the Einfeldt and double-blast test problems, while the trapezoid never does this even for a CFL of 0.85.

Adaptive timestep control. Previous sections have developed the spatial and temporal discretization for the 1D Euler equations, however the explicit methods used have well known limits upon their stability when the timestep is increased. Because of this, and our desire to take the largest practicable timestep because timesteps cost a lot of wallclock time, adaptive timestep control is mandatory.

This requirement to limit the timestep δt given a space step δx for an explicit method is known as the CFL condition, after the seminal work of Courant, Friedrichs & Lewy who in 1928 demonstrated for various classes of PDEs (Elliptic, parabolic and hyperbolic) that convergence of time methods was often conditional upon the ratio of time step to space step.

The CFL of a discretized PDE encodes the maximal local eigenvalue of the resulting system of ODEs, which goes directly to the stability of conditionally stable methods (which includes all explicit linear methods) in in the form that stability requires that $\lambda_{max} t \ < \$ const. This constant, now called the CFL constant, was originally derived by Courant, Friedrich and Lewy in 1928 for several categories of discretized PDEs in **?**, translated to English in **?**.

The CFL limit, by dimensional analysis, is a constant times the ratio of the space step to information speed (for equations which have real, finite information

speeds):

$$t_{\text{CFL}} = \beta^{max} \times \min(\frac{h}{c_{\text{fastest}}}) \qquad (3.34)$$

For explicit discretizations of hyperbolic systems, it is typically in the vicinity of one. Matters beyond this point become confused by the common use of the same term, usually a phrase like "Simulation X was run at a CFL of 0.7," to potentially refer to any of several things, all related to the details of the numeric method. One, β^{max} may refer to the largest *forward Euler* timestep which has the TVD property. Two, it may refer to the largest timestep for the time integrator being used which is TVD. Third, it may refer to the largest timestep for the chosen integrator which is stable under some other stability criterion which is *not* the TVD condition (e.g. TVB, total variation bounded).

A better intuitive understanding can be gained using one of the ideas of the original Courant paper, information propagation and domain of dependence. For the Godunov scheme, we can imagine that when the fastest moving information (fastest wavefront) has traversed one half of a cell, it is possible that it could collide with a "partner" that has reached the center of the same cell from the other side. At this point, it is not guaranteed that these waves cannot interact to generate a faster wavefront propagating back to one of the interfaces, thereby rendering the original calculation of the flux invalid and the method potentally unstable.

Based on this reasoning, we can understand the von Neumann result that under meaning 1, Godunov methods have $\beta^{max} = 1/2$. If the time integrator, however, is chosen to be explicit midpoint, it will be observed that the method is only TVD for $\beta^{max} \leq 1/4$, and becomes TVB for values between 1/4 and 1/2.

However this introduces practical problems. If a different numeric method were selected (or implemented), then suddenly all simulations with β prescribed may find themselves being either excessively conservative, or in unstable territory.

It is for this reason that GPU-Imogen utilizes the second meaning: The code accepts input values of `run.cfl` which lie on the interval $(0,1)$ where 1 refers to the β^{max} *for the chosen spatial and temporal discretization* which preserves the TVD property.

All other time evolution operators in the code also have an associated CFL-equivalent property. For example, a stationary gravity potential ϕ has the condition that

$$|\frac{1}{2}adt^2| = \frac{1}{2}|\nabla\phi|dt^2 < dx, \tag{3.35}$$

i.e. that the timestep may not be large enough for gravity to make a fluid parcel freefall further than an entire cell within a single timestep. As in this case $dt \propto \sqrt{dx}$, such a condition is not considered relevant to be worth checking.

Other limits which exist are handled in a manner that prevents them imposing global constraints: The radiation limit ($\Gamma dt <\approx \epsilon_{internal}$) is handled per-cell by nonlinearly stopping cooling at a temperature floor. The gas-dust coupling time ($k_{drag}dt <\approx 1$) is evaded by performing coupling with an unconditionally L-stable method described below. Technically a limit exists as well due to the frame terms in cylindrical coordinates and/or rotating frames of reference, but these are tied to angular change per unit time; Unless the azimuthal grid has literally a single-digit number of cells, the normal CFL limit assuredly satisfies them.

Operator splitting.   Extending the one-dimensional prescription to two or three dimensions with *first* spatial order accuracy is exactly as simple as one may imagine: Just sum the time derivatives resulting from each of the $\vec{F}$, $\vec{G}$

and $\vec{H}$ operators, or more generally just compute the flux through every face, and use their differences to perform a multi-dimensional conservative update.

However, the edges/corners of cells can create a strongly-interacting region of the local solution. Handling this requires that a multi-dimensional scheme of higher than first order compute fluxes not pairwise at edges/faces, but at each corner using data from all four quadrants (or eight octants) touching that corner in the locally orthogonal coordinate system.

Unsplit schemes certainly, of course, exist but their implementation onto the chosen parallel architecture appeared quite daunting and so the dimension split approach was used.

Operator splitting theory. In the split approach, $\vec{F}$, $\vec{G}$ and $\vec{H}$ are treated as separate propagators for the system's state, and operator algebra shows how individual (i.e. 1D) methods can evolve the combined $(\vec{F} + \vec{G} + \vec{H})$ propagator with second order accuracy

The idea of dimension splitting was rigorously analyzed by Strang in Strang (1968) which considered the case of a two dimensional linear constant coefficient hyperbolic PDE,

$$u_t + Au_x + Bu_y = 0 \tag{3.36}$$

for two non-commuting matrices A and B. In the case of the Euler equations, for smooth solutions, A and B would be the flux Jacobians in two orthogonal directions expanded about the current fluid state. Per Strang, the evolution of u can be expanded as a power series in time,

$$u = u_0 + t(Au_x + Bu_y) + t^2(A^2u_{xx} + (AB + BA)u_{xy} + B^2u_{yy})/2 + ... \tag{3.37}$$

if we assume that u is smooth and exchange mixed partials with abandon. If the series were continued it would be seen that this expansion computes the exponential of the operator,

$$u(t) = u_0 \exp((Au_x + Bu_y)t) \tag{3.38}$$

If we consider that for the Euler equations Au_x and Bu_y are just the fluxes in the x and y directions, let us replace them with $F/G/H$ representing the discretized $x-$, $y-$ and $z-$ direction flux differences.

Two means of constructing a multi-dimensional method (or more generally, a solver for a splittable operator) out of one-dimensional methods (sub-operators) work well. Both operate by generating terms which agree with the terms in expansion (3.37) to some order.

One consists of applying various sub-solvers (which exactly or approximately calculate the exponential of sub-operators) with scaled timesteps, where the list of operators and timestep scale factors is cleverly chosen to arrive at its end having generated the first N terms of (3.37).

To save space, let the letters refer to the exponential of the operator rather than the operator and numeric multiplicands to scaling the operator being exponentiated. In other words, "$F/2$" would mean $\exp(tF/2)$ or "Evolve the F operator by half a timestep."

Then the simplest operator splitting is of first order accuracy, and consists of just solving for the sub-flows, one by one, in any order:

$$u(t) = F * G * H * u_0 + O(t^2) \tag{3.39}$$

where $O(t^2)$ is the local truncation error (the global error being one order worse, as the $O(t^2)$ error is compounded by $N\,t$ timesteps). The requirement for 1st order

accuracy is that the coefficients on every individual operator add up to unity, which is also called consistency.

For any two operators F and G, it is easy to show by direct expansion of $\exp((F+G)t)$ and comparison that

$$u(t) = F/2 * G/2 * G/2 * F/2 * u_0 + O(t^3) = F/2 * G * F/2 * u_0 + O(t^3) \quad (3.40)$$

forms a method that is second order accurate in the splitting. This is the *Strang splitting*. The *order* of error is the same, but it's worth nothing that the actual error term coefficients in the expansion (there are eight) differ.

By induction it can be seen that any such first-order stringing together of subsolvers can be upgraded to second order by repeating the sequence in reversed order,

$$u(2t) = A_1 * A_2 * A_3...A_n * A_n...A_3 * A_2 * A_1 * u_0 + O(t^3) \quad (3.41)$$

Operator splitting has found great application in N-body direct solvers, in which the N-body Hamiltonian $H = T(p_i) + U(x_i)$ has two parts which are easy to exactly evaluate individually - the change in position due exclusively to momentum, and the change in momentum due exclusively to position, commonly called "drift" and "kick" - yet perniciously difficult to evaluate at high order simultaneously.

A more general approach in splitting is called Multiple Product Splitting (MPS). This expands the toolbox from products of suboperators to sums of products. An example of a second-order accurate MPS from two first-order products is

$$u(t) = \frac{1}{2}(F * G + G * F)u_0 + O(t^3). \quad (3.42)$$

Like the above method (3.40), this is of second global order but the error terms differ considerably.

For any set of operators and a proposed product method, it is not knowable a priori, in general, what order of method can be constructed: Given the step fractions as parameters, the requirement that the first P terms in (3.37) agree will generate an exponentially growing number of constraints. The use of summation in addition to products introduces new free parameters which can potentially help satisfy constraints when searching for high order methods. Solvers for irreversible equations, such as the fluid equations, suffer particularly because non-reversibility forbids negative timesteps.

There are generally 8 third order terms in a splitting of two operators (ranging from AAA to BBB). If second order methods are symmetrized by averaging over permutations of their constituents, then there are four distinct third order coefficients. One, corresponding to AAA and BBB, has no error if the individual propagators are solved exactly (as it corresponds to a one dimensional system).

Of the three second order methods given in (3.40) and (3.42), the Strang split ones can be symmetrized into the symmetric 2nd order method

$$u(t) = \frac{1}{2}(F/2 * G * F/2 + G/2 * F * G/2)u_0 + O(t^3) \tag{3.43}$$

This can be combined with the second order MPS method in a way that minimizes the third order error but does not eliminate it (as there are 3 coefficients but only two variables),

$$u(t) = \frac{1}{2}(\frac{13}{16}(F/2 * G * F/2 + G/2 * F * G/2) + \frac{3}{16}(F * G + G * F))u_0 + O(t^3) \tag{3.44}$$

which has slightly over half as much third order error (and no asymmetry in that error). However the price is a most unreasonable increase in the amount of work required - this method requires ten evaluations of the F and G operators, where the Strang splitting requires only three.

Operator splitting in GPU-Imogen. The operators that are split and solved in GPU-Imogen are the spatial fluxes (which may be in 1, 2 or 3 space dimensions), and any or all of a variety of other source terms, such as radiative loss as referred to in the introduction, multi-fluid coupling, gravitation and frame effects.

All source operators are grouped under a single symbol Γ, which represents the action of all the source operators (wherein any splittings must, themselves, be symmetrized).

By expanding the exponential of the operators and requiring that all 1st and 2nd order errors cancel, a one-parameter family of 2nd order methods is arrived at:

$$(\frac{k/2}{\Gamma}) * P(\{F, G, H\}) * ((1 - k)\Gamma) * \tilde{P}(\{F, G, H\}) * (\frac{k}{2}\Gamma) \qquad (3.45)$$

For values of $k \in [0, 1]$ (such that no attempt to run operators backward in time is made), a fully second order method of composing the space update where P and $\tilde{P}$ represent respectively a permutation and the reverse of that permutation (e.g. if $P = \{X, Z, Y\}$ then $\tilde{P} = \{Y, Z, X\}$).

The product formulation is chosen over the second order MPS because it is memory efficient. This is because it does not require creating multiple copies of the simulation state.

Without looking beyond second order, there is no way to decide which if any ordering of operators is "better." Because GPU-Imogen's solver for the

individual flux operators is only second-order accurate, it doesn't really matter. Based on the heuristic belief that one sequence may perhaps generate errors that partially cancel those from another, GPU-Imogen alternates spatial sweeps in 2D (XYYX, YXXY, ...) and cycles through all six permutations in 3D, both in a repeating determinstic pattern.

Application of gravitational potential and frame terms. It is found that the actions of gravitational potential, frame rotation, and cylindrical geometry source terms can be solved simultaneously with considerable efficiency and high-order time accuracy. These source terms are the following in Cartesian coordinates written as equations for velocity, evaluated with density ρ and positions held fixed:

$$\frac{d}{dt}\begin{bmatrix} v_x \\ v_y \\ v_z \end{bmatrix} = \begin{bmatrix} 2\omega v_y + \omega^2 x - \frac{d\Phi_g}{dx} \\ -2\omega v_x + \omega^2 y - \frac{d\Phi_g}{dy} \\ -\frac{d\Phi_g}{dz} \end{bmatrix} \tag{3.46}$$

and in cylindrical coordinates,

$$\frac{d}{dt}\begin{bmatrix} v_r \\ v_\phi \\ v_z \end{bmatrix} = \begin{bmatrix} 2\omega v_\phi + r\omega^2 - \frac{d\Phi_g}{dr} \\ -2\omega v_r - \frac{d\Phi_g}{d\phi} \\ -\frac{d\Phi_g}{dz} \end{bmatrix} \tag{3.47}$$

Because these terms act purely upon the kinetic energy of the gas, we do not need to numerically calculate an integral to track the total energy because we have an exact one at hand, namely that the change in total energy is simply the change in kinetic energy, which is trivial to calculate exactly ($.5\rho(v_{\text{final}}^2 - v_{\text{initial}}^2)$).

The reason that high time order accuracy is desired locally here, even though the fluid dynamic algorithm is only second-order space and time, is because these terms lack the intrinsically conservative behavior of conservation equations.

Depending on how they are solved they can, in fact, erroneously invent momentum and energy out of nowhere. This we desire to suppress to the greatest possible extent for long simulations.

The total gravitational potential (the static field, dynamic solution of Poisson's equation, and sum over fields from compact objects if any exist) is here assumed as a given, having been already evaluated at all points on the grid. The potential gradient is calculated using either 2nd or 4th order central difference stencils for regular grids with spacing h,

$$\frac{\partial f}{\partial x} = \frac{-f(x-h) + f(x+h)}{2h} + O(h^2) \tag{3.48}$$

$$\frac{\partial f}{\partial x} = \frac{f(x-2h) - 8f(x-h) + 8f(x+h) - f(x+2h)}{12h} + O(h^4) \tag{3.49}$$

These formulae and a litany of other finite difference, scattered-interpolation and mesh-metric formulae are given in Hyman and Larrouturou (1982).

Once the potential gradient is available, the problem becomes completely parallel because every cell is an independent problem. To acheive high order from few variables, Gaussian quadrature is adopted. By construction, Gaussian quadrature with s points exactly reproduces the integral of a polynomial of order $2s - 1$, and therefore has accuracy of order $O(2s)$. The 2nd order Gauss-Legendre method (one quadrature point) is the implicit midpoint method. The 4th order (GL-4) and 6th order (GL-6) methods are described below.

The only difficulties arise in solving for the X-Y or R-θ velocities, as the z equation is trivial (the only action in z is gravity). The in-plane variables represent a system of two equations. It has been found that Gauss-Legendre quadrature can be made to iterate a solution of these with extremely high efficiency on GPUs (acheiving nearly 80% of theoretical maximum mathematical throughput).

The Butcher tableau that must be solved for GL4 is

$$
\begin{array}{c|cc}
1/2 - \sqrt{3}/6 & 1/4 & 1/4 - \sqrt{3}/6 \\
1/2 + \sqrt{3}/6 & 1/4 + \sqrt{3}/6 & 1/4 \\
\hline
& 1/2 & 1/2
\end{array}
\tag{3.50}
$$

And that for GL-6 is

$$
\begin{array}{c|ccc}
1/2 - \sqrt{10}/15 & 5/36 & 2/9 - 1/\sqrt{15} & 5/36 - \sqrt{15}/30 \\
1/2 & 5/36 + \sqrt{15}/24 & 2/9 & 5/36 - \sqrt{15}/24 \\
1/2 + \sqrt{10}/15 & 5/36 + \sqrt{15}/30 & 2/9 + 1/\sqrt{15} & 5/36 \\
\hline
& 5/18 & 8/18 & 5/18
\end{array}
\tag{3.51}
$$

When referring to them abstractly below, the component names

$$
\begin{array}{c|c}
c_i & a_{i,j} \\
\hline
& b_j
\end{array}
\tag{3.52}
$$

will be used. With two equations, it can be seen that the 4th (6th) order methods will require solving a system of 4 (6) equations simultaneously. This requirement to solve $s \times N$ variables at once is what generally precludes the use of GL type methods for large coupled systems of equations (large N) despite their accuracy and stability properties.

The fixed point iterations are Gauss-Seidel like, but rather than backsolving rows in a matrix the nonlinear equations are manipulated directly. The equations for the p-th v_r are independent of v_r and yield "exact" stage values for v_r given the current estimates of v_ϕ:

$$
v_{r,p}^{(n+1)} = v_r^0 + \left[\sum_s a_{p,s}(r\omega + v_{\phi,s})^2/r + c_p\Phi_r \right] \tau
\tag{3.53}
$$

73

Next the equations for the p-th v_ϕ are sequentially solved for $v_{\phi,p}$,

$$v_{\phi,p}^{(n+1)} = \frac{v_\phi^0 - \left[a_{p,p}2v_{r,p}\omega - (1/r)\sum_{s<p}v_{\phi,s}^{(n+1)}(v_{r,s} + 2r\omega) - (1/r)\sum_{s>p}v_{\phi,s}^{(n)}(v_{r,s} + 2r\omega) - c_p\Phi_\phi\right]\tau}{1 + \tau a_{p,p}v_{r,p}/r}$$

$$(3.54)$$

The reciprocal factor suggests one obvious limit upon the radius of convergence, but this will never be encountered in practice because for that to happen the grid would have to extend within less than one radial cell size of $r = 0$ (The CFL timestep limit precludes $\tau v > h$).

The limitations on timestep imposed by the explicit CFD algorithm mean that the change here is in fact small; In practice, improvements in equilibrium holding (i.e. reduction of errors in the interior of an equilibrium fat gas torus) go away with only an explicit Euler first-guess and two iterations on a reference test case.

That the algorithm described here acheives performance at the price of generality: The structure of the specific equations of motion being solved is expressly manipulated to provide a very fast fixed-point iteration of the implicit system. There is an upper bound on the radius of convergence (and thus the stable timestep) but it is expected to be very large.

When the fluid is held in place (Due to operator splitting, all fluid transport is handled by the CFD routines) these terms act purely on the mechanical energy of the fluid and have no action upon its internal energy density. As a result the total energy equation can be solved exactly by simply subtracting the kinetic energy from total energy before and adding its new value after. This efficiently prevents a wide range of potential maladies associated with unphysical

states that could be created by truncation error if an approximation for total energy were used.

There are two "knobs" that control this method: The choice of 4th or 6th order time integration given the potential gradient, and the choice of the 2nd or 4th order spatial scheme to compute the potential gradient. When tested upon a prototypical application for this operator solver, a 3D gas disk in cylindrical coordinates with gravity and frame rotation, all three methods are associated with exceedingly low levels of error inside of the disk as imaged in $\log |\partial_t \rho|$. The exception occurs at the midplane, where the fluid solver inescapably is first order accurate (because density has an extremum - a maximum - there).

Application of multifluid drag. The equations of motion for drag-coupled gas and dust in astrophysically relevant regimes are given in detail in Laibe and Price (2011b) and produced previously in section II

Several solvers of two classes are implemented in GPU-Imogen: The classic explicit midpoint (EMP) and 4th order Runge-Kutta (RK4) methods, and three members of a family of exponential methods dubbed the LogTrap method.

Exponential Methods. The linear multistage methods are well known. The exponential method deserves some explanation. Exponential integrators are designed to approximate the general semilinear equation

$$y' = f(t, y) = Ly + nl(t, y) \tag{3.55}$$

where L may be either the linear part of the ODE or a linearization about the current state and nl is respectively either the nonlinear part or nonlinear residual. Details as well as the basis for the implementation in Imogen may be found in Caliari and Ostermann (2009).

The very short summary is, exponential methods are described by Butcher tableax except that the entries are now matrix-valued functions instead of scalars. In addition to the classical (nonstiff) order conditions which guarantee that the first N terms of the power series expansion are correct, exponential methods have stiff order conditions which determine their order of accuracy in solving the stiff (linear) part of the problem.

The exponential equivalent of the Euler method has the Butcher tableau

$$
\begin{array}{c|c}
0 & 0 \\
\hline
 & \phi_1
\end{array}
\tag{3.56}
$$

with the ϕ_1 function defined as

$$
\phi_1(x) = \exp[x] - 1.
\tag{3.57}
$$

This method has classical order two and stiff order one.

Assuming that the matrix exponential e^{Lt} can be computed effectively (in general this is an *extremely* bad assumption), it should not be surprising that under that condition such methods can potentially have substantial advantages in computational efficiency (accuracy per work done).

Historically matrix exponentials have been very troublesome to compute numerically (Moler and Van Loan (2003)), especially when finite difference operations create large, sparse matrices. In the case being considered here, though, where the stiff action is that of force directly opposite to the direction of relative motion, with all cells independent, it is very easy to solve the matrix exponential because if the instantaneous relative velocity decay time is defined using

$$
k = -F_{drag}(v_{gas} - v_{dust})/(v_{gas} - v_{dust}).
\tag{3.58}
$$

then the L in (3.55) is simply $L_{ij}(t) = diag(-k, -k, -k)$.

LogTrap Method. In reality, the drag coefficient itself is generally dependent on the relative velocity. If the timestep is large enough that the drag coefficient changes greatly during the span of a single timestep, the drag regime can become extremely nonlinear as the rate of change of L itself begins to seem stiff.

The evolution in L has no negative impact upon stability because we know *a priori* that none of the eigenvalues will flip sign: drag may get weaker but it's not going to turn into a magic free energy source where drag makes particles accelerate.

The detrimental effect of a rapidly changing L to a method such a ETDKR1 is the degradation of the accuracy of the numeric solution because the drag is not accurately modelled over the interval being integrated during a given timestep.

A novel method for addressing this condition implemented in GPU-Imogen is deemed the *LogTrap* method (for LOGarithmic TRAPezoid). If we are solving a nonlinear ODE

$$y' = -k(y)y \tag{3.59}$$

, obviously the general nonlinearity will preclude exact solution. The logtrap idea is that if an interpolating polynomial $k_p(t)$ can be constructed instead with the property that

$$k_p(t) = k(y(t)), \tag{3.60}$$

then a very simple exact form emerges, that

$$y(t) = y_0 e^{-\int_0^t k(t)dt} \tag{3.61}$$

77

Of which the case of linear drag can be seen is the case of $k_p(t) =$ constant. In the simplest case, that of measuring k once at $t = 0$, the resulting first-order LogTrap method (LT1) yields linear exponential decay and is equivalent to the exponential Euler method (for the case (3.59), ETD methods are more broadly applicable).

The second-order logtrap method uses k_0 to advance to time t and compute k_1 there (then k_1 incurs a locally second-order truncation error), and the result is

$$y_{lt2} = y_0 e^{-(k_0+k_1)t/2} \tag{3.62}$$

such that k_p is a linear interpolant. This is where the name comes from, because it applied the Trapezoid method to the Log, or in shorthand LT2.

Further improvement in accuracy may be affected by using this (globally) 2nd order approximation to advance y_0 to $y_{1/2}$ and compute $k_{1/2}$. Now in possession of three points, Richardson extrapolation yields Simpson's rule,

$$y_{lt3} = y_0 e^{-(k_0+4k_{1/2}+k_1)t/6} \tag{3.63}$$

Assuming the evaluation of the individual k values is stable, because the weights are convex this method (LogSim?) is also clearly L-stable for positive timesteps when applied to problems of the form (3.59).

Both the ETD and the LogTrap methods are examined by the DustyBox test in the implementation test descriptions. The use of Richardson extrapolation or fancier RK tableaux to derive more points and better quadrature rules could be continued, however the LT3 algorithm already has sufficient accuracy (and to spare) that global error is dominated by other operators and operator splitting error.

Challenges for strong drag. Strong gas-dust coupling (short drag time) in a multifluid flow is a famously difficult problem to handle numerically.

When the coupling term becomes extremely strong it becomes problematic to consider the system from the standpoint of two fluids coupled by a perturbing drag. In Laibe and Price (2014), Laibe & Price present the opposite angle formalism of a single fluid containing fractional components ϵ_k with perturbed velocities δv_k. Unfortunately, this would have required rewriting the entire Godunov solver from the ground up and was considered as presenting rather too much of an implementation challenge.

CHAPTER IV

PARALLEL IMPLEMENTATION

Now more than ever, large numeric problems are not solved by serial processors running faster (if for no other reason than that multiple physical limits prevent them from running any faster) but by more processors running in parallel. The gpu-Imogen code, as its name suggests, takes advantage of the parallel processing facilities of nVidia Tesla GPUs, which provide banks of hundreds or thousands of tightly coupled parallel processors in the space of a standard video card. The code is capable of using any or all of the GPUs available on a node, and also runs in parallel on multiple nodes using MPI.

This problem is solved by a hierarchical arrangement in which the whole space being simulated is distributed among processor nodes, which in turn distribute it among their GPUs. In turn, the GPUs each distribute their local processing tasks among tens or hundreds of *streaming multiprocessors*, each of which have a hundred float point units at its command.

All processing that the code performs upon the distributed fluid (and/or ancilliary data) arrays is fully parallelized. Here some underlying ideas in parallel code speedup are presented and the code's performance is compared under a variety of conditions.

Types of parallel speedup. There are two forms of speedup of interest: Strong scaling and weak scaling. If $T(s, n)$ denotes the execution time for a program doing w amount of work on n processors, *strong scaling* asserts that

$$T(w, n)_{\text{strong}} = T(w, 1)/n, \tag{4.1}$$

that is, that a problem of fixed size runs faster and faster as more resources are thrown at it. Most algorithms that exhibit this behavior are known as trivially

parallel: There is no dependency at all between calculations, so dividing them up to more processors is extremely simple. An example of such would be the calculation $y_i = f(x_i)$ for $i \in [0, N)$.

Inevitably weak scaling breaks down at some point once an irreducible atomic unit of calculation is reached. In the vector mapping example just given, clearly the simple distribution of a job of size M to N processors will encounter problems when $N > M$.

A program which exhibits *weak scaling* behaves with the property that

$$T(nw, n)_{\text{weak}} = T(w, 1), \tag{4.2}$$

that processing time remains the same as the job is scaled so long as work per processor remains constant. This avoids the endpoint of strong scaling where some indivisible unit of work is eventually encountered.

An algorithm which does not parallelize what so ever would have the relation

$$T(w, n)_{\text{serial}} = T(w, 1). \tag{4.3}$$

An example of such would be a calculation of the form $y_{i+1} = f(y_i)$, which includes ODE initial value problems (IVPs). The calculation of multiple y_i at once cannot possibly be done, because each new y depends on every previous y.

Real computations will contain both parts that can be parallelized and parts that can't. **Amdahl's Law** states that if a fraction p of a program can be parallelized and a complementary amount $1 - p$ can't be parallelized at all, then the maximum amount it can be sped up is $\frac{1}{1-p}$. This represents the limit in which the parallel part executes instantly, and provides an immediate rule of thumb for how much a program can possibly be sped up.

gpu-Imogen solves a (very large) IVP ODE; While multiple steps cannot be computed at once, each step involves solving a nonlinear function of millions or possibly billions of variables, and it is the evaluation of the fluid dynamic steps themselves that is parallelized.

Parallel strategies.   The underlying PDEs that Imogen solves are of the strictly hyperbolic type and therefore have a locality property (all wavespeeds are real and finite). Looking back in time, the region from which information can reach and therefore influence any given point looks like (is conformally equivalent to) a cone. This physical locality property leads to a computational locality property: Because the true solution at any point depends only on a conical region extending in to the past, the computed solution at any cell depends only on cells containing that conical region (In fact, the solution not only can but *must* depend on all cells in the past signal-cone in order to be stable), and that cone extends only to the neighbors, as depicted in figure 10.

For completeness' sake, we note that the domain of dependence of equations of different character. Parabolic equations (e.g. incompressible fluid equations) are characterized by an infinite domain of dependence, but one in which the dependence on distant parts of the solution generally decays rapidly (exponentially). Elliptic equations (e.g. electrostatics or gravitation) have imaginary-valued characteristic 'speeds' and show the behavior that the solution at every point depends upon every other point, and not necessarily weakly. This all-to-all dependence is what makes the solution of elliptic PDEs infamously difficult to parallelize.

Ghost cells. When calculations possessing a locality character are distributed, it is inevitable that at the boundary between processors i and j,

82
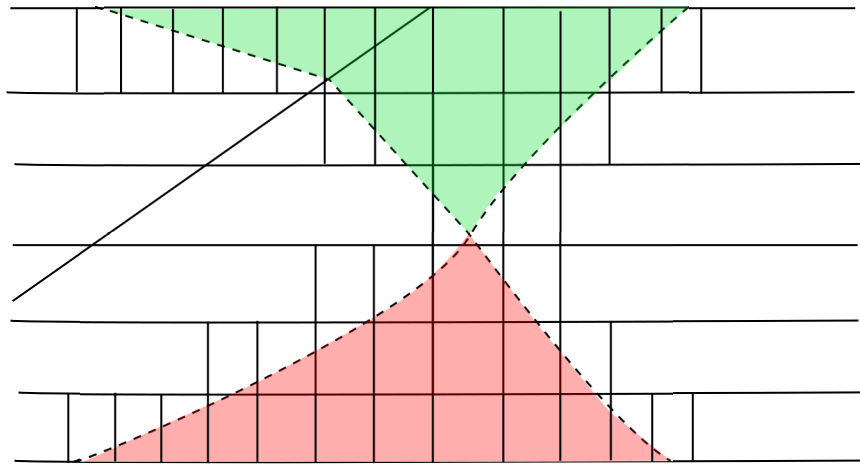
Figure 10. Schematic drawing of the domain of dependence (in red), which grows backward in time, and the domain of influence (in green) which grows forward in time. Time levels are horizontal lines, while relevant cells are vertical lines. The bounding exact signal speeds are traced by the dashed lines.
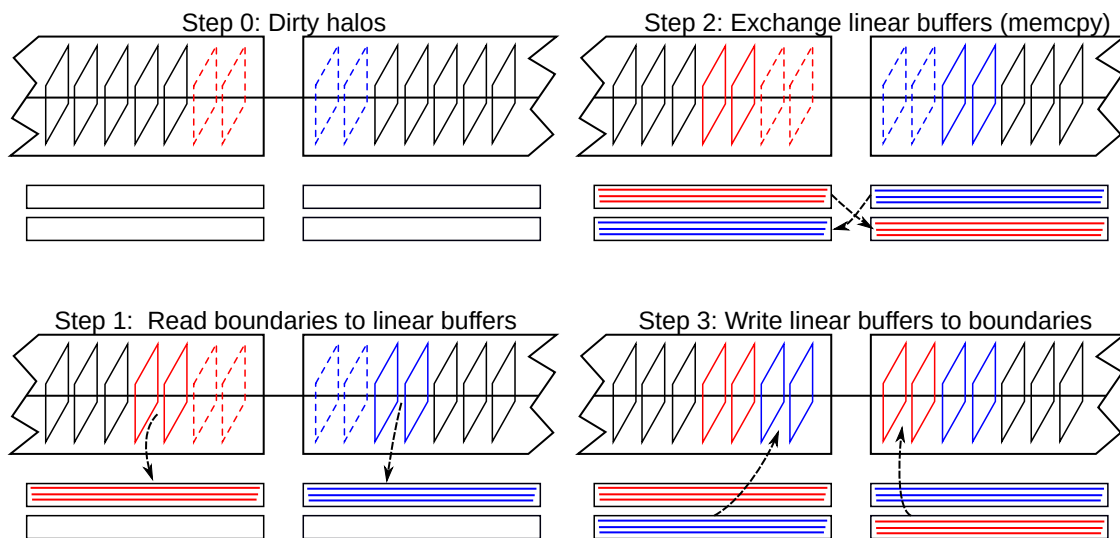
Figure 11. Depiction of the halo exchange process utilized by gpu-Imogen: First, the halo sources (solid red/blue planes) are copied to linear buffers; This process is reasonably efficient, and the GPU's memory bandwidth is very wide. Then the halo buffers are exchanged, which is very efficient but limited by the relatively low speed available. Finally, the linear tapes are efficiently copied back to planes. An analagous process applies to MPI halo exchanges; The only difference is that the buffers are exchanged by MPI messages rather than `cudaMemcpyDeviceToDevice`.

processor i needs information held by processor j and vice versa. A standard technique for resolving this conundrum is the use of *ghost cells*: The data on processor j that processor i needs for the next timestep is copied to processor i before beginning the timestep. gpu-Imogen performs parallel exchange between GPUs and between nodes entirely through the use of ghost cells, and also uses ghost cells at the level of individual multiprocessors within the GPU for computation.

A variety of strategies are applied for calculations involving differences on various directions, sometimes at once, that come up in the process of solving the evolution equations being used. Most of these have been tested using the *nSight* performance profiler and found to acheive good performance.

GPU utilization in gpu-Imogen. The performance of gpu-Imogen is tested using both simple built-in timer functions to measure the time required for a given number of timesteps to be taken (as used by the code to estimate its own likely walltime required to run), and in much greater detail using the *nSight* profiler tool from nVidia.

These tests show that once enough work is available (the simulation is large enough) that the GPU kernels no longer execute in less than the blink of an eye, the utilization of processing resources is highly efficient.

The archive of 1D simulations which were performed to generate many of this paper's results were near the overhead-dominated regime, and they revealed an overhead that accumulates to roughly 1.6 milliseconds per timestep (meaning an upper limit of about 600 iterations per second). The 3D simulations were in the exact opposite, utilizing essentially 100% of available GPU time. The crossover point depends on the capability of the GPUs being used (the more powerful the

GPUs, the more work required), as well as the amount of extended physics being computed but roughly speaking GPU utilization behaves as

$$\text{utilization} = \frac{N_{cells}}{N_{cells} + 20000} \times 100\% \qquad (4.4)$$

where N_{cells} is the number of cells per GPU.

In addition to runtime overhead per iteration, there is a small fixed overhead required for the MATLAB runtime to start and for GPU kernels to be JITed on first use, in addition to whatever time is required for computing simulation initial conditions. This is generally negligible in all realistic use scenarios, in which many iterations will be run, but it is very clear in profiling runs in which only a small number of steps will be taken. In *nSight* there are usually random (relatively) long delays for the first half dozen or so iterations before behavior settles in.

An unexpected source of overhead, it turned out, lives somewhere inside the CUDA runtime: GPU memory allocations/frees, when done on the default stream for the first device used were found to often carry an *extremely* large time penalty. And not only were they slow, the time required for cudaMalloc and cudaFree actually appears to be proportional to the size of the alloc or free. With no way to avoid this, several groups of compiled functions now support the ability to be passed pre-allocated buffers to minimize the number of allocations/frees that must be done.

When there is enough work to keep GPUs occupied, it is found that the code is very efficient at distributing itself across multiple GPUs on a single node. This is no surprise, of course, since the bandwidth connecting devices inside a single node is very large (usually on the order of 10GBps, comparable to a
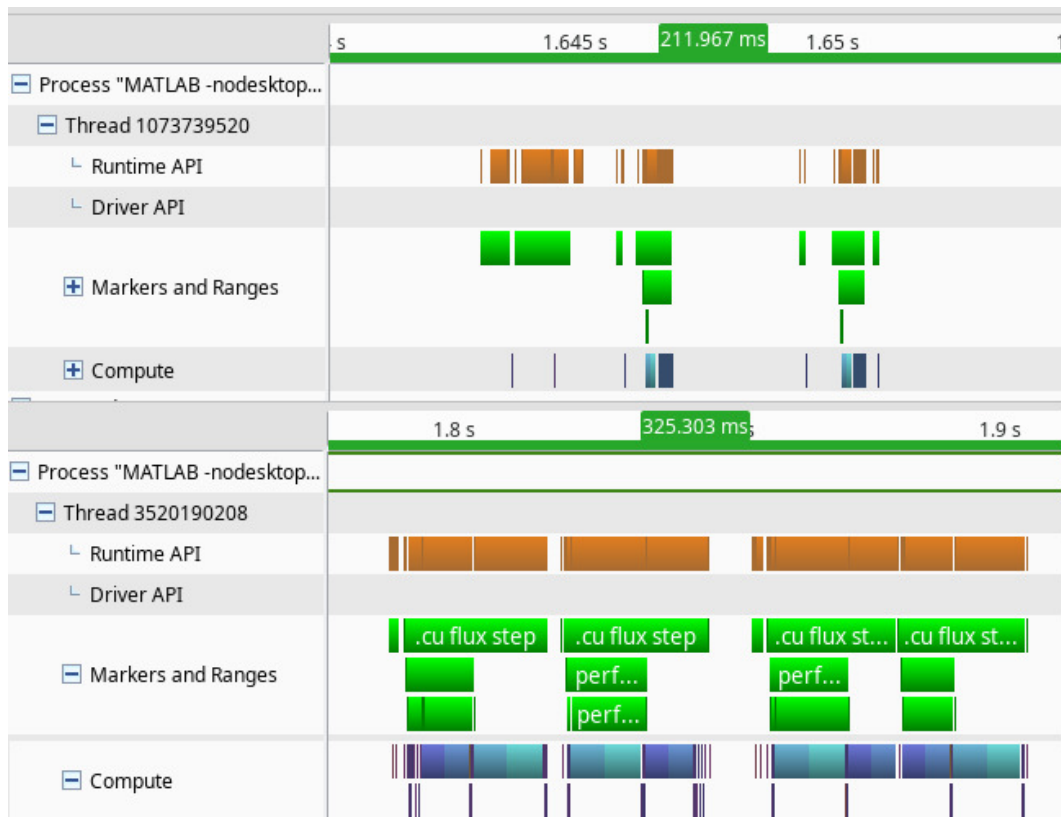
Figure 12. Crops of timelines recorded by the nSight profiler in two different cases. Above, an extremely small simulation (4096 cells in one dimension) takes less time computing than the simulation has overhead: Only about 2.3msec of GPU utilization were reported, and 55msec elapsed in computing 4 timesteps (excluding significant startup overhead on the very first timestep), for a GPU utilization efficiency of only 4%. Below, a larger simulation (1024x256) occupied about 190 of 240msec to solve 4 timesteps, using around 80% of available GPU time.

86

100Gbps network interface, though new NVLink GPU-to-host interfaces are much faster).

CHAPTER V

CODE VERIFICATION TESTS

This section describes a substantial battery of tests which have been applied to the G G code in order to verify that it correctly solves the basic equations of shock-capturing fluid dynamics and a range of additional physics.

Code test parameters. All code tests are run with the following parameters (as relevant) unless otherwise specified:

The temporal integration method is explicit trapezoid. The CFL prefactor is set to 0.85. The slope reconstructor used in the Godunov solver extrapolates primitive variables (ρ, v, P) using the Ospre limiter. The flux assignment is HLL.

Code correctness tests - 1D.

Convergence of wave propagation. In the wave propagation tests, simulations are initialized with uniform backgrounds upon which are imposed exact solutions of sonic or entropy waves. Exact nonlinear initial conditions are found by integrating the infinitesimal sonic or entropy wave eigenvector (linear) waves over an amplitude parameter. In this manner the initial condition to the situation depicted in figure (13)'s sound wave is given in terms of the normalized amplitude $a = \delta\rho/\rho_0$ as

$$\rho(a) = \rho_0(1 + a) \tag{5.1}$$

$$v(a) = M_0 c_0 + \frac{2c_0}{\gamma - 1}\left[(1 + a)^{\frac{\gamma-1}{2}} - 1\right] \tag{5.2}$$

$$P(a) = P_0(1 + a)^\gamma \tag{5.3}$$

$$c(a) = c_0(1 + a)^{\frac{\gamma-1}{2}} \tag{5.4}$$

$$x(a, t) = x_0 + c_0 t((1 + M_0) + \frac{\gamma + 1}{\gamma - 1}((1 + a)^{\frac{\gamma-1}{2}} - 1)) \tag{5.5}$$
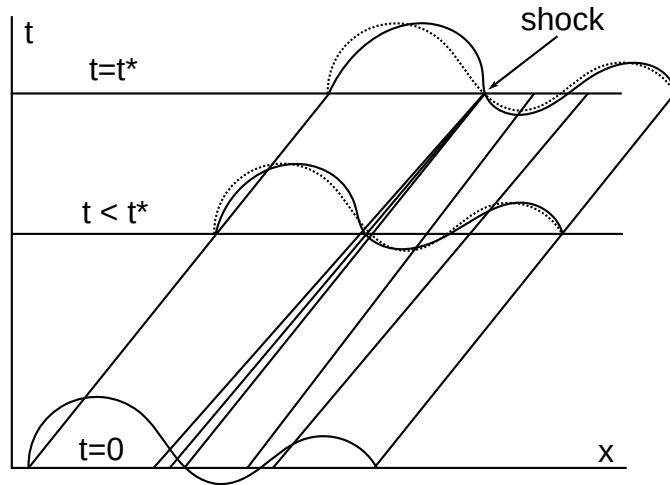
Figure 13. X-T plot depicting nonlinear propagation of a sonic disturbance leading to shock formation: Where the soundspeed is a decreasing function of position, three lines tracing the movement of characteristic packets converge towards the point of maximum negative gradient until at the time $t = t*$ given in (5.7) they collide. This marks the formation of a shock and the end of the exact solution used to track wave propagation accuracy. Two retreating lines on a region where soundspeed is increasing depict rarefaction (spreading out of characteristics).

which are the density, velocity, pressure, adiabatic sound speed and characteristic packet positions (the location where an initial sonic characteristic of amplitude a starting at x_0 at time t will be found), and M_0 is the Mach at which the uniform background is moving. The code test unit uses $\rho_0 = 1$ and $P_0 = 1$ for the background fluid state; The choice is arbitrary because there is nothing else to normalize against.

The exact initial condition for the sound wave is essential to test the code, as a linear sound wave initial condition will generate an error proportional to amplitude squared that does not decrease when the grid is refined.

The exact solution to an entropy wave is simply an arbitrary perturbation to density.

In the test, the simulation runs on a unit line, square or cube in dimension 1, 2 or 3 respectively. The wavenumber k is quantized by the imposition of periodic boundary conditions, such that wavennumbers $k_i = 2\pi n_i$ are chosen for integer inputs n_i. There is a choice in labelling as there are two sonic eigenvalues (k and $-k$) per ω but two sign choices for ω as well, but $\omega/k = (-\omega)/(-k)$. We choose positive ω. By utilizing symmetric flux limiters, which have the property that $F(\rho, v, P) = -F(\rho, -v, P)$, we can guarantee preservation of parity symmetry about a coordinate axis. By extension, this means only one half/quadrant/octant of n_i need to be tested.

Analytically there is no limit on n. On the finite simulation grid a cutoff is imposed on n by, at the very least, the Nyquist sampling theorem - $n_i < \frac{1}{2} n_{\text{grid},i}$. The actual range of wavenumbers that a code can resolve is called its spectral bandwidth and, for grid based codes, this is necessarily substantially less than the Nyquist limit (only spectral element codes come anywhere close to the Nyquist limit). Sine waves in GPU-Imogen resolved by less than about 20 cells per wavelength experience substantial damping: ($Im(\omega) \approx 0.1 Re(\omega)$), implying a damping period of a few oscillation periods.

Galilean invariance is tested by running with a static background ($M_0 = 0$) and with a moving one ($M_0 = .526172$, a completely arbitrary value) and finding that the results are identical up to the 2nd order truncation error. The truncation error is not Galilean invariant because it is tied the grid and thus the frame in which the flux differences are evaluated.

Under the Euler equations, with an ideal gas equation of state, the group velocity is constant. By using the Euler equations we have already assumed that the second derivative terms (mass diffusion, kinematic viscosity, thermal

diffusivity) should be neglected. Thus we expect a wave packet of infinitesimal amplitude to be everlasting, experiencing no dissipation, dispersion or distortion, so that

$$\vec{u}(x,t) = \vec{U}_0 + \epsilon \left[1, \pm c_s/\rho, c_s^2\right] f(x \pm ct) \tag{5.6}$$

is a solution for any finite, smooth f for at least some length of time.

With waves of *finite* amplitude, adiabatic compression modulates the local soundspeed so that the peaks and troughs see higher and lower local sound speeds, and pull ahead or fall behind the midpoint of the wave (where $\delta\rho$ crosses zero and the characteristic amplitude is infinitesimal). This is a form of self-interacting nonlinearity known as wave steepening. It is also observed in gravity-driven surface waves in shallow water (including tsunami), and in nonlinear optics where it is known as self phase modulation.

In all its forms, the underlying nonlinear mechanism is that the local wave amplitude modulates its own local phase velocity. In acoustics, unless the fluid equation of state exhibits exotic behavior, the coefficient of modulation is always positive for all perturbative waves - there is no amplitude at which further compression of an ideal gas causes soundspeed to begin dropping, for example. This is not the case in e.g. nonlinear optics, in which the group velocity dispersion coefficient may have either sign; Positive values leading to soliton formation (an optical analogue of a shock) and negative ones leading to pulse stretching.

The point is, the finite amplitude sound wave represents an exact *nonlinear* solution to the Euler equations which isn't based on a symmetry or balance.

In the one-dimensional wave tests, waves are initialized using a sinusoidal density with wavenumbers of 1 and a relative amplitude 1%. This is tame as far as perturbations go, but in air would be equal to a literally deafening sound pressure

level of 154dB (0dB in air is referred to a 20μPa pressure fluctuation, which is roughly the quietest sound a young person can hear at 1KHz in an anechoic chamber. The largest amplitude possible for an undistorted sine wave in air is 194dB before the trough reaches zero density).

The simulation is evolved forward in time for 0.95 times the critical time t^*,

$$t* = \frac{2}{c_s(\gamma + 1)} \max(-da/dx)^{-1} \text{(wave periods)} \tag{5.7}$$

$$t* = \frac{4\pi}{c_s^2|k|(\gamma + 1)} \max(-da/dx)^{-1} \text{(time)} \tag{5.8}$$

The value t^* is the time at which characteristic lines near the largest negative amplitude slope will cross, at which time the flux becomes multivalued and a discontinuity (shock wave) forms. This is the endpoint for the solution prescribed in (5.1)- (5.5).
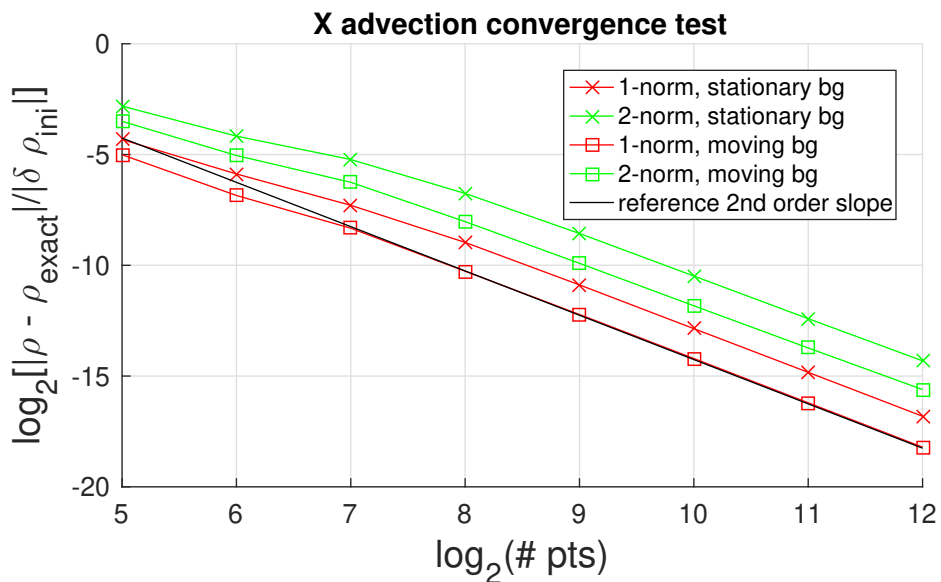
Figure 14. Convergence towards exact solution of a sonic characteristic. Initial condition: $x \in [0, 1]$, $\rho_0 = P_0 = 1$, $\gamma = 5/3$, $M_0 = 0$ or $M_0 = .526172$ (an arbitrarily chosen value), exact sound wave with $a(x, 0) = a_0 cos(k \cdot x)$, $a_0 = .01$ and $k = 2\pi$. Norms measured at $t = 0.95t^* \approx 6.803874$. The solution is Galilean invariant up to truncation error.
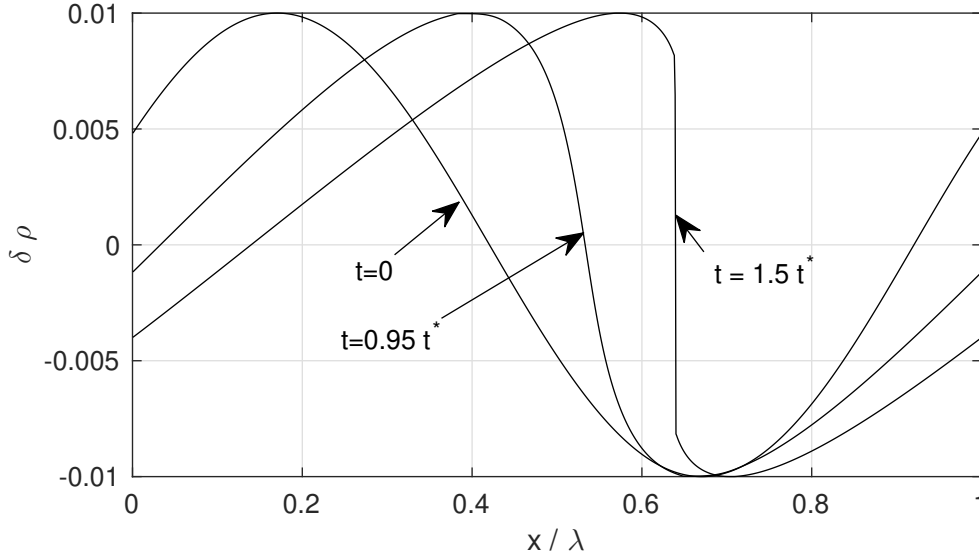
Figure 15. A reference sound wave of amplitude .01 shown in its initial state, immediately before the critical time at which it forms a shock, and shortly after forming a shock; Numeric simulation with 512 grid points. The wave has been horizontally shifted for presentation. The evolved waves required approximately 10000 and 15000 time steps respectively.

The flow, of course, still exists, but now characteristic transformation (between forward sonic, entropy, and reverse sonic) occurs at the shock, as well as a scattering by these different characteristics off each other and dissipation by the shock that alters the 'equilibrium' state. Which is to say, any attempt to continue the exact solution grows extremely complicated very quickly.

Dustybox test (drag solver). The DustyBox tests the time accuracy of the drag solving algorithm independent of space. Spatially uniform gas and dust with specified parameters are placed into a box and given a relative velocity, and the simulation is let evolve and they decay.

Assuming the form of the drag law is exactly integrable, the exact relative velocity is available for comparison. This is not the case for the general law given by Eq. 2.61 outside of its asymptotic limits. Instead,
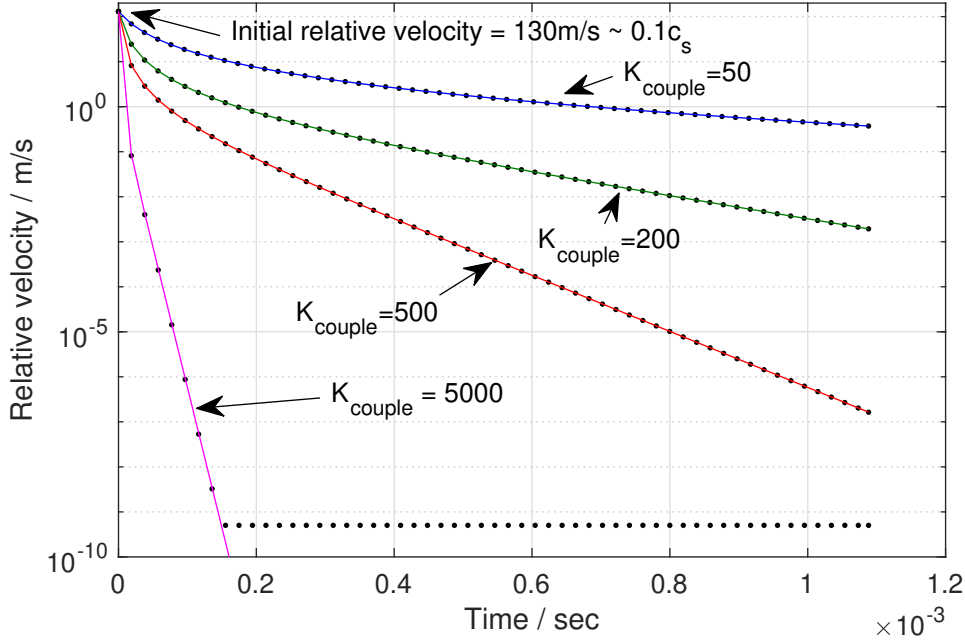
Figure 16. Demonstrating the efficacy of the LogTrap solver algorithm in a box of length 1 meter. Dust particles with $\sigma = 7 \times 10^{-6}m^2$ are initially in motion at 130m/s in hydrogen at STP. With $K_{couple} = \frac{d\log v}{dt}/(c_s \times 1m)$ defined as the test particle stopping time over the sound crossing time set to 50, 200, 500, and 5000 by respectively setting particle masses to 188, 47.3, 18.9 and 1.89 nanograms, accuracy remains dead on. In the $K_{couple} = 5000$ case, the relative velocity decays by 99.93% (and *Re* decreases from 3610 to 2.4) *in the very first timestep*, yet the relative error just before velocity decays below resolvability is still only 6%. In the other cases, the error at the endpoints is 0.36%, 0.05% and 0.002% for decreasing K_{couple}.

reference results are generated using Matlab's `ode113` function with the options

`odeset('Reltol',1e-13,'AbsTol',1e-14)` .

In the test, fluid 1 is given the microscopic parameters of molecular hydrogen, a density of .0824 and a pressure of 101325 (hydrogen at STP). "Fluid" 2 is given a cross section of $7 \times 10 - 6m^2$, corresponding to a sphere of diameter approximately 3mm.

94

Accuracy of dustybox solutions
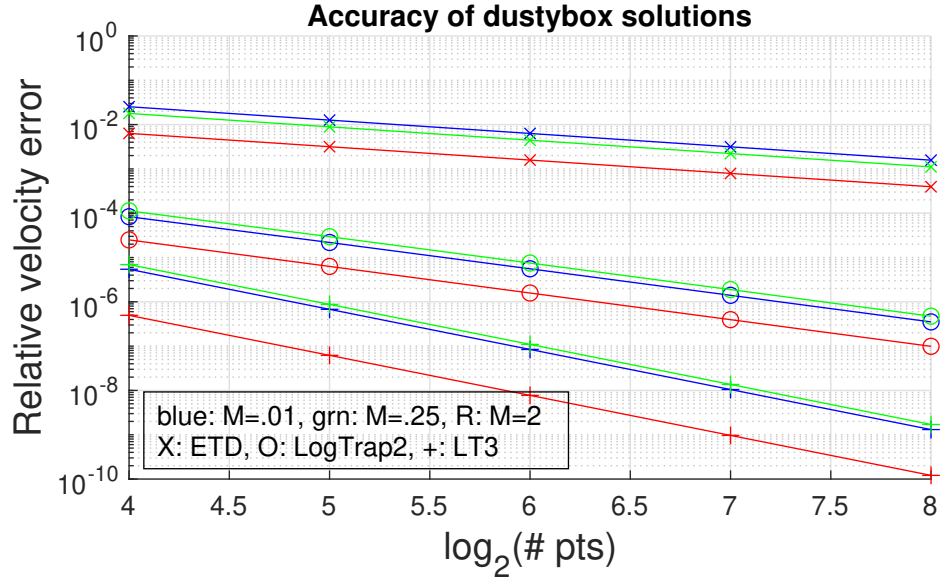
Figure 17. Plots showing the 1st through 3rd order accuracy of the ETD, LogTrap2 and LogTrap3 solvers. The fluid conditions are the same as in figure 16, with K_{couple} set to 10. The dust velocity is initially 0.1 times soundspeed, and the gas speed is (per the legend) .01, .25 and 2 times soundspeed (referring here to the unmodified c_s). The simulation is run for 10 milliseconds and the resulting relative velocity is compared to the result from solving the drag ODE using Matlab's ode113 solver with the tolerance set to 10^{-13}; Both the error prefactor and the rate of convergence of the LogTrap algorithms are superb.

This cross section was chosen so that the initial relative velocity of $0.1c_s \approx 130m/s$ yields $Re \approx 3610$, well into the turbulent regime. From here, particle mass is chosen in order to set the coupling time (without comment as to the physicality of the implied densities).

Four numeric solvers have been implemented: Classic explicit midpoint (EMP) and 4th order Runge-Kutta (RK4), the exponential Euler method (EE), and an exponential-like method dubbed the LogTrap method.

The explicit methods are used only to check that the drag-calculation core function is correctly implemented because they are only conditionally stable and would require additional work to test for timestep restrictions in practice.

Dustywave test. In the dustywave test, the ability of the code to correctly propagate a sound eigenstate of a coupled gas-dust system is tested for several coupling strengths (weak, intermediate, strong), which correspond to a test particle stopping time respectively much longer than, comparable to, and much less than the sound wave oscillation period.

Because coupled gas-dust flows require computing the microscopic viscosity, and this microscopic value in turn takes physical values as inputs, this test is run in SI units rather than normalized units. The calculation domain is a box one meter long with circular boundary conditions.

The 0th order initial conditions for the gas are a density of .0824, velocity of 0 and pressure of 101325 (SI units for molecular hydrogen at RTP). The thermodynamic model is warm molecular hydrogen with $\gamma = 7/5$; The details are available in gpuImogen via `fluidDetailModel('warm_molecular_hydrogen')`. They are, a dynamic viscosity of 8.9135×10^{-6}kg/m-s at 298.15K, scaling as $(T/298.15)^{0.7}$, and a kinetic cross section of 1.9272×10^{-19}m² scaling as $(T/298.15)^{0.2}$.

The 0th order initial condition for the dust is a density of 1, at rest. The dust particles are given a radius of 5 micrometers. In order to satiate the numeric solvers, an adiabatic index of 1.01 is asserted. The particles are treated as hard spheres.

The relative coupling strength depends on the particle drag time versus wave frequency, which in turn is proportional to wavenumber. For a given target coupling strength as input, the particle mass is sought which generates it:

$$S_{target} = \hat{K}_d(m_d)/\omega(\hat{K}_d(m_d)) \tag{5.9}$$

where ω is a sound wave eigenvalue of the dusty gas linear matrix (2.81). Given that the relative coupling strength is monotonically related to the particle mass, if an interval on which the solution to this nonzero root-finding problem is guaranteed to lie can be given to a root finder algorithm (such as Matlab's `fzero()`) then convergence is assured. Starting from an arbitrary m_0, Imogen first computes m_{low} by scaling m_0 down by factors of 4 until the coupling strength is too large, then scales up by 4 until it is too small to find m_{high}. The solution to (5.9) is now guaranteed to lie on the interval (m_{low}, m_{high}).

It is noted that while any mass and particle size/volume may be asserted numerically, physically realizable values are bounded by the density of solid matter not subject to external compression, the pressures required to substantially raise the density of solid matter not generally occurring outside of stellar and planetary cores, detonating atomic bombs or diamond anvils.

Once m_d is found, a sine wave perturbation of amplitude 0.001 and wavelength equal to the length of the box is evolved to $t = k/\mathcal{R}\rceil [\omega]$, i.e. one trip through the box, and the metric error is computed in the p-norm as

$$E^p = \int_0^1 [(\rho_g(x) - \rho_{g,ref}(x))^p + R(\rho_d(x) - \rho_{d,ref}(x))^p]^{1/p} \, dx \qquad (5.10)$$

with $R = \rho_d/\rho_g$ is the ratio of equilibrium densities. The inclusion of the dust density, as can be seen in figure 18, is associated with initially slow convergence because of the tendency of the dust to evolve entropic mode errors - stationary glitches in density - which have a strong tendency to persist over time, until finally 2nd order convergence is obtained asymptotically.

Convergence of Sod shock tube. The Sod shock tube is a classic test for shock-capturing codes in which the decomposition of a one-dimensional
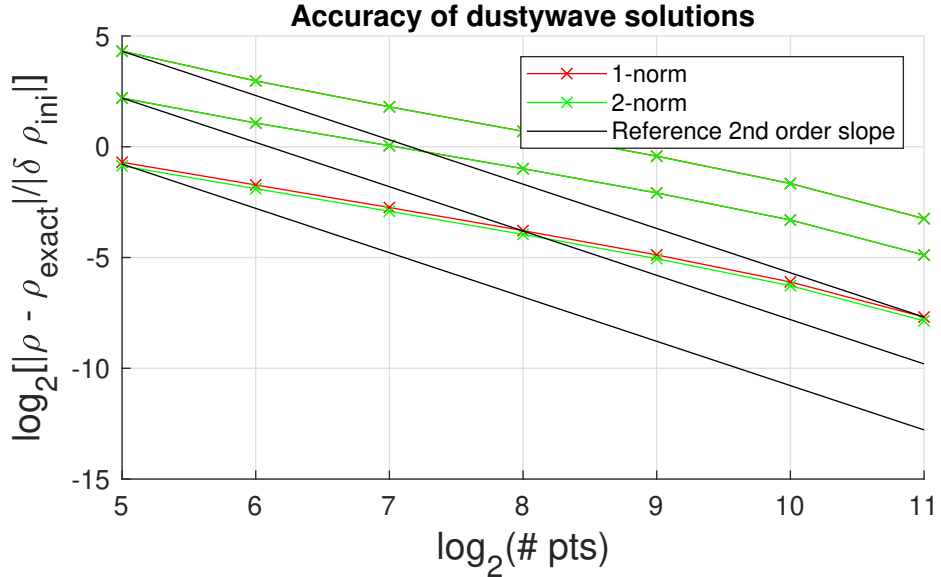
Figure 18. Convergence of the Dusty Wave test with overlaid 2nd order slope lines. The initially 1st order convergence is due to the tendency of the dust to evolve persistent entropy-mode glitches.

Riemann problem (RP) is evolved forward until shortly before the emitted waves reach the boundary.

The RP tested here is the same as that specified by Sod (1978) and is specified by left and right states of

$$u_{left} = [\rho = 1.0, v = 0, P = 1.0]$$

$$u_{right} = [\rho = 0.125, v = 0, P = 0.1]$$

with the gas equation of state defined by $\gamma = 7/5$.

The simulation is a unit line segment on the interval $[-0.5, 0.5]$, with $u(x < 0) = u_{left}$ and $u(x \geq 0) = u_{right}$ and constant BCs. The exact solution to the decomposition of this particular RP is given in terms of the self-similarity

98

parameter $s = x/t$, in all cases for $t > 0$, as

$$\psi(s < -c_{left}) = u_{left} \tag{5.11}$$

$$\psi(-c_{left} < s < c_{tail}) = u_{fan}(s) \tag{5.12}$$

$$\psi(c_{tail} < s < c_{contact}) = u_b \tag{5.13}$$

$$\psi(c_{contact} < s < c_{shock}) = u_{postshock} \tag{5.14}$$

$$\psi(s > c_{shock}) = u_{right} \tag{5.15}$$

This describes a decomposition that emits a left-going rarefaction fan, two regions of constant state separated by a contact discontinuity, and a rightgoing shock wave. The first step is to solve a transcendental equation that equates the pressure after the shock jump with the pressure at the tail of the rarefaction,

$$G = (\gamma - 1)/(\gamma + 1) \tag{5.16}$$

$$\beta = \frac{\gamma - 1}{2\gamma} \tag{5.17}$$

$$(P_l^\beta - P^\beta)\sqrt{\frac{(1 - G^2)P_r^{1/\gamma}}{G^2 \rho_l}} = (P - P_r)\sqrt{\frac{1 - G}{\rho_r(p + Gp_r)}} \tag{5.18}$$

with left pressure P_l, left density ρ_l, right pressure P_r and right density ρ_r as inputs and the postshock pressure P to be solved for. From this the Rankine-Hugoniot relations yield the remainder of the postshock state, $u_{postshock} = RP(u_{right})$. By integrating the sonic amplitude parameter for Eqs. (5.1 - 5.5), the state $u_{fan}(x, t) = u_{fan}(s)$ is found, as is the speed c_{tail} and the position of the tail. Then $u_b = u_{fan}(c_{tail})$ and the entire solution is written.

This process is implemented in the function `SodShockSolution(xcoords, t)`. The function is careful about cells which straddle boundaries between the piecewise states and computes integral averages in them in order to be correct (as the numeric code, it must be remembered, represents cells as volume averages).
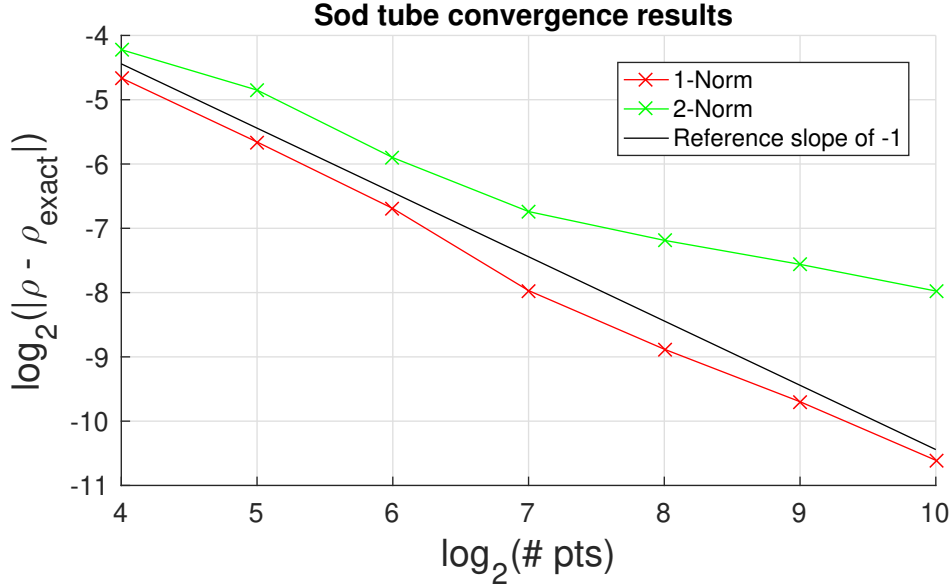
Figure 19. Convergence of numeric solution of a Sod shock tube. 2-norm convergence slows to $1/\sqrt{(N)}$ as the diffusion of the contact eventually dominates the error.

The error metrics are generated by comparing the L_1 and L_2 differences in density. As expected, the solution only converges at 1st order because of the $O(h)$ uncertainty in the exact shock position on the grid and because the slope limiter goes to first order there, leading to large errors in the vicinity of the shock. However, these errors are monotonically bounded and decay exponentially moving away from either side of the shock.

Convergence of Einfeldt rarefaction tube. The Einfeldt rarefaction tube is another classic test for codes in which a Riemann problem is specified that produces a double rarefaction between two mutually retreating slabs of fluid.

It appears in Einfeldt (1988) as a demonstration of the potential for schemes to produce glitches at sonic points, or create entropy-violating shocks. The HLL and HLLC fluxes used by GPU-Imogen are essentially glitch-free as expected.

The Einfeldt initial condition may be specified on the unit line segment $x \in [-0.5, 0.5]$ as a Riemann problem with initial states parameterized by the initial Mach number m as

$$u_{x<0} = \rho = 1, v = -mc_s, P = \rho c^2/\gamma$$

$$u_{x>0} = \rho = 1, v = mc_s, P = \rho c^2/\gamma$$

and the fluid adiabatic index given by γ.

The exact solution to the Einfelt tube may be found by a self-similarity transform. Let the initial condition be specified by

All non-trivial structure emanates from the origin at $x = 0$; The head of the rarefaction travels at the the infinitesimal speed of sound plus the background convection speed, $x_{head}(t) = (m+1)c_s t$ at which point the fluid is travelling at a speed of mc_s. Therefore we have that

$$v(x, t) = mc_s \frac{x}{(m+1)c_s t} = \frac{m}{m+1} s \tag{5.19}$$

Given this prescription for the velocity field, we assume a self-similarity solution of the form

$$\rho(x, t) = \phi(x/t) \equiv \phi(s) \tag{5.20}$$

with self-similarity variable $s = x/t$. Then the continuity equation may be massaged into an integrable ODE,

$$\partial_t \rho + \partial_x \rho v = 0 \tag{5.21}$$

$$\frac{d\phi}{ds} \partial_t s + \frac{m}{m+1} s \frac{d\phi}{ds} \partial_x s + \phi \frac{m}{m+1} \partial_x s = 0 \tag{5.22}$$

$$-s \frac{d\phi}{ds} + \frac{m}{m+1} s \frac{d\phi}{ds} + \phi \frac{m}{m+1} = 0 \tag{5.23}$$

$$d\phi/ds = m\phi/s \tag{5.24}$$

after noting that $\partial_x s = 1/t$ and $\partial_t s = -x/t^2$. This ODE has the solution

$$\log(\phi/\phi_0) = m \log(\frac{s}{(m+1)c_s}) \tag{5.25}$$

$$\rho(x,t) = \phi(x/t) = \rho_0 \times \left(\frac{x}{(m+1)c_s t}\right)^m \tag{5.26}$$

The rarefaction fan is an expansion wave and its behavior changes fundamentally depending on the initial Mach of the retreating slabs. From Eq. (5.2), letting $a \to -1^+$, the largest initial speed from which an expansion wave that decompresses to zero density can reach zero speed is

$$M_{crit} = \frac{2}{\gamma - 1} \tag{5.27}$$

Notably, the critical Mach increases without limit as the equation of state approaches isothermal. If $m < M_{crit}$ then the expansion fan will be able to slow the retreating fluid down to zero speed and the solution of the problem will have five piecewise regions: The unaffected slabs at large $|s|$, bracketing two rarefaction fans, bracketing a stationary central region. In this case of a subcritical Mach, the solution is well behaved everywhere and can be numerically represented everywhere.

However for $m > M_{crit}$ the central quiescent region vanishes and there are only three piecewise regions, the unaffected slabs bracketing a single expansion described by Eq. (5.26). The problem which occurs in this solution when s is allowed to run through zero is obvious - it goes to vacuum. Such a situation is numerically impermissible because of the resulting divide by zero, which can be seen as representing the fact that it breaks one of the fundamental assumptions of continuum mechanics.

The formal convergence of such supercritical rarefactions is prevented because GPU-Imogen, like all gridded codes, necessarily asserts a very small

minimum density to prevent division by 0. The convergence grows worse with increasing m because density is suppressed as s^m which quickly becomes exceedingly small for most values of s as m grows.

Convergence of Woodward & Colella double blast tube. The double-blast tube was presented by Colella and Woodward (1984) in their 1984 paper introducing the piecewise parabolic method (PPM) interface reconstruction scheme.

It consists of a line segment of unit length on the interval $[0, 1]$ containing three piecewise discontinuous initial states,

$$u_{x<0.1} = \{\rho = 1, v = 0, P = 100\}$$

$$u_{0.1 \leq x \leq 0.9} = \{\rho = 1, v = 0, P = .01\}$$

$$u_{x>0.9} = \{\rho = 1, v = 0, P = 1000\}$$

with the boundary conditions on either end set to extrapolate-as-constant and the gas equation of state defined by $\gamma = 7/5$.

The decomposition the two RPs launches extremely strong shocks towards the middle. These collide, yielding very fine details which require considerable grid refinement to resolve for lower-order schemes and which displayed the high resolution of PPM to advantage. The simulation is stopped arbitrarily at $t = 0.038$.

There is no analytic solution except for short times; Imogen accepts the most-refined solution as "exact." Because the grids are refined by doubling resolution, the process of integral-averaging the fine grid over the coarser ones simplifies to the following: For each decrease in refinement by one step, average fine cells 2N and 2N+1 into cell N.
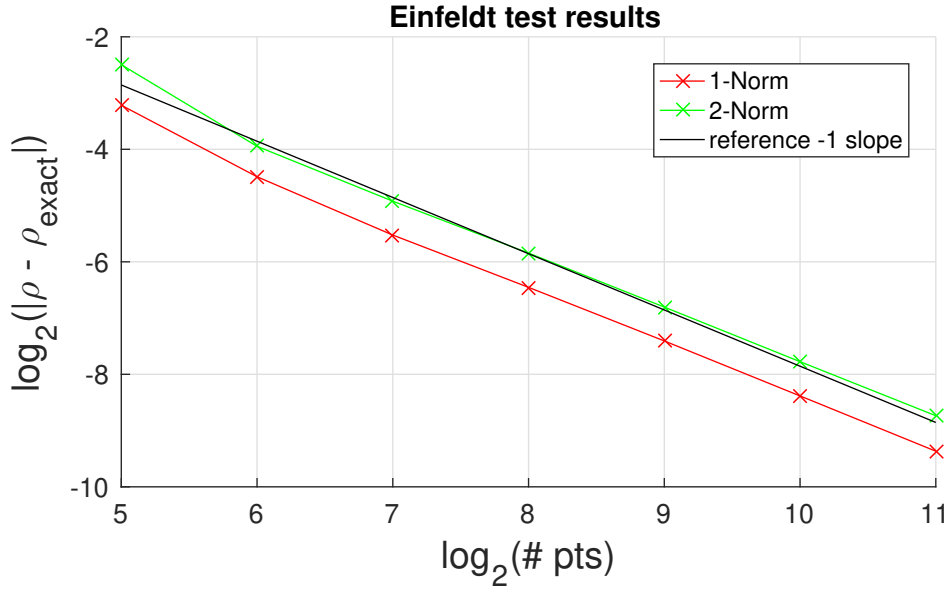
Figure 20. Convergence of numeric solution of an Einfeldt rarefaction with $\gamma = 1.4$ and $m = 4$ (barely subcritical).
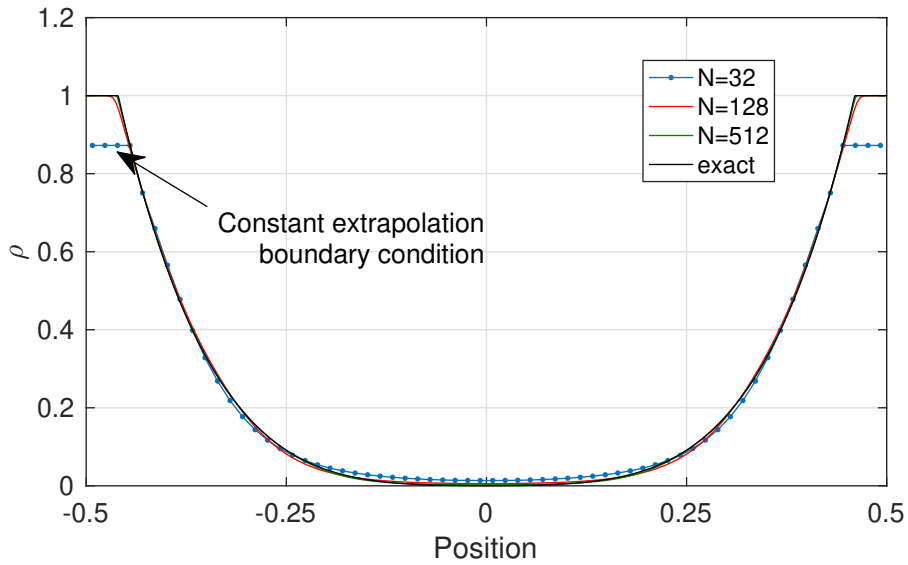
Figure 21. Plot of numeric results for above Einfeldt tubes at resolutions of 32, 128 and 512 cells, with exact solution in black: The solution is captured, and no sonic kink is evident.
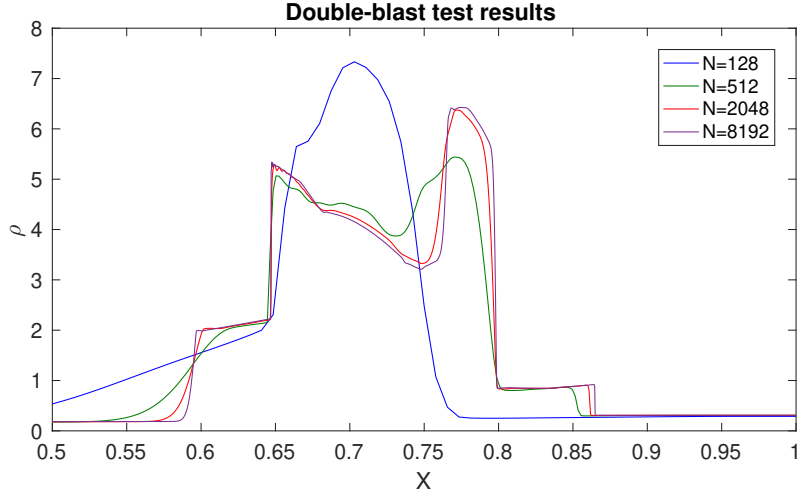
Figure 22. Results from GPU-Imogen for the Woodward-Colella double blast tube for successive quadruplings of resolution

Initially convergence is poor due to the influence of unresolved structure, however once all major forms become resolved the expected 1st order convergence of a shock-containing solution emerges.

Convergence of Noh implosion tube. The Noh implosion tube is another specific Riemann problem with a slight twist. The implosion consists of a shock propagating into a cold fluid (nominally with $M = \infty$, i.e. into cold fluid temperature of zero) which then collides with a perfect wall, leaving stationary doubly-shocked fluid behind a shock which is now propagating back the way it originally came.

The GPU-Imogen version is a little more flexible. The problem can be run in any of planar, cylindrical or spherical geometry. The planar problem is solved exactly for arbitrary Mach.

The initial condition is specified as a box on the line segment $x \in [-1, 1]$. The parameters are the initial radius of the shock r_0 from $x = 0$, arbitrary initial
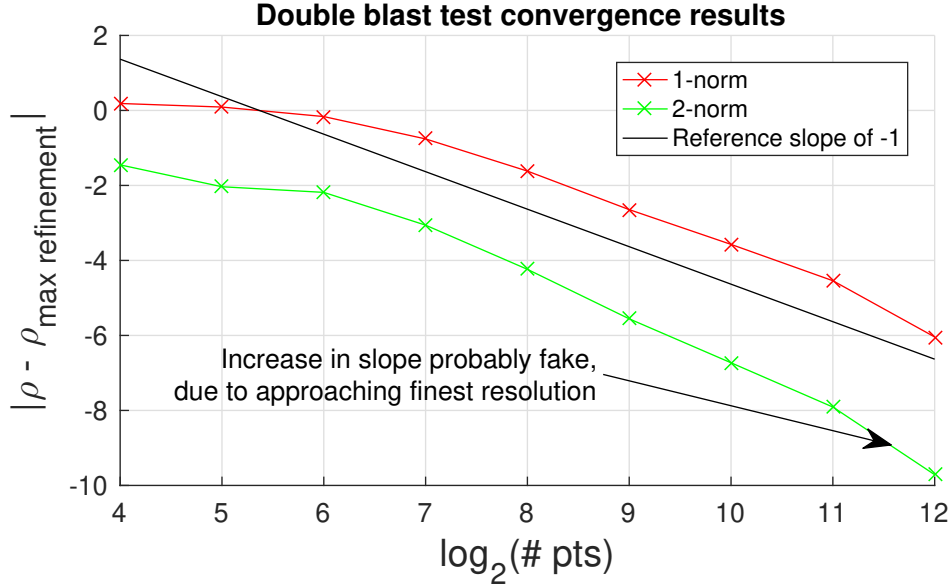
Figure 23. Convergence of a double blast tube. A resolution of twice the largest shown is taken as being exact.

$\rho_0, P_0 > 0$, and the Mach m that sets the strength of the shock (by which v_0 is determined).

The code uses $|r_0|$ as the distance of the shock from $x = 0$ or $r = 0$ and the sign to indicate either that the first shock has not hit the center ($r_0 < 0$) and $r_0 > 0$ to indicate it has.

By default, to also test mirror boundary conditions, the planar test is set to only use the halfspace $x \in [0, 1]$, with a mirror boundary condition on the negative X edge.

In planar geometry, the exact solution of the tube for arbitrary Mach numbers is possible because the only characteristics flying around are shocks separating constant states (details in Gehmeyr, Cheng, and Mihalas (1997)). Such solution is probably not possible for the case of spherical or cylindrical implosion chambers.

Noh tube convergence results
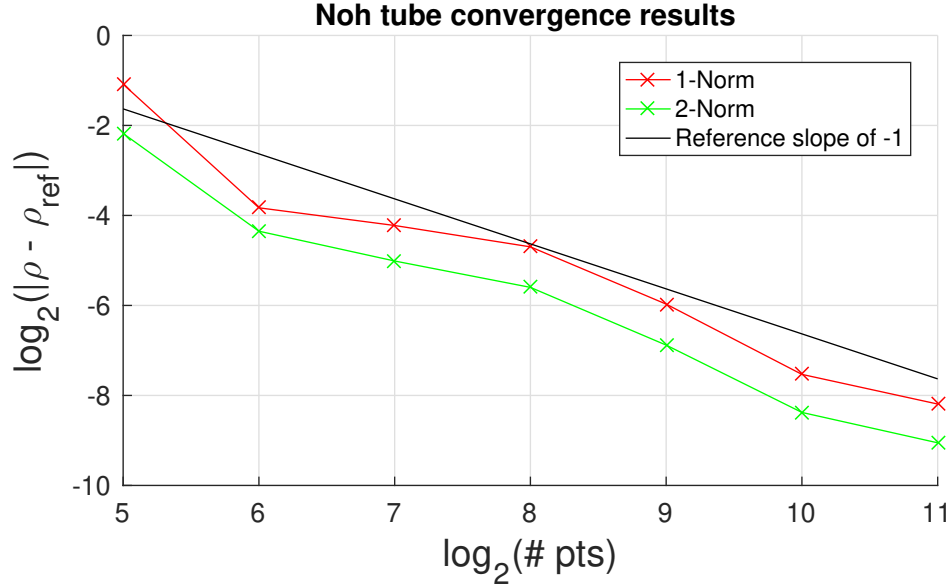
Figure 24. Graph of the depiction of the Noh tube test, showing the expected 1st order convergence for a solution containing shocks.

The initial (coldest) fluid is denoted $\psi_0 = \rho_0, -v_0, P_0$. The shock propagates in at a rate

$$v_{sh,0} = -mc_{s,0} \tag{5.28}$$

where the adiabatic index is by default 5/3, leaving behind fluid in state $\psi_1 = RH(\psi_0, m)$. At a time

$$t_1 = -r_0/v_{sh,0} \tag{5.29}$$

the shock hits its counterpropagating counterpart (or the wall), creating a twice-shocked region denoted as ψ_2. In the generalized constant-velocity-piston case an infinite sequence of ψ states are created as the shock bounces back and forth between the wall and the piston, which is fully described in Gehmeyr et al. (1997). In the GPU-Imogen test only the first two are considered.

For completeness, the first three states (with intermediate variables $\phi = \frac{\gamma-1+2m^{-2}}{\gamma+1}$ and $c_0 = \sqrt{\gamma P_0/\rho_0}$ are,

$$\psi_0 = \left\{ \begin{array}{l} \rho = \rho_0 \\ v_0 = 0 \\ P = P_0 \end{array} \right\} \quad (5.30)$$

$$\psi_1 = \left\{ \begin{array}{l} \rho = \rho_0/\phi \\ v = -mc_0(\phi - 1) \\ P = P_0(\gamma(2m^2 - 1) + 1)/(\gamma + 1) \end{array} \right\} \quad (5.31)$$

$$\psi_2 = \left\{ \begin{array}{l} \rho = \rho_1(4 + m^2(\gamma + 1) - m\sqrt{16 + m^2(\gamma + 1)^2})/(2 + 2m^2(\gamma - 1)) \\ v = 0 \\ P = P_1 + \rho_1 m_0 c_1^2(m_0(\gamma + 1) - \sqrt{16 + m^2(\gamma + 1)^2})/4 \end{array} \right\} \quad (5.32)$$

Shu-Osher tube. The Shu-Osher tube was introduced by Shu & Osher in Shu and Osher (1989) as a demonstration of their new ENO reconstruction algorithm.

Their state consists of a shock propagating at Mach 3 at the instant it runs into a plane entropy wave of amplitude 0.25 whose wavevector is parallel to the shock. Linear perturbation analysis of the shock yields the outbound wave amplitudes propagating into the postshock region given the incoming entropy wave amplitude from upstream. Wavevectors are connected by the requirement that all waves have the same oscillation frequency in the shock frame. The outcome and exact initial conditions for simulation are given in figure 25. The linear result (red line in 25) derived by the Mathematica CAS for arbitrary initial conditions is given below.

In this calculation subscript 1 denotes preshock and subscript 2 denotes postshock equilibrium quantities, with the postshock quantities defined by the

Shu/Osher Shock Interaction Tube

Steepened
a ~ 0.2 sound wave

Compressed entropy wave

Preshock entropy wave
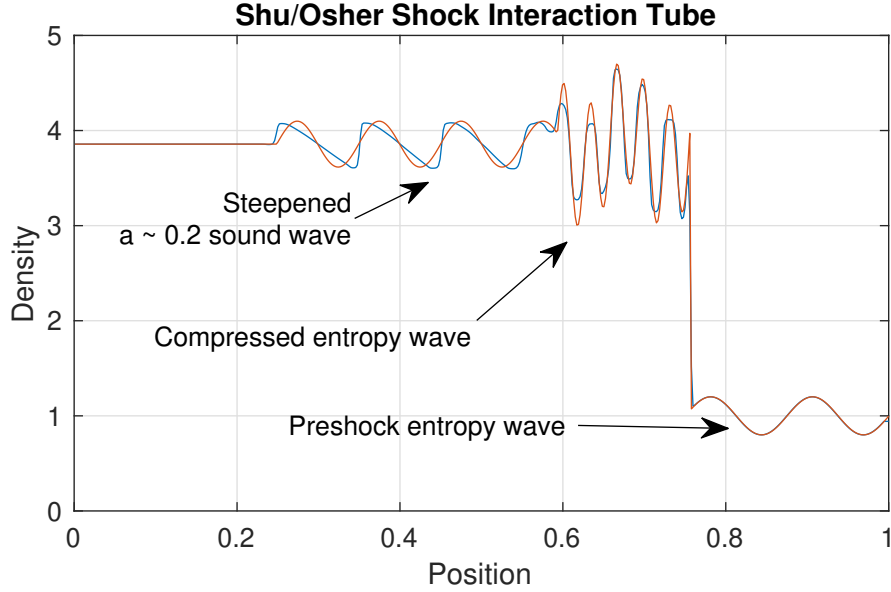
Figure 25. The result of evolving a Shu-Osher tube to $t = 0.178$ (blue curve) with linear analysis (orange) overlaid. The initial condition is set on the interval $x = [0, 1]$. The initial condition for $x > 0.75$ is $u_r = \{\rho = 1 + .2\sin(8\pi x), v = 0, P = 1\}$ with an adiabatic index $\gamma = 7/5$. The IC for $x < 0.75$ is $u_l = RH(u_r|_{x=0.25}, M_0 = 3)$, i.e. the uniform postshock solution of a shock not encountering any entropy wave ($u_l = \{\rho \approx 3.857, v \approx 2.629, P = 10.\bar{3}\}$). Boundary conditions are constant.

exact solution of the Rankine-Hugoniot conditions (given the preshock state and the Mach). This calculation was done in the stationary shock frame with the normal into the shock (so that $v_1 = Mc_1 > 0$ and $v_2 > 0$ also). For space's sake we here use the abbreviations $\beta = \gamma - 1$ and $\delta = \gamma + 1$.

$$A_{\text{snd,post}} = \frac{\epsilon}{c_2} \frac{2v_1^2(\gamma(P_1 - P_2) + \beta\rho_1 v_1(v_1 - v_2))(v_1 - v_2)}{\left(\begin{array}{c} c_2 v_1(2\gamma(P_1 - P_2) + \rho_1(v_1 - v_2)(3\beta v_1 - \delta v_2)) + \\ v_2(2\gamma P_1 v_1 + 2\gamma P_2(v_2 - 2v_1) + \beta\rho_1 v_1(3v_1^2 - 4v_1 v_2 + v_2^2)) \end{array} \right)} \tag{5.33}$$

$$A_{\text{ent, post}} = \frac{\epsilon v_1^2}{c_2 v_2^2} \frac{\left(\begin{array}{c} -2(\gamma(P_1 - P_2) + \beta\rho_1 v_1(v_1 - v_2))(v_1 - v_2)v_2^2 + c_2^2(2\gamma v_2(P_1 - P_2) \\ +\rho_1 v_1(v_1 - v_2)(\beta v_1 + (\gamma - 3)v_2)) - c_2 v_2(2\gamma P_1(v_1 - 2v_2) \\ +2\gamma P_2 v_2 + \beta\rho_1 v_1(v_1^2 - 4v_1 v_2 + 3v_2^2)) \end{array} \right)}{\left(\begin{array}{c} c_2 v_1(2\gamma(P_1 - P_2) + \rho_1(v_1 - v_2)(3\beta v_1 - \delta v_2))+ \\ v_2(2\gamma P_1 v_1 + 2\gamma P_2(v_2 - 2v_1) + \beta\rho_1 v_1(3v_1^2 - 4v_1 v_2 + v_2^2)) \end{array} \right)}$$

(5.34)

$$x_{\text{shock}} = \frac{i\epsilon}{\rho_1 \omega} \frac{v_1(v_1 - v_2)(-2\gamma P_2 v_2 + \rho_1 v_1(\beta(v_1 - v_2)v_2 + c_2(\beta v_1 - \delta v_2)))}{\left(\begin{array}{c} c_2 v_1(2\gamma(P_1 - P_2) + \rho_1(v_1 - v_2)(3\beta v_1 - \delta v_2))+ \\ v_2(2\gamma P_1 v_1 + 2\gamma P_2(-2v_1 + v_2) + \beta\rho_1 v_1(3v_1^2 - 4v_1 v_2 + v_2^2)) \end{array} \right)}$$

(5.35)

The only dependence on incoming wavenumber appears for x_{shock} which contains $1/\omega = 1/k_{in} c_s M$.

Because the outbound postshock sound wave has amplitude comparable to the incoming entropy wave amplitude, it steepens within a few shock frame oscillation periods into a weak ($M \approx 1.003$) shock train. A partially nonlinear analysis that propagated the exact sound relations given by (5.1)- (5.5) might be of value, however the superposition of the linear result with the nonlinear simulation shows that we recover the expected outcome.

A fully nonlinear analysis would require accounting for the fact that the entire postshock region is a scattering problem, with multiple interacting characteristics of large (0.2 normalized) amplitude. Fourier analysis of a very high refined simulation ($N_x = 500,000$) showed, in the FFT of the shock front's position, nonlinear modulation terms without end.

Stability of radiative shock. Imogen supports optically thin radiation which takes the form of a simple sink of internal energy,

$$\frac{\partial \epsilon}{\partial t} = -\Lambda(\rho, P) = -k\rho^2 T^\theta$$

(5.36)

where we consider θ-parameterized radiation.

Radiation powered by particle collisions scales as ρ^2 because at least two particles must collide or graze, either to convert their kinetic energy into an excited state or for Bresmsstrahlung of ions/electrons to occur. Bremsstrahlung has $\theta = 1/2$ because the typical momentum two colliding/grazing particles have to exchange is proportional to thermal velocity which is proportional to $\sqrt{T}$ for nonrelativistic particles $(T_{e-} <\approx 10^9 K)$

A planar radiative shock profile may be derived by adding the radiation term to the Euler equations and asserting time-independence,

$$\partial_x \begin{bmatrix} \rho v_x \\ \rho v_x^2 + P \\ \rho v_x v_y \\ E_{flux} \end{bmatrix} = \begin{bmatrix} 0 \\ 0 \\ 0 \\ -\Lambda(\rho, P) \end{bmatrix} \tag{5.37}$$

The continuity, transverse momentum, and normal momentum equations may all be trivially integrated and found to equal constants. These then allow to solve for $\rho(v_x)$, $v_y(v_x)$ and $P(v_x)$. All are substituted into the energy equation, yielding a single ODE of the form

$$\frac{d}{dx}E_{flux}(v_x) = \frac{dE_{flux}(v_x)}{dv_x}\frac{dv_x}{dx} = -\Lambda(\rho, P) \tag{5.38}$$

Noting that everything but v_x itself was defined in terms of v_x from having integrated the earlier members of Eq. (5.37).

This equation is analytically solvable for integer and half integer values of θ. In the code, it is numerically integrated with 10 decimal accuracy using the adiabatic postshock solution as the initial condition.

The terminating condition depends on the choice of θ. If the advection component is ignored and we examine an isolated, stationary parcel of fluid then

the equation is also exactly solvable, with a form dependent on θ:

$$\frac{d}{dt}\left(\frac{P}{\gamma - 1}\right) = -\beta \rho^{2-\theta} P^{\theta} \tag{5.39}$$

$$\frac{d}{dt}\left(\frac{T}{\gamma - 1}\right) = -\beta \rho T^{\theta} \tag{5.40}$$

$$T^{-\theta} dT = -\beta(\gamma - 1)\rho dt \tag{5.41}$$

where we replace pressure with $T = P/\rho$ while assuming ρ is constant. This leads to solutions of the form

$$T(t) = (T_0^q + \phi(t))^{1/q} \tag{5.42}$$

away from special cases, with $q = 1 - \theta$ and $\phi = -\beta(\gamma - 1)(1 - \theta)\rho t$. The cases are:

If $\theta > 1$, then q and ϕ are both positive. The temperature profile over time is a fractional power, and cooling never finishes.

If $\theta = 1$ the special case of exponential cooling occurs (which also never finishes).

If $0 < \theta < 1$, q is positive and ϕ grows more negative with time. At the critical time t^*, the quantity in parentheses in (5.42) goes to zero and the temperature falls to zero at t^*. Because $0 < q < 1$, the decrease to zero temperature is smooth approaching t^*.

If $\theta = 0$ the radiation rate is temperature independent and the temperature drops linearly to zero in finite time.

If $\theta < 0$ the same runaway cooling as for $0 < \theta < 1$ happens, but the solution has a singular point at t^* which it approaches with infinite derivative.

Given the assumption that the preshock flow was nonradiating, a logical choice of where to end the integration of the flow is when the temperature returns to its preshock value. For a strong shock which heats the postshock fluid greatly,

112

this results in an ultimate compression $\rho_{fin}/\rho_0 \approx M^2$ such that the overall outcome resembles an isothermal shock.

There are then 3 regions initialized: A uniform preshock flow which is presumed to not radiate, a stationary adiabatic shock at the start of a cooling layer, and a cold dense region where radiation is again switched off.

A model of this type is widely considered as a starting point for both stellar accretion columns and for modelling the leading edge of the radiative snowplow phase of supernova remnants. These solutions are well known to support linearly-unstable nonlinearly-saturating modes for many values of θ, including weakly unstable behavior for $\theta = 1/2$ (see e.g. Chevalier and Imamura (1982) and Imamura, Wolff, and Durisen (1984) for linear analysis and emphasis of white dwarf accretion columns, and Strickland and Blondin (1995) and Blondin, Wright, Borkowski, and Reynolds (1998) for nonlinear numeric simulation)

Numerically capturing the steady solution represents a considerable challenge to a fixed grid. At the high Machs of interest, the stationary shock front is known to be positionally unstable for most shock profiles, and its very slow secular evolution is subject to the generation of slow post-shock oscillations, both of which are observed.

At high Machs, the base of the cooling regions presents a major resolution problem. At Mach 7, for example, even with a resolution of 10000 cells half of the final cooling occurs in the last 5 cells before radiation switches off. This is because the pressure contrives itself to remain (relatively) constant, so that for radiation exponents $\theta < 2$ the radiation rate diverges to ∞.

Another way to see the problem is that since $\Gamma \propto \rho^2 \propto (M^2)^2 = M^4$ for an isothermal shock (whose state the base of the cooling shock approaches),
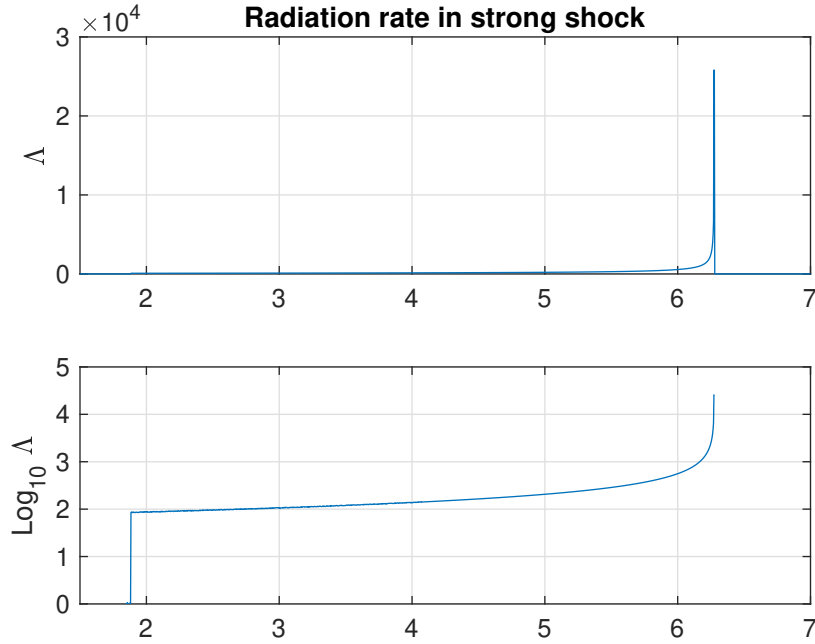
Figure 26. Plot of the radiation rate of a shock with M=10 and adiabatic index $\gamma = 5/3$ and radiation law $\theta = 1/2$ in linear and log scale. The cooling region is resolved by 1440 cells. The radiation rate immediately postshock is 85.9, and the radiation rates in the last 4 cells before cooling finishes are 4961, 4076, 6640, and 25800.

the resolution required to prevent total cooling in a single cell grows as the fourth power of the shock strength!

Code correctness tests - 2D. Two and three dimensional tests require that the operator splitting process maintain second order accuracy, and provide substantial additional freedom to do interesting things with flows.

Cross-grid wave transport. Transporting a sound wave at an angle across the grid provides a test of the isotropy breaking in GPU-Imogen due to the use of dimension splitting to acheive multi-dimensional operation. For this test, a (typically large) grid is chosen, along with a maximum wavenumber $\vec{N}_{max}$. Simulations of the same sound wave at all wavenumbers up to $\vec{N}_{max}$ are

run. All are run for the same time (chosen as $0.95t^*$ computed for the largest wavenumber) to remove dependence of the results on iteration count. Metric norms are computed, then scaled by $1/|N|^2$ (due to the effective scaling of resolution as $1/N$ and the observed 2nd order convergence) to remove the expected resolution dependence.

If the expected resolution dependence were the only dependence, then at this point all norms should be identical. Regrettably the underlying structure of the equations being solves means that they are not. The square grid breaks continuous rotation symmetry in space, and the operator splitting scheme breaks it in both time and space.

As can be seen in the plots of figure 27, the results are however very close to isotropic. This can be quantified by normalizing the standard deviation of the prefactors (which would be zero in the case of perfect isotropy) by their mean. For the test conditions run, the result is

$$\frac{\sigma_1}{\mu_1} = \frac{6.03759 \times 10^{-6}}{4.52471 \times 10^{-5}} = .1334 \tag{5.43}$$

$$\frac{\sigma_2}{\mu_2} = \frac{2.53809 \times 10^{-5}}{1.40048 \times 10^{-4}} = .1812 \tag{5.44}$$

Which indicates that the truncation error (though always very small) varies by around 15% depending on the orientation of the wavevector with respect to the grid.

Operator splitting sequences with higher order accuracy in the splitting are well known for some classes of differential equations. However, higher order splittings require either negative timesteps, that certain branches in the tree of error commutators vanish, or both. While other important sets of differential equations, such as quantum operators and the gravitational N-body equations,

115
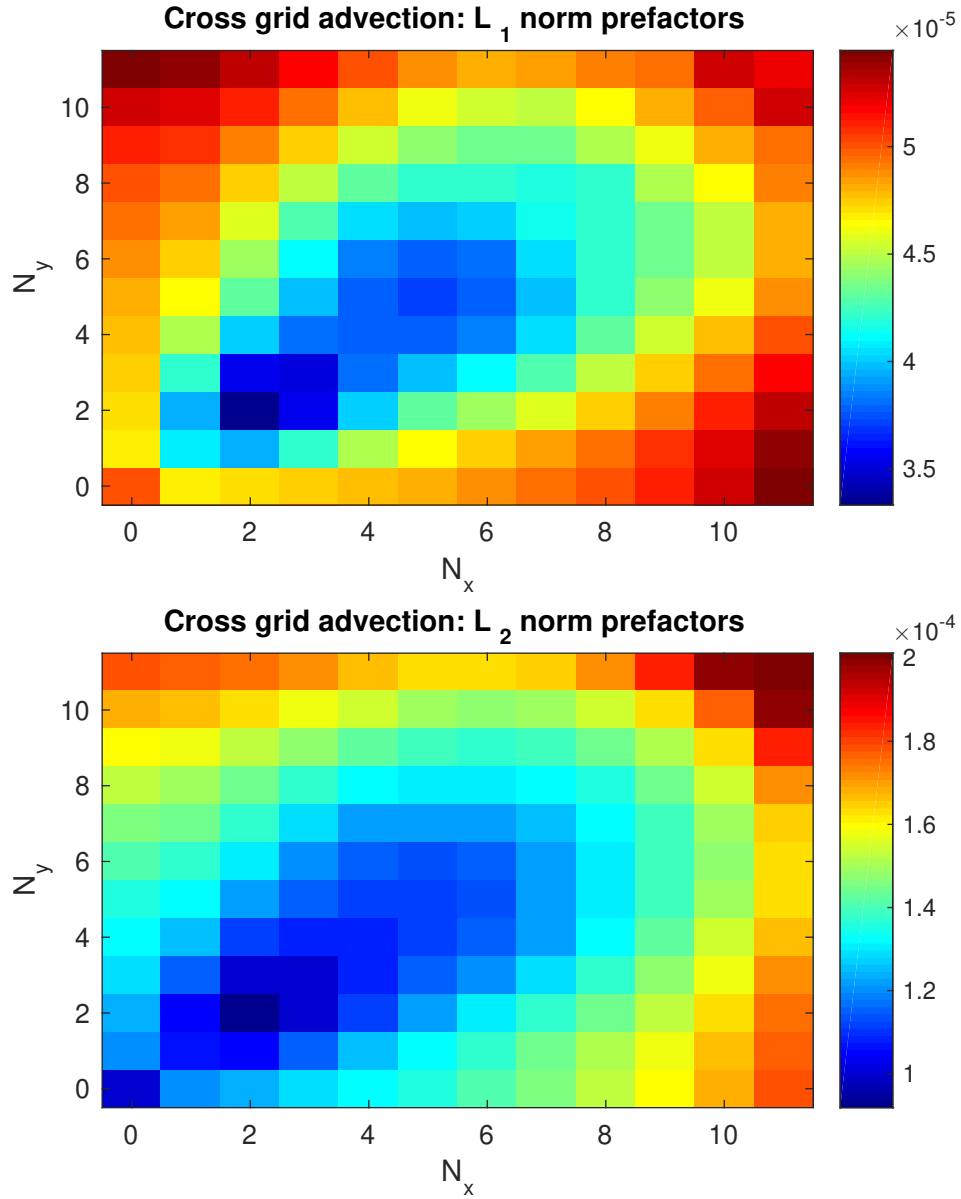
Figure 27. Convergence of a sonic characteristic propagating with wavenumbers as marked. Value for $\vec{N} = (0, 0)$ invalid. Initialization on unit square using Eq. (5.1)-(5.5) with $\vec{k} = 2\pi\vec{N}$, circular boundary conditions and a wave amplitude of .05. All simulations share common end time $t = 0.95t^*(\vec{N} = (11, 11)) \approx 0.874739$. Grid resolution fixed at 1536×1536, minimum effective resolution occurs for max wavenumber having ≈ 100 cells/wavelength.
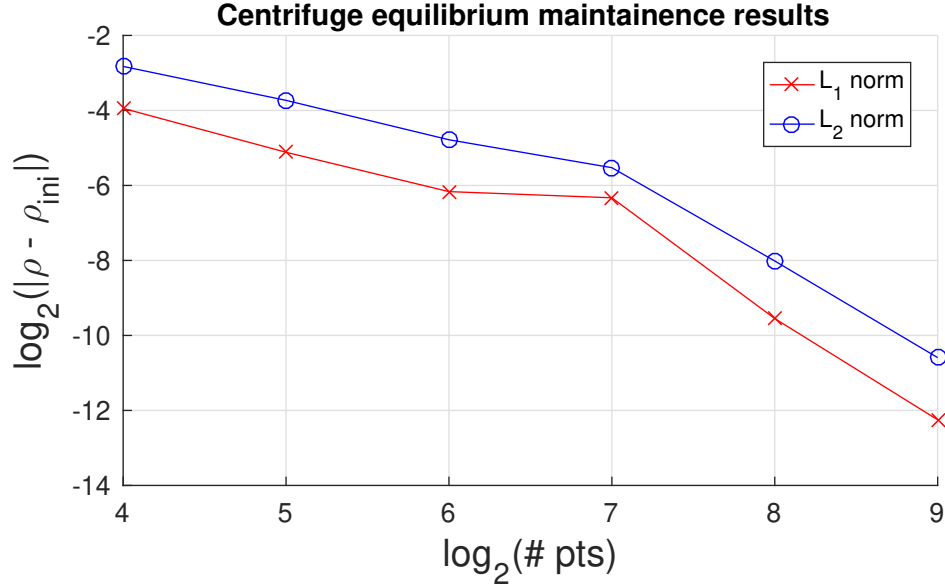
Figure 28. Convergence of a centrifuge equilibrium toward time-independence

meet these requirements and have seen great returns from higher order operator split methods, this is the not the case with the Euler equations: They are nither time reversible (which forbids negative timesteps) nor can any commutator terms in their (time dependent, nonlinear) evolution operators be expected to vanish.

We also note that larger wavenumbers (toward the upper right corner of the figures) are nearing the resolution at which they begin to deviate from asymptotic behavior.

Gresho test. The Gresho test was introduced in Gresho (1991) and among those used in Liska and Wendroff (2003) to compare numerous CFD schemes/packages.

It consists of a two-dimensional system with cylindrical symmetry in which pressure and centripetal effects due to axisymmetric rotation balance. The fluid rotates on cylinders with the form $v(r, \theta, z) = f(r)\hat{\theta}$, which generates a divergence-free flow for any choice of f. Assuming axial symmetry, the continuity equation

117
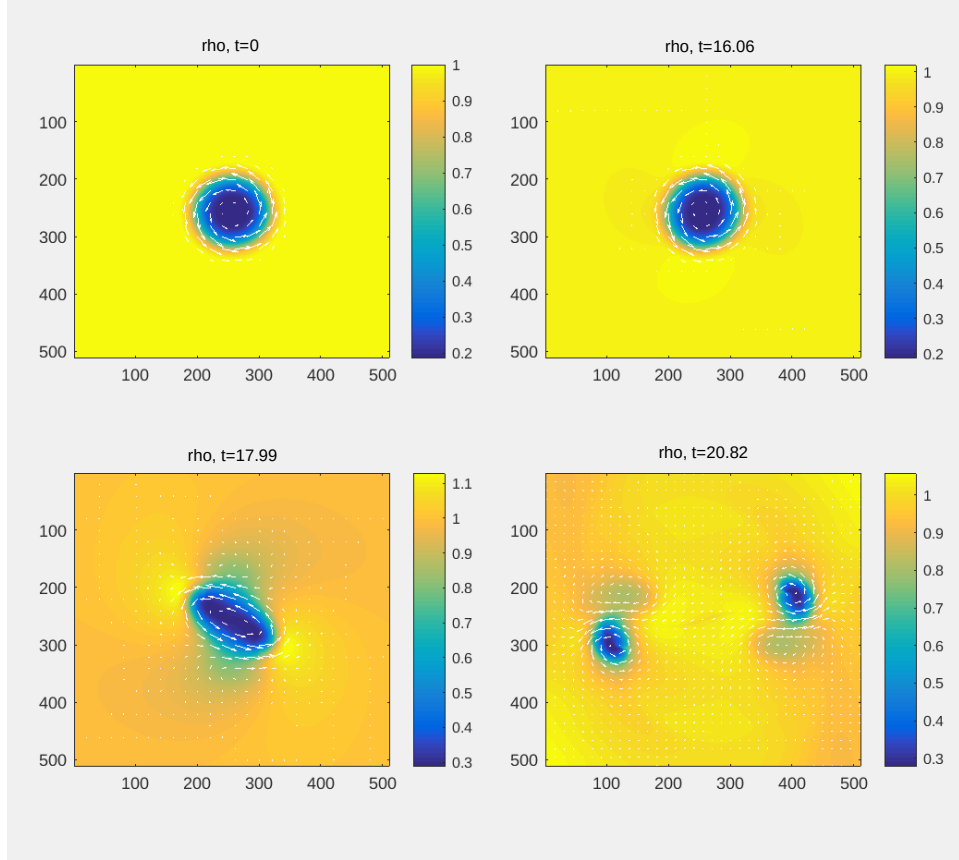
Figure 29. A particular centrifuge with rotation curve $\omega(r) = \omega_0(1 - \cos(2\pi r))$ on $r \leq 1$ and $\omega = 0$ for $r > 1$, with $\omega_0 = 1.5$. The grid spans $(-2.5, -2.5) \times (2.5, 2.5)$. The rotation curve yields a rotation period of $\tau(r = 0.5) = 2.09$. As can be seen, the structure remains stable for about 8τ before a normal mode appears, then it deforms into a bar by 9τ and fragments into pieces by 10.5τ.

is identically solved for any axisymmetric density distribution. The constraint of relevance is the radial force balance version of the momentum equation,

$$\frac{dv_r}{dt} = 0 = \rho(r)v_\theta(r)^2/r - \partial_r P(r) = \rho(r)r\omega(r)^2 - \partial_r P(r) \tag{5.45}$$

This problem is solvable through the same potential integral method that yields a Kojima model protostellar/protoplanetary disk, albeit with quite different boundary conditions.

118

With only one constraint per point, two more constraints or assertions are necessary to specify an initial condition. The typical choice is to assert some rotation curve, and to pick an equation of state that allows to write $P(\rho)$, at which point Eq. (5.45) gives a (usually integrable by design) ODE for ρ. Depending on the choice of EoS, not all rotation curves are compatible with physical density profiles (instead ending with vaccuum inner edges). Another workable choice is to prescribe some temperature curve $T(r)$ and compute $P = \rho T$ to get an ODE for ρ.

Generally the rotation curve should be nonsingular at the origin and have compact support on the computational domain (outer boundary $v_\theta \to 0$) yielding a finite interesting region embedded in a uniform, stationary background.

Exact time-independent equilibria are evolved, and accuracy is considered based on how well they maintain time-independence. These vortices are expected to be unstable against both axisymmetric instability in 3D as well as axially asymmetric modes in both 2D and 3D.

This test is run in square geometry and serves mainly to test the operator splitting and general accuracy in square coordinates.

Reflected blast test. The reflected blast test specifies an initial set of riemann problems which generate a chaotic central region containing subsonic turbulence.

The initial condition is defined on the square $[0, 1] \times [0, 1]$, with mirror boundary conditions on both axes with the fluid state

$$\rho(x + y > 0.5) = 1, P(x + y > 0.5) = 1 \tag{5.46}$$

$$\rho(x + y < 0.5) = \rho_{corn}, P(x + y < 0.5) = P_{corn} \tag{5.47}$$

We use $\rho_{corn} = .125$ and $P_{corn} = 0.14$. The simulation is executed on a grid of resolution 768^2 and run for a total of 100,000 iterations ($\approx$ 75 initial sound crossing times).

Because the problem begins with perfect mirror symmetry about $x = y$, it should nominally maintain the symmetry forever. However second order operator splitting does not maintain XY symmetry and therefore perfect symmetry cannot hold.

In the case of the reflected blast test, the asymmetry seen in density/temperature is amplified as the shocks repeatedly run across the contact discontinuity separating originally-dense and -tenuous gases, and the low-density region becomes chaotic. After a couple of reflections, the shocks' Mach inevitably drops to a value not greatly more than 1 due to dissipation, and dissipation quickly slows.

However, while the asymmetry is very obvious in density and temperature, it is largely invisible in pressure. Even after dozens of dynamic times, even if the density profile is obviously asymmetric due to weakly stable shear modes forming vortices, the locations of the shocks running back and forth remain quite close to (though not perfectly) symmetric.

Because all boundaries are mirrors, total mass upon the grid should be perfectly conserved. Noting that an edge cell that straddles the mirror counts for half, and a corner cell that straddles both counts for one quarter, a 768^2 blast chamber was let to run for 100000 steps and the mass on grid was checked at every timestep. The result is plotted in figure 31: Conservation was identical to the limit of double precision. The change in total mass on grid fluctuated by -3 to +5 $\times 10^-15$, a value so close to zero that the quantization of double precision

Temperature in reflected implosion test at t=5
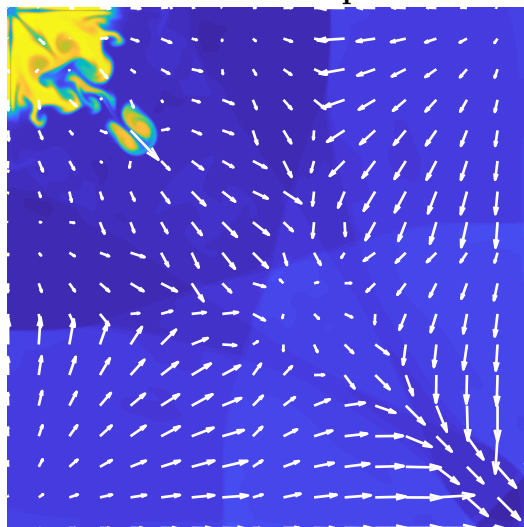
Figure 30. The temperature of the implosion test chamber at t=5, imaged in temperature, with velocity vector arrows overlaid. Simulation resolution was 512^2. Initial symmetry breaking is just visible.

numeric representation is clearly visible. The sum of mass was performed by Matlab's `sum()` function which uses compensated summation to assure that the result is accurate.

2D Riemann problems. Here numeric solutions to several 2D Riemann problems are presented. They may be compared to the results published in the locations indicated with each figure.

Some of these demonstrate the existence of the chaotic central region of the 2D RP, which for a long time caused considerable difficulty in the formulation of unsplit solvers upon solid theoretic grounds.

Rayleigh-Taylor instability. The Rayleigh-Taylor instability, as originally analyzed by Lord Rayleigh in 1883, describes the instability of a heavier fluid balanced on top of a lighter one. The classic example is water balanced on top of oil: If a surfactant removes the surface tension that stabilizes the
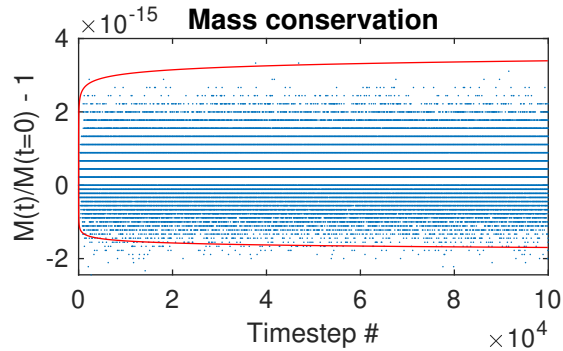
Figure 31. The total mass on the grid of a 768^2 implosion chamber was tracked. Ideally there would be no deviation from zero. The actual total change, as can be seen, is nearly as close to zero as double precision can represent. +1 and -.5 $\times 10^{-15}\sqrt{\log x}$ are plotted showing expected growth of errors introduced by the nature of float point math.

arrangement, it overturns. Another example is atmospheric inversions which balance cold, dense air on top of warmer, lighter air. When this arrangement breaks down and if the turbulence reaches the surface, the result is the appearance of intense, randomly-varying wind gusts "out of nowhere."

Somewhat more generally, the instability is that of any lighter fluid accelerated into a denser one, either by a pressure driven flow or by gravity. Looking at things from an energy perpective the origin of the instability is clear: heavy fluid is "higher up" than lighter fluid and it is energetically preferable for them to exchange positions.

Two sets of 2D Rayleigh-Taylor simulations were run. They were initialized on unit boxes with a resolution of 512^2. Density was 1 for $x < 0.5$ and 2 for $x > 0.5$. Equilibrium velocity is zero everywhere. The classical analysis is incompressible, however our fluid must have a finite soundspeed. Therefore a gravity field pulls left with a strength of 0.1. Initial pressure at x=0 is 2.5, and is solved for vertical balance against gravity.

RP # 1: From Clawpack-4.3
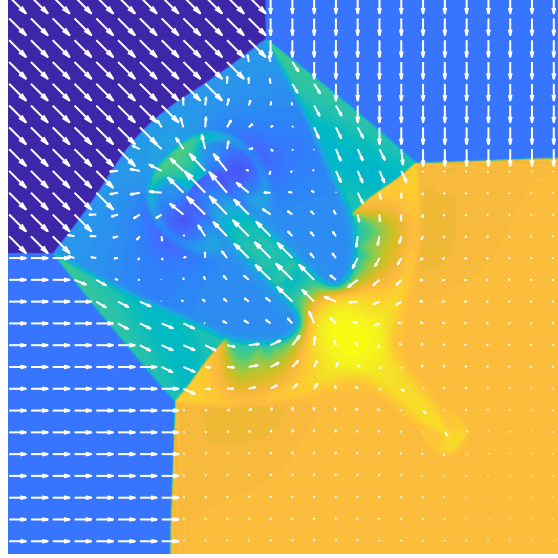
Figure 32. A four quadrant RP. Initial states given as $[\rho, v_x, v_y, P]$, clockwise from lower right: $[1.0, 0, 0, 1.5]$, $[0.53225, 1.206, 0, 0.3]$, $[0.53225, 0, 1.206, 0.3]$, $[0.13799, 1.206, 1.206, 0.029032]$. $\gamma = 1.4$. Grid is a unit box. Boundary condition = extrapolate constant. RP initially centered on $(0.8, 0.8)$. Evolved from $t = 0$ to $t = 0.8$

The sinusoidal perturbation altered the velocity as

$$v_y(x, y) = 0.1 cos(4\pi x) exp(-4\pi|y - 0.5|) \tag{5.48}$$

and the random perturbation took the form

$$v_y(x, y) = 0.1 rand(x) exp(-4\pi|y - 0.5|). \tag{5.49}$$

In both cases the perturbation is decayed away from the interface and assumes a very small value at the walls. The boundary conditions are circular vertically, mirror at the left wall and free balance at the right wall.

The sinusoidal perturbation leads directly to the classic RT "mushroom cloud". The random perturbation creates structure with a much smaller size in the Y direction. From the linear instability analysis (in which $\omega_r \propto k$), the

RP #2: From Wendroff 2003
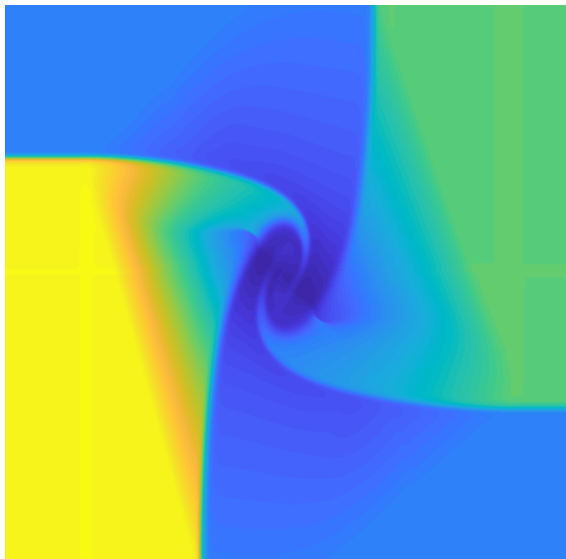
Figure 33. A four quadrant RP. Initial states given as $[\rho, v_x, v_y, P]$, clockwise from lower right: $[1, 0.75, -0.5, 1]$, $[3, -0.75, -0.5, 1]$, $[1, -0.75, 0.5, 1]$, $[2, 0.75, 0.5, 1]$. $\gamma = 1.4$. Grid is a unit box. Boundary condition = extrapolate constant. RP initially centered on $(0.5, 0.5)$. Evolved from $t = 0$ to $t = 0.3$.

higher wavenumbers in the random perturbation should grow faster. However, the random perturbation's small structure also reaches the nonlinear regime much sooner and the growth of small fingers is slower than that of a few large fingers.

2D Sedov-Taylor explosion. The Sedov-Taylor explosion, as a model of either an atomic explosion or supernova, considers the deposition of a finite energy E into a delta function at the origin of a uniform, cold (pressureless) fluid. This was the solution originally published by Sedov. Later work by Kamm and Timmes in Kamm (2000) and Kamm and Timmes (2007) generalizes the exact solution to arbitrary spatial dimension, and of power-law distribution of density, $\rho \propto r^w$, as well as providing the algorithm for exact solution in all cases. (We note that at least one erroneous factor appears in the 2007 paper that is not present in the 2000 one).

Rayleigh-Taylor instability simulations
Left, sinusoidal perturbation; Right, random perturbation
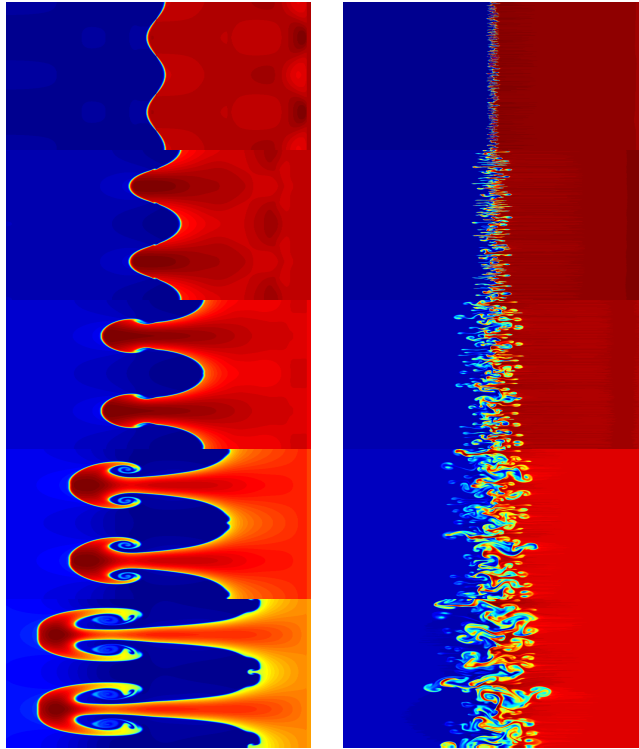
Figure 34. Frames from two sets of Rayleigh-Taylor simulations. Both are initialized in boxes of size 1, on grids of size 512^2. Density of the left half is 1, of the right half is 2. Gravity field strength is set to 0.1, and from a maximum pressure of 2.5, the pressure gradient is set to hold equilibrium. Images are taken at times of 0.5 to 2.5 in steps of 0.5. The perturbations are given in the text.

In GPU-Imogen the classic case ($w = 0$), the one Sedov considered as a model of a nuclear explosion, is tested in space dimensions 2 and 3. It often presents problems with formal convergence metrics, especially by measurement of density, because the great majority of the area/volume of the blast is extremely tenuous which causes small errors in density to become large errors when normalized.

Depositing the energy into a finite spherical volume (containing multiple cells) predictably results in an improvement in circularity / sphericity, but

obviously deviates from the idea of a point explosion. This can be done in two ways. The simple one which can be implemented trivially for any radius is to deposit equal energy into all cells whose center's radius is less than r_0, then normalize such that total energy equals the blast energy.

The better solution, implemented for small radii, is to properly integral-average a disk/sphere whose radius touches some particular coordinate point. Four such integrals are available for 2D: Assuming square cells with dimension
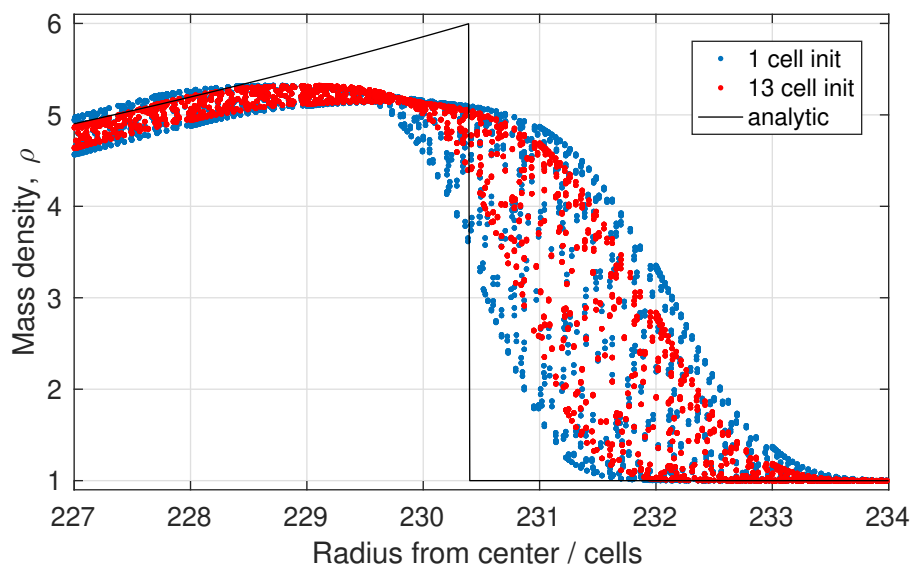
Figure 35. Scatterplot of density vs radius from a 512^2 Sedov-Taylor explosion on a unit square with $\rho_0 = 1$ and $E_{blast} = 1$, evolved to $r_{blast} = 0.45$ ($t = 0.20088$). Blue dots were from initialization into a single cell, while red were from initialization into a radius of $\sqrt{2.5}$ (13 cells): Initialization into a small finite volume improved circularity by about 30%. In both cases the shock is captured in a width of about 2 cells, with a deviation from circularity of about 1 or 1.5 cells (out of a diameter of ≈ 450 cells). The extremely narrow structure of density behind the blast - at this resolution ρ drops 16% in the space of 2 cells - dominates the metric errors and causes them to converge very slowly. Note that the variations in max density (the lower left line corresponds to grid-aligned, and the higher right line to 45 degrees across) which contribute so much to the metric error are almost entirely an artifact of the multi-dimensional shock profile: The Mach of the shock front at this point is still in the hundreds.

126

normalized to one, to circles with radius zero (1 cells), radius $1/\sqrt{2}$ (5 cells), radius 1.5 (9 cells) and radius $\sqrt{2.5}$ (13 cells). Three such integrals are available in 3D. Assuming cube cells of unit size, for circles of radius zero (1 cell), radius $1/\sqrt{2}$ (7 cells) and radius 1.5 (27 cells).

These simulations take 20 steps using the HLLC solver before switching themselves to the HLL flux solver. HLL requires an inordinately small timestep at small times, or it yields ugly odd-even decoupling glitches along the coordinate axes, while HLLC at long times suffers the carbuncle instability.

The ST explosion is also notable for exhibiting the carbuncle instability if the HLLC flux solver is used for the whole simulation time. The carbuncle is an artificial instability present in certain classes of flux solvers in which hydrodynamic shocks, which should be unconditionally stable, instead exhibit various strange malefictions in the vicinity of grid-aligned flow. The problem appears to be connected with any solver which represents a shear wave according
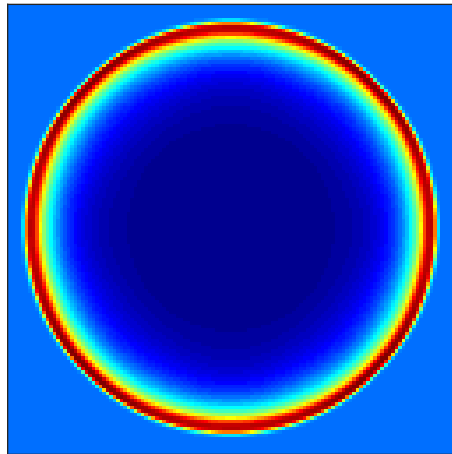
Figure 36. A small 128^2 simulation of the above described blast with the shock capturing cells visible.
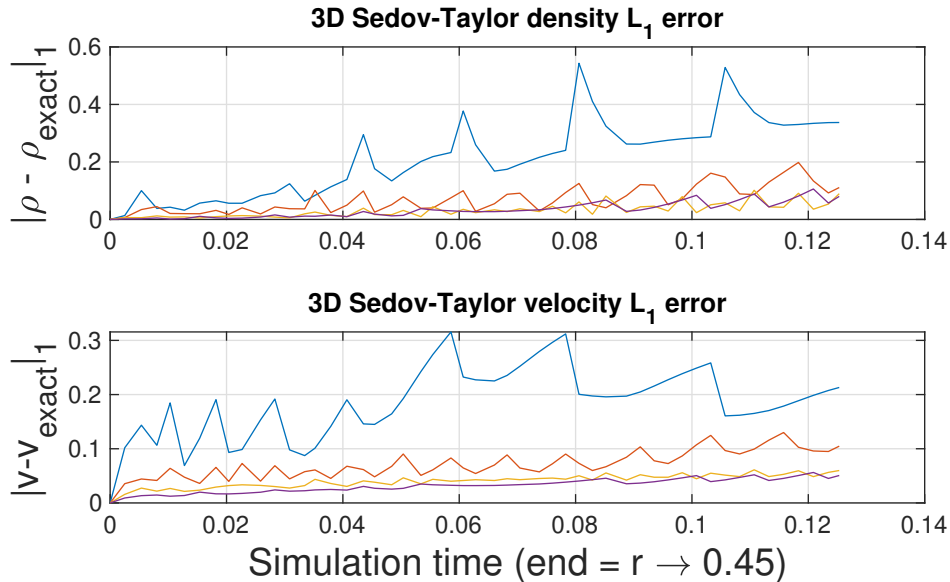
Figure 37. Plots of the 1-norm of the density and velocity error for Sedov-Taylor runs at resolutions of 16 (blue), 32 (red), 64 (orange), 128 (purple), 256 (green), 512 (cyan) squared, with both axes mirrors for double effective resolution. Formal convergence is slow but present.

to Dumbser, Moschetta, and Gressier (2004), among which HLLC is prototypical representative.

Code correctness tests - 3D. Most of the tests done in two dimensions have a nontrivial extension to three dimensions. Tests done in three dimensions are also notable because, especially with any appreciable grid refinement, they cannot be done even workstation class computer, and require the use of fully parallel computing resources: A 1024^3 simulation, for example, requires roughly 90GB total of memory in GPU-Imogen.

3D reflected blast test. A three-dimensional unit cube was initialized with velocity zero everywhere and a Riemann problem with normal $\vec{n} =< 1, 1, 1 >$

with values

$$\rho(x + y + z > 0.8) = 1, P(x + y + z > 0.8) = 1 \tag{5.50}$$

$$\rho(x + y + z < 0.8) = \rho_{corn}, P(x + y + z < 0.8) = P_{corn} \tag{5.51}$$

As in the 2D case we use $\rho_{corn} = .125$ and $P_{corn} = 0.14$ and the simple ideal gas EoS with $\gamma = 7/5$.
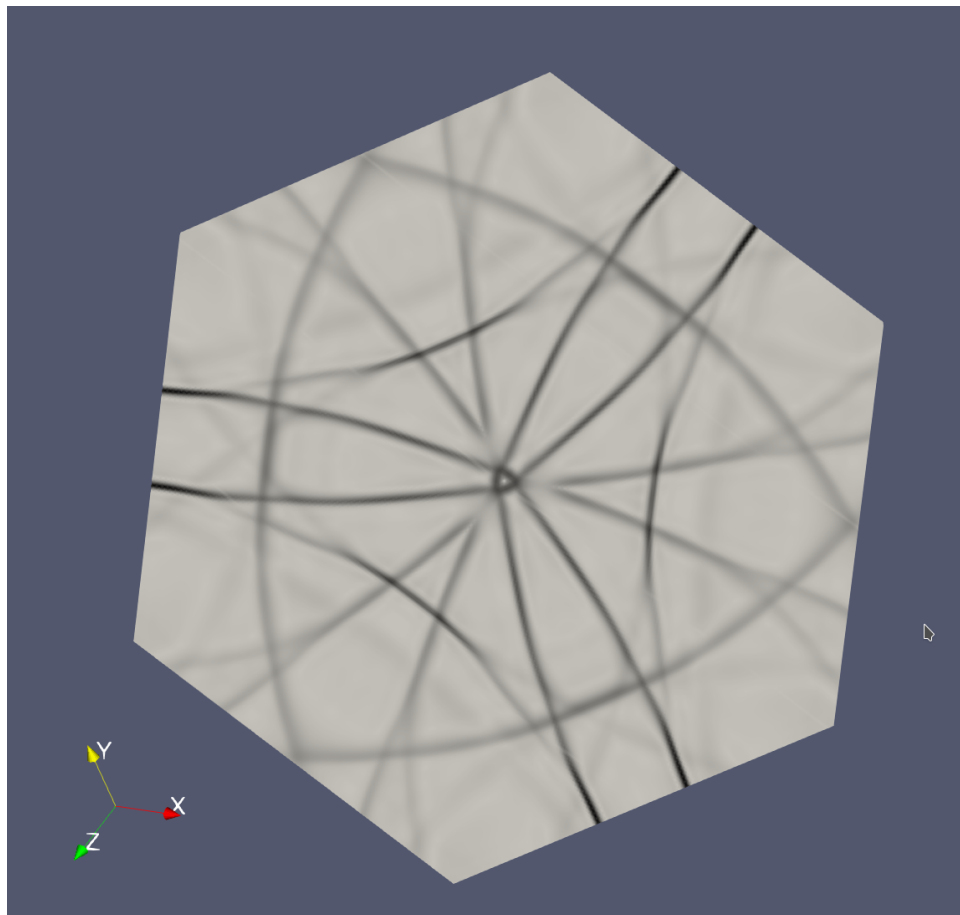
Figure 38. Schlieren-like visualization of $|\nabla \rho|$ of a 3D implosion chamber at t=4.957 (about 6 sound crossing times) revealing the shock waves continuing to echo across the chamber. The image plane has normal $< 1, 1, 1 >$ and passes through the center of the simulation volume: Note that at this point there is no detectable deviation from trigonal symmetry. This simulation used a resolution of 256^3.

In the 2D case the expectation is of maintaining reflection symmetry about the $< 1,1 >$ axis because the initial conditions are identical under that parity transform. This is equal to embedding the 2D solution in 3 dimensions and rotating it by $n \times 180 \deg$ about the $< 1,1 >$ axis). In the 3D case, trigonal symmetry is evident about the $< 1,1,1 >$ axis because the initial condition is (and its evolution should be) symmetric under rotations of $n \times 120 \deg$ about the $< 1,1,1 >$ axis.

This symmetry is confirmed in simulations at early times, as well as its inevitable breaking at later times due to amplification of truncation errors in weakly stable entropic structure.

3D Sedov-Taylor explosion. As in two dimensions above, the ST explosion is tested in three dimensions. These tests were run using all three axes mirrored, doubling the effective resolution of each run. As is visible in the plots below, the Sedov-Taylor explosion has erratic and slow convergence. This is associated with the extremely thin layer of spatial structure behind the shock, which is difficult to accurately capture, and the fact that because the shock structure grows as the 2/5 power of time, the number of cells involved grows as the 1.2 power of time and the number of cells at the surface of the blast grows as the 0.8 power of time.

Thus, given that the error in cells near the shock front will always be $O(1)$, at best convergence metrics will be something like $1/N^{0.2}$. None the less, there is a decrease in the error measurements initially and despite the seemingly bad numbers, the exact and numeric solutions look extremely similar.
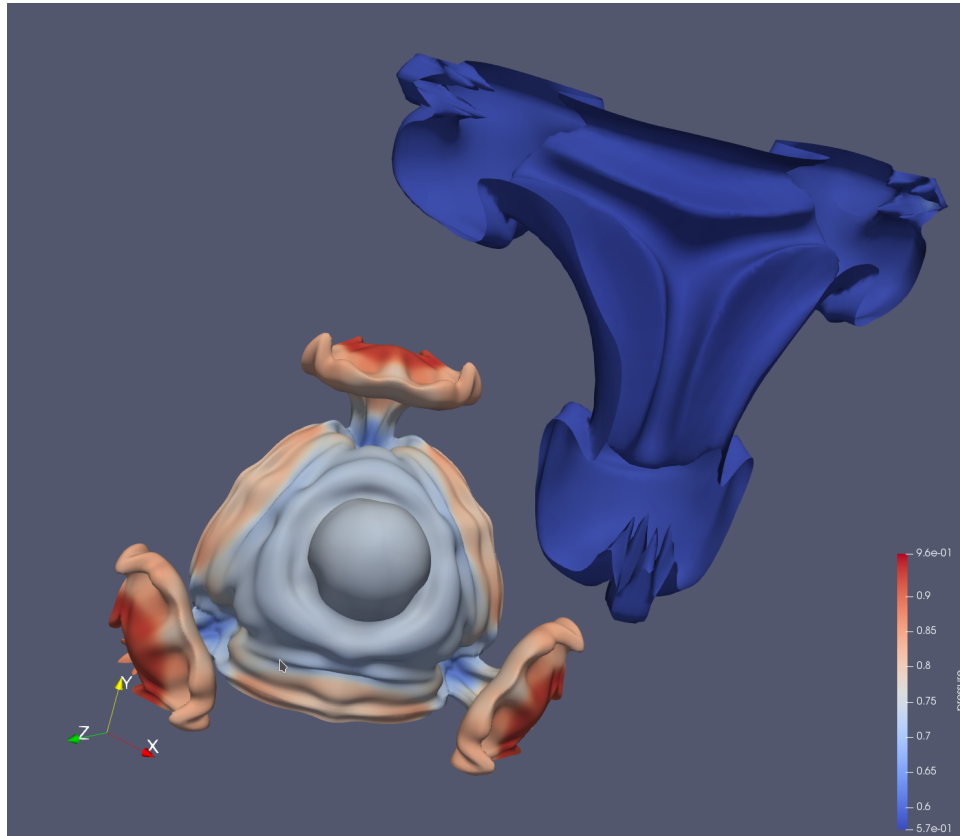
Figure 39. A three dimensional visualization of the implosion chamber at t=4.652 showing the contour of $\rho = 0.64$, colored by pressure. The three plumes launched along the edges of the cube are visible, as is the knob-like plume launched along the $< 1, 1, 1 >$ normal. This, and an additional contour at the opposite corner of the simulation, all exhibit the trifold symmetry.

Known limitations. It is well known (see e.g. Dumbser et al. (2004)) that numeric schemes of the type employed in GPU-Imogen are not quite unconditionally nonoscillatory in the resolution of planar shocks. A sufficiently strong shock always has some profile ("position" within the cell) which is unstable to moving off that profile, a defect related to the fact that the (linear) reconstructions generated by the finite shock profile fail to trace the Rankine-Hugonoit loci, even if the underlying flux scheme exactly captures a thin (zero-cell-wide) shock that is aligned on a cell boundary (both HLL and HLLC do so).
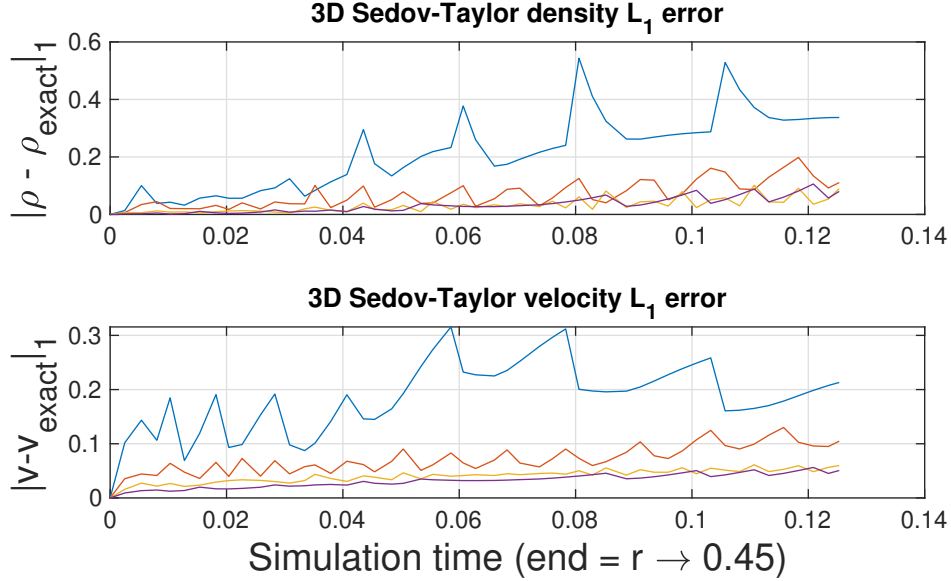
Figure 40. Plots of the 1-norm of the density and velocity error for Sedov-Taylor runs at resolutions of 24 (blue), 48 (red), 96 (orange) and 192 (purple) cubed. Convergence is erratic but present.

In such cases, a slowly moving shock ($|v_{sh}| << c_s$) is known to experience shock front oscillation as the numeric shock position jumps from interface to interface. This is evident in the later stages of the double blast test, and particularly visible in the Noh shock tube: The first shock propagating toward the wall shows no untoward oscillation, while the second one bouncing off it does.

The code also has some limitations in the handling of radiation loss, which are discussed at length in section VI, and with handling two-fluid flow with tight coupling which are covered at the end of II.

CHAPTER VI

SIMULATIONS AND RESULTS

The GPU-Imogen code has been employed to simulate radiative shocks in one, two and three dimensions. The large number of one dimensional simulations has been compiled into a data bank of observables and properties as functions of shock parameters over a wide range of parameters.

All simulations utilize the truncated radiation law

$$\dot{e}_{int} = -\Theta(T-1)\beta\rho^2 T^\theta \tag{6.1}$$

where θ is the temperature scaling law ($\theta = 0.5$ corresponds to free-free bremsstrahlung) and $\Theta(x)$ is the Heaviside step function that truncates cooling. Thus the generated equilibria are in fact detailed models of isothermal shocks: The preshock temperature is normalized to 1 and cooling is cut off when the postshock temperature drops to 1. The strength of cooling is represented by β.

In the code, β is tasked with absorbing all dimensionful prefactors, including those originating from dropping μ/k_b when using $T = P/\rho$. The units are such that $\rho_{pre} = P_{pre} = \beta = 1$.

The instability of a similar problem - a shocked flow settling onto a wall at T=0 - is of interest as a model of white dwarf accretion. This was analyzed linearly by Chevalier and Imamura (1982) among others. They found that in the strong shock limit the flow is potentially subject to multiple linearly unstable modes - denoted as F, 1O, 2O, etc after classification of stellar radial oscillation modes - depending on the cooling law θ parameter.

Solving the Rankine-Hugoniot conditions for the postshock parameters and computing the shock position and cooling time, it is suggested that

$$w\frac{\partial X_{\text{shock}}}{\partial w} > NwT_{\text{cool}} \rightarrow \text{instability.} \tag{6.2}$$

The heuristic argument is that the left side represents the change in equilibrium shock height X_{shock} when the shock front velocity is perturbed by w, and the right the distance the front will move before feedback can allow it to "recompute" where it "wants" to be, which is proportional to the cooling time. This analysis, for a strong shock, leads to the result that

$$2\theta < 3 - CN \tag{6.3}$$

where C is the shock compression ratio ($\frac{\gamma+1}{\gamma-1}$ equals 4, 6 and 8 for $\gamma = 5/3$, 7/5 and 9/7 respectively) and N is the numeric constant. In reality, it ends up being observed stability thresholds for θ that inform the feedback to cooling time ratio N, but none the less the implication that there is an upper θ for instability to be present is clear and correct.

Direct numerical simulations were performed by Strickland and Blondin (1995) on a similar problem with a different bottom boundary condition - that of radiation cutoff rather than to T=0 - owing to the singularities introduced by permitting T to reach 0. They confirmed that multiple modes exist in the nonlinear regime analagous to the F/1O/2O/... and that the saturated nonlinear pattern frequencies agreed with the linear oscillation rates. While the limited processing power available prevented a wide ranging nonlinear survey, the basic result was confirmed that the oscillation frequencies and the underlying instability are largely independent of how the cooling region is terminated for strong upstream shocks

Here, we consider flows at three adiabatic indices (5/3, 7/5, 9/7), radiation theta values ranging from -1.0 to +0.5, and shock strengths from Mach 2 to Mach 10. For each adiabatic index a body of around 500 simulations has been obtained. From the radiation rate temperature dependence exponent of a radiating plasma (see 5 & Gehrels and Williams (1993) for details), such exponents correspond to postshock temperatures of around 200 thousand Kelvin and above.

The methodology behind equilibrium generation is presented, followed by a description of various oscillatory behaviors that have been observed. The analysis tools used to examine the time series data from simulation are described, and results are presented per adiabatic index.

Two dimensional simulations were performed on parameters which oscillate in the F, 1O and 3O modes in 1D, at a spatial resolution of 2048 cells in the cooling direction and 10240 transverse, with 512 cells in the cooling region. This necessitated the use of relatively moderate shock strengths to avoid the cold layer resolution problem, but the overwhelming similarity between all modes of a given type suggests that their behavior should also be representative.

Finally, the result of simulations of a global 3D simulations of three stellar bow shocks, featuring no radiation, $\theta = 1/2$ radiation, and runaway $\theta = -1/2$ radiation are presented. The 3D simulations covered the initial grid-symmetry breaking and several complete cycles of cold layer formation, dissolution to turbulence, and reformation/stabilization during 35000 timesteps. The numeric spatial resolution was 768x768 transverse and 512 flow direction, for a total of 225 million voxels. These results were acheived using only 4 K-80 GPUs with a single day of wallclock time.

Equilibrium solutions. The equilibrium stucture with which the simulations are initialized contains three regions: A uniform preshock region, a thin shock at the front of the cooling layer, and a uniform cold region (which matches the postshock result for a planar isothermal shock). The assumption of thinness implies that the mean free path for re-thermalization must be much shorter than the cooling length.

The equations for a radiating one dimensional flow with adiabatic index γ are restated for convenience:

$$\partial_t \begin{bmatrix} \rho \\ v \\ .5\rho v^2 + P/(\gamma - 1) \end{bmatrix} + \partial_x \begin{bmatrix} \rho v \\ \rho v^2 + P \\ v(.5\rho v^2 + \frac{\gamma P}{\gamma - 1}) \end{bmatrix} = \begin{bmatrix} 0 \\ 0 \\ -\Theta(T - 1)\rho^2 T^\theta \end{bmatrix} \quad (6.4)$$

where the subscript v_x on velocity has been dropped to just v. The transverse components of velocity remain constant for these radiating flows, as they do across the shock, due to conservation of transverse momentum ($\partial_x(\rho v_x v_y) = 0$ combined with $\partial_x(\rho v_x) = 0$).

The mass equation can immediately be integrated exactly to yield a constant (named 'px' in the code) and an expression for $\rho(v)$, and the momentum equation can be integrated to yield another constant (named 'fx') and an expression for $P(v)$. This reduces the problem to a single autonomous ODE in a single variable for the evolution of internal energy density. This takes the generic form of

$$\frac{dy}{dv} = f(v) \quad (6.5)$$

. The numerical simulation naturally requires the output in position space, and we change the independent variable to x,

$$\frac{dy}{dx}\frac{dx}{dv} = f(v) \rightarrow \frac{dy}{dx} = f(v)\frac{dv}{dx}. \quad (6.6)$$

This gives the term c_1 in the equation (6.9) below,

$$\frac{dv}{dx} = c_1 = \frac{P^\theta \beta (\gamma - 1) \rho^{2-\theta}}{p_x v - P\gamma} \tag{6.7}$$

in which $P(v) = fx - pxv$ and $\rho(v) = px/v$ are analytic functions of the velocity v. The single ODE is solved as an IVP with the initial condition at $x = 0$ equal to the stationary shock solution of the Rankine-Hugoniot equations for the given shock strength, and integrated with respect to x until the temperature drops to 1.05 (for numeric reasons). We note that equation 6.7 is analytically solvable for integer and half-integer values of θ.

As part of the initialization of the equilibrium solver, initial step points are required; At all regular points, the flow ODE has a Taylor series expansion. Using the *Mathematica* CAS, a program to symbolically evaluate the coefficients c_n in the expansion

$$v(x) = \sum_{n=0}^{\infty} c_n x^n \tag{6.8}$$

was written which recursively solves for these coefficients c_n in terms of input constants and previous c_n, generating ever larger polynomials in terms of values at $x = 0$, the adiabatic index γ and the radiation index θ.

Though it is possible to recursively substitute the previous c_n in, the resulting equations grow larger rather than smaller, meaning that there is no great cancellation of terms. Or at least not one that Mathematica's `FullSimplify[]` can find.

The first four coefficients c_n can be given in a relatively reasonable space, and these are:

$$c_1 = \frac{P^\theta \beta (\gamma - 1) \rho^{2-\theta}}{p_x v - P\gamma} = \frac{dv}{dx} \tag{6.9}$$

$$c_2 = -c_1 \frac{(p_x(\gamma - 1)(\frac{P^{\theta-1}\beta(P(2-\theta)+p_x v\theta)\rho^{2-\theta}}{p_x v} + \frac{\gamma+1}{\gamma-1})}{2(p_x v - P\gamma)} \tag{6.10}$$

$$c_3 = -\frac{p_x(\gamma+1)c_1 c_2}{p_x v - P\gamma} - \frac{\begin{pmatrix} P^{\theta-1}(\gamma-1)\rho^{2-\theta}(-((\beta(6P^2 + (6f_x P - f_x^2 - 10P^2)\theta \\ +(f_x - 2P)^2\theta^2)c_1^2)/(Pv^2)) + 2\beta(p_x\theta - P(\theta-2)/v)c_2) \end{pmatrix}}{6(p_x v - P\gamma)} \tag{6.11}$$

$$c_4 = -\frac{p_x(\gamma+1)(c_2^2 + 2c_1 c_3)}{2(p_x v - P\gamma)} - \frac{\begin{pmatrix} (P^{\theta-3}\beta(\gamma-1)\rho^{1-\theta}(f_x^3(\theta-2)(\theta-1)\theta\rho c_1^3 \\ -4P^3(\theta-1)(-3+2\theta)c_1((-2+\theta)\rho c_1^2 + 3p_x c_2)+ \\ 12P^4(\theta-1)c_3 + f_x(6P^2\theta(2\theta-3)c_1((-2+\theta) \\ \rho c_1^2 + 2p_x c_2) + 6P^3(2-3\theta)c_3) + f_x^2(6P(1-\theta) \\ \theta c_1((\theta-2)\rho c_1^2 + p_x c_2) + 6P^2\theta c_3))) \end{pmatrix}}{24v^3(p_x v - P\gamma)} \tag{6.12}$$

where the fluid properties (ρ, v, P) are constants evaluated at $x = 0$, γ is the gas adiabatic index, and β and θ are the radiation parameters in (6.1).

For values of θ less than 1, the ODE becomes singular if integrated towards $T \to 0^+$. On the basis that it is physically unreasonable for the postshock gas to continue radiating below the temperature of the preshock gas, integration is terminated at a user-set constant (nominally 1.05) times the preshock temperature. The factor 1.05 rather than 1 is used due to tiny artificial temperature fluctuations in the cell ahead of the shock front, which artificially destabilize it if the radiation switch-off threshold is exactly equal to the preshock temperature.

The equilibrium integration, in any case, extends only over parameters for which the resulting ordinary differential equation is well posed and amicable to solution by `Matlab`'s builtin solvers such as `ode113()`.

Once the initial condition for the simulation has been generated, the nonlinear code uses operator splitting to evaluate the transport and radiation terms separately, and so the radiation is evaluated numerically with density a fixed quantity so that it is only necessary to solve an equation of the form

$$\dot{P} = -k\Theta(T - 1.05)\rho^{2-\theta}P^{\theta} \tag{6.13}$$

with $k = \beta(\gamma - 1)(k_b/\mu)^{\theta-1}$, which solution is implemented in closed form for all values of theta (and applicable temperature floor cutoff applied). Numerically, it is favorable to solve the temperature evolution equation instead,

$$T^{-\theta}\dot{T} = -k\Theta(T - 1.05)\rho \tag{6.14}$$

because while this requires an additional division to find $T = P/\rho$ but avoids solving a transcendental function to find $\rho^{2-\theta}$.

Depending upon the radiation exponent θ there are three possible solutions to the temperature curve:

$$\theta = 0 \rightarrow T(t) = T_0 - k\rho t \tag{6.15}$$

$$\theta = 1 \rightarrow T(t) = T_0 exp(-k\rho t) \tag{6.16}$$

$$\text{else} \rightarrow T(t) = (T_0^{1-\theta} + (\theta - 1)k\rho t)^{\frac{1}{1-\theta}} \tag{6.17}$$

In each case, the evaluation of radiation loss is followed by $T = \max(T, 1.05)$ which represents the step cutoff.

Oscillatory behaviors. A radiating column between a dense cold layer and a thin shock front behaves as a one dimensional acoustic resonator. The dense layer behaves as a hard boundary and the shock front as a free boundary. This
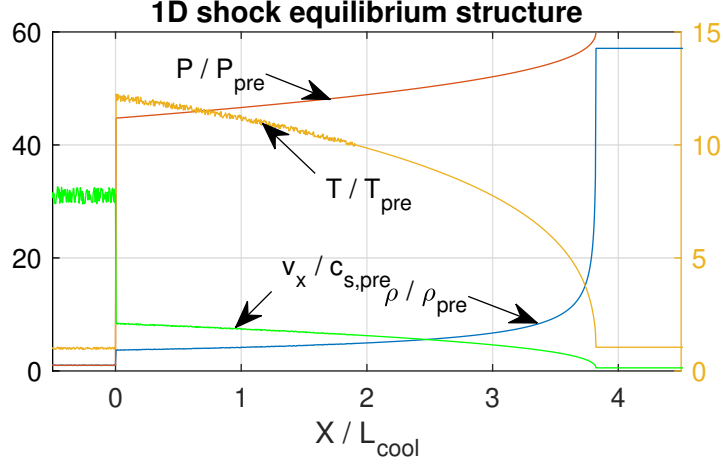
Figure 41. Plot of a 1D equilibrium shock structure with parameters $M = 6$, $\gamma = 5/3, \theta = 0.15$, with all values normalized by the indicated preshock (X_{pre}) values. The visible fluctuations in v (green) and P (red) are the initial perturbations used to salt any instability. This structure is qualitatively the same for all shocks studied.

condition leads us to expect a oscillations at wavelengths which satisfy the half-closed-pipe boundary conditions, namely a fundamental mode with a wavelength $\lambda_0 = 4X_{\mathrm{shock}}$ and overtones at odd harmonics $\lambda_n = \lambda_0/(2N + 1)$. In turn the fundamental mode would oscillate at a frequency ω_0 and the harmonics at $\omega_n = (2N + 1)\omega_0$.

The instability of radiative shocks is of the overstability type. If a shock in equilibrium has its shock front velocity perturbed, the hypothetical new equilibrium shock length is determined instantly by the velocity of the perturbation. The question then becomes, in the time before the cooling column can provide feedback, does the shock pass the new equilibrium or not? If it does, the feedback will say to reverse direction and the shock will be stable. If it has not, the shock will "realize" that it is even further out of equilibrium and runaway instability results.

If we consider a strong shock, the RH jump relations yield postshock quantities (no subscripts) of

$$\rho = \frac{\gamma + 1}{\gamma - 1}\rho_{pre} \tag{6.18}$$

$$v = \frac{\gamma - 1}{\gamma + 1}v_{pre} \tag{6.19}$$

$$P = \rho v^2 \quad T = v^2 \tag{6.20}$$

The results for temperature and pressure are surprisingly independent of the adiabatic index. From these we may calculate the cooling time and cooling length (where $\epsilon = P/(\gamma - 1)$ is the internal energy density):

$$t_{cool} = \epsilon/\dot{\epsilon} = \rho v^2/(\gamma - 1)/(\rho^2 v^{2\theta}) \tag{6.21}$$

$$X_{shock} = vt_{cool} = v^{3-2\theta}\rho^{-1}/(\gamma - 1) \tag{6.22}$$

From the qualitative argument presented above, consider that the shock front is perturbed outward at a velocity w. This will alter the equilibrium column height by an amount $\partial X_{shock}/partialv \times w$. In turn we expect the shock to cover a distance of $wT_{feedback}$ before it "figures out" where it is relative to the equilibrium it is hunting, so an approximate physical intuition for stability is implied by

$$\frac{\partial X_{shock}}{\partial w}w > NT_{cool}w \tag{6.23}$$

in which the feedback time is a dimensionless constant N times the cooling time. The way to read this is, the displacement of the equilibrium position caused by a velocity w exceeds the distance the shock front moves before pressure feedback occurs. Dividing both sides by w and substituting the strong-shock results for the

postshock variables,

$$(\theta - 2)(v/v_{pre})T_{cool} + (3 - \theta)\frac{\gamma - 1}{\gamma + 1}T_{cool} + 2(1 - \theta)\frac{\gamma - 1}{\gamma + 1}T_{cool} > NT_{cool} \quad (6.24)$$

$$(\theta - 2 + 3 - \theta + 2 - 2\theta)\frac{\gamma - 1}{\gamma + 1} > N \quad (6.25)$$

$$(-2\theta + 3) > C N \quad (6.26)$$

$$2\theta < 3 - C N \rightarrow \theta < 1.5 - .5C N/2 \quad (6.27)$$

Where C is the compression ratio of the shock $(\gamma + 1)/(\gamma - 1)$ and N is the unknown constant. In the forward direction, any (positive) value of N indicates that there is an upper bound θ_{crit} above which instability is not expected. Going the other way, the observed threshold values for θ_{crit} imply numeric values of N. Based on the apparent stability thresholds found numerically, at $M = 10$, the approximate numeric values for N corresponding to them are

$$
\begin{array}{|c|c|c|}
\hline
\gamma & \theta_{crit} & N_{eff} \\
\hline
5/3 & .75 & 0.375 \\
\hline
7/5 & .6 & 0.3 \\
\hline
9/7 & .25 & 0.3125 \\
\hline
\end{array}
\quad (6.28)
$$

And it can be seen that the computed numeric value of N is surprisingly consistent across significantly varying adiabatic indices.

Comparison with other nonlinear simulations and linear theory.

In Strickland and Blondin (1995), Strickland & Blondin provide a table comparing their numeric oscillation frequencies at 3 different Machs, two of which are below as SB. Chevalier & Imamura provide frequencies and growth rates from linear analysis in Chevalier and Imamura (1982) (CI below) in the strong shock limit, and our results are presented side by side as KI. These results are for

$\gamma = 5/3$:

θ	$M = 5, SB$	$M = 5, KI$	$M = 10, SB$	$M = 10, KI$	$CI\#1$	$CI\#2$
-1		$.2586(F)$		$.2679(F)$	$.263(F)$	$.953(1O)$
0	$.993(1O)$	$.9588(1O)$	$.869$	$.8701(1O)$	$.294(F)$	$.921(1O)$
$.25$	$1.73(2O)$	$1.018(1O)$	$.888(1O)$	$.8806(1O)$		
$.5$		$2.342(3O)$	$1.43(2O)$	$.8957(1O)$	$.889(1O)$	$1.504(2O)$

$$(6.29)$$

While there are disagreements as to which mode dominates the nonlinear saturation, agreement in mode frequencies is always very close. In cases of disagreement, our mode plots reveal that the parameters in question are usually near to a mode transition; Such cases are generally characterized by very long settling times. For example, for M=5, θ=0.25 we find a 1O mode where Strickland & Blondin find a 2O. Our mode plot finds that this parameter is near the 1O/2O threshold, and the nearby 2O mode at M=4.5, θ=0.25 has a frequency of 1.734, while M=5, θ=0.35 has a frequency of 1.706 (which is the frequency SB found for their 2O mode). In limited refinement tests, we often found that higher resolutions tended to shift the preferred oscillation modes up near mode thresholds by reducing artificial damping of the higher mode.

The nonlinear simulations in all cases are of course disadvantaged in that they can only "report" the dominant mode. In some of these cases, a simulation required hundreds of oscillation periods to settle into the modes we report. Sometimes a shock would settle into a high mode of oscillation, or a mixture of two modes, for many dozens of oscillation cycles before "decaying" into a lower mode. It is worth noting, this process exclusively proceeded one way - never did a shock long reside in a lower mode before eventually entering a higher mode

number. The reason for this exclusivity is that the process we to salt the shocks, a random upstream density perturbation, is heavily biased towards high frequencies such that every simulation begins with high modes and 'tumbles down' the ladder of mode numbers.

Generic mode properties. As suggested at the start of VI and described in detail below in VI, we expect any given shock to have a spectrum of frequencies at $\omega_n = (2n+1)\omega_0$.

Later analysis shows that, with the addition of a correction term for finite Mach, accurate predictions of ω_0 can be obtained for a great range of parameters.

As the 1D PDE has continuously infinitely many variables and the Euler equations are strictly hyperbolic (implying that the system has a complete set of eigenvalues), there must exist infinitely many possible modes of oscillation. As to whether an infinite number of *unstable* modes of ever higher mode number will be found as parameters are swept towards stability is another matter. While there are no longer infinitely many modes once the calculation is discretized, the rapid reduction of mode amplitudes at high mode numbers suggests that these very high modes do not matter anyway.

As described before in VI, high overtones obey the harmonic oscillator prediction very closely, while low modes deviate. This is to be expected based on the large amplitudes that low modes are able to reach, leading to self frequency modulation. The F mode frequency is generally about 15-20% below ω_0 and the 1O frequency is perhaps typically 5% lower than $3\omega_0$, with all higher modes being easily within the standard deviation of their scatter across various parameters of it.

The Nth mode in a half-closed 1D acoustic oscillator has N nodes inside its envelope. Stable, saturated oscillation of a radiating shock in the Nth overtone - or

$$
\begin{array}{|c|c|c|c|c|}
\hline
\gamma & F & 1O & 2O & 3O \\
\hline
5/3 & 0.75; -15\% & .15; -5\% & .04; \approx 0; & .02; \approx 0 \\
7/5 & ? & .12, -8\% & .025; \approx 0 & .015; \approx 0 \\
9/7 & ? & .12, & .023; \approx 0 & .015 - .02; \approx 0 \\
\hline
\end{array}
\tag{6.30}
$$

Figure 42. Table of typical approximate saturated mode amplitudes along with measured typical frequency shifts from prediction for the lower modes at 3 adiabatic indices

the F mode when N=0 - is characterized by (N+1) wave envelopes whose relative phases are $360n/(N+1)$ degrees for $n \in (0, 1, ..., N-1)$: The F mode has a single wave, the 1O has the appearance of two waves 180 degrees apart, the 2O of three waves at 120 degrees, etc. Examples of the first six modes are plotted in figure 43.

Based on this various geometric observations can be made based on the 1/N shift symmetry. A line drawn at fixed time from the adiabatic shock through the cooling region will cross N weak shocks existing inside the cooling region which are analogous to the N nodes of a linear wave. And, a shock propagating down crosses N shocks propagating up. Etc.

The result uniformly holds that an increase in Mach or a reduction in θ will tend to induce instability if it is not present, and lead to a preference for lower modes of oscillation if instability is present.

While low modes dominate over large areas of parameter space, all higher oscillation modes tend to be compressed into relatively narrow bands between the 1O mode and the threshold of discernable instability, with higher modes appearing to occupy progressively narrower bands.

Most parameters, once fully saturated, settle into a mode of oscillation with only that mode frequency and its harmonics present. In the proximity of a mode transition, the time required to saturate and for the weaker mode to ring

145
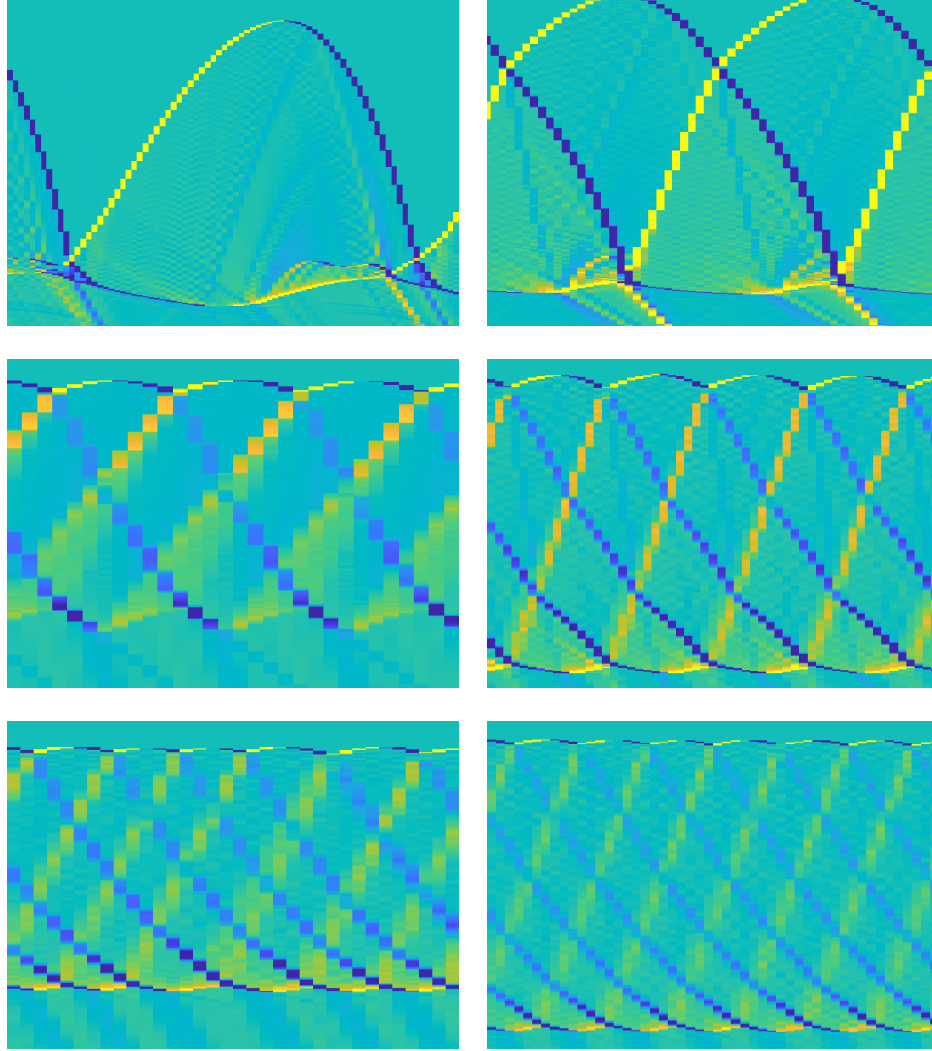
Figure 43. Spacetime waterfall plots (vertical = space, time = to right) of the structure of representative members of the F through 5O modes of oscillation of radiating shocks, showing the increasing number of overlapping wave patterns. Images are of $c_s \propto T$ in linear scale. Representing the input parameters as the tuple (M, θ, γ), the parameters are as follows: F mode - $(6, -.35, 5/3)$, 1O mode - $(7, -.75, 9/7)$, 2O mode - $(2, -.95, 5/3)$, 3O mode - $(8, .25, 7/5)$, 4O mode - $(4.25, .35, 5/3)$, 5O mode - $(5.5, .2, 7/5)$. Overlaid lines are $\partial_t \rho$, revealing shocks moving up and down the cooling region.

down become much longer. Sufficiently near to the transition, it is often the case that the weaker mode does not ring down to zero amplitude, but that both modes coexist with finite amplitude in the final state.

When this occurs, it seems to be the case that only one mode attains true nonlinearity, and the others are present in the spectral analysis only as their linear mode peak. The second mode, rather than creating its own harmonics, instead generates intermodulation tones with the dominant primary mode. This takes the visual appearance in the time series of the dominant mode pattern's peaks appearing to fluctuate periodically.

Even overtones are unstable, but except for high adiabatic indices ($\gamma = 5/3$) and shocks that are weaker than the hypersonic regime they are almost never seen in saturated simulations. It is not clear if a sufficiently fine gradation of parameters might reveal a band of even overtones for lower adiabatic indices or stronger shocks, but the fact that not one was "hit" by chance suggests not.

Shock fallback. All shocks simulated in the equilibrium's rest frame which are unstable are found to retreat downstream at a slow rate once oscillation sets in. This process occurs because the oscillations increase the dissipation of the cooling region, allowing it to reach a temperature which is actually somewhat below the radiation cutoff temperature.

The oscillation process launches both entropic and sound waves into the cold layer. The sound waves are adiabatic, and their compression heats the flow. However, in the cold layer any temperature above the cutoff is "instantly" radiated away, and so the final flow state is such that the *peak* temperature of the waves in the cold layer is close to the cutoff, not its average.

In the normalized preshock flow $c_s = \sqrt{\gamma} \approx 1$ and the incoming flow velocity is $Mc_s \approx M$. The rate at which shocks retreat downstream relative to their equilibrium state is very much less than 1. It is very small for weak shocks (which have very little dissipation) and high oscillation modes (which introduce very little), and for strong shocks (for which the equilibrium cold layer is already moving so slowly as to be nearly unable to go any slower), for which cases the typical fall-back rate is 0.005 or less. For intermediate strength shocks (and especially intermediate strength shocks near the F-1O threshold) the rate is larger, from 0.01 to 0.025 or so. The fallback also becomes very markedly weaker for lower adiabatic indices. In all cases, $\delta v/Mc_s << 1$.

Another potential cause of shock migration is purely numerical error, the failure of the simulation to keep a stable and stationary shock fixed in place. In simulations which were found to be stable, the shock would (except for perhaps a few cells' eventual displacement when the initial perturbation rammed the shock front at the start) remain utterly stationary, barely moving a cell or two even if the simulation ran for a hundred cooling times.

If the simulation is run for long enough in the equilibrium rest frame, a fixed grid leads to the shock inevitably walking off the grid. This is compensated for by boosting the frame to track the fallback.

Plots of the fallback rate versus parameters show that it drops to zero at the threshold of instability, smoothly rises to a maximal value, and then tends to decrease moving towards the high-M/low-θ parameters. Along a curve of fixed M this behavior is easy to understand: At low M, approaching stability, the instability is weak and so fallback is weak. At high M, the post-cooling flow is

so dense it can hardly slow down any more and so fallback is also slow, and thus a maximum exists between these cases.

Multi-mode saturation. As convenient as it would be for analytical purposes, there is no rule stating that only one mode is unstable in a radiative shock for given parameters.

The instability exhibited by 1D radiating shocks is of the saturating type which does not fundamentally rearrange the system. This may be expected only because a 1D system lacks the degrees of freedom present in 2D and 3D that permit the usual mechanism of fluid mechanics that nonlinearity brings to mind - turbulence - to exist.

A few experiments were conducted in which two nonlinear oscillators interacted through a symmetric quadratic coupling:

$$\dot{a} = (i\omega + k_a)a - (k_a/a_{sat})a/|a|^3 + \alpha ab \tag{6.31}$$

$$\dot{b} = (i\omega + k_b)b - (k_b/b_{sat})b/|b|^3 + \alpha ab \tag{6.32}$$

If the $i\omega$ and saturation terms are ignored, the Lotka-Volterra equations are recognizable. The extensions cause either mode to be able to evolve independently of the other (precisely as is observed if one mode's growth rate is negative and a single-mode oscillation is observed). It was found that when realistic frequencies and saturation amplitudes were entered for the F and 1O modes, the spectrum of a numeric integration can reproduce lower order spectral features found in the intermodulated parameter region (the two base peaks and their second-order sum/difference tones) but not the higher order terms when appropriate growth rates and interaction strengths were guessed. The possibility of quantitatively recreating the nonlinear behaviors of the shocks with a slightly more complex model is attractive for the potential analytic tractability and savings in simulation
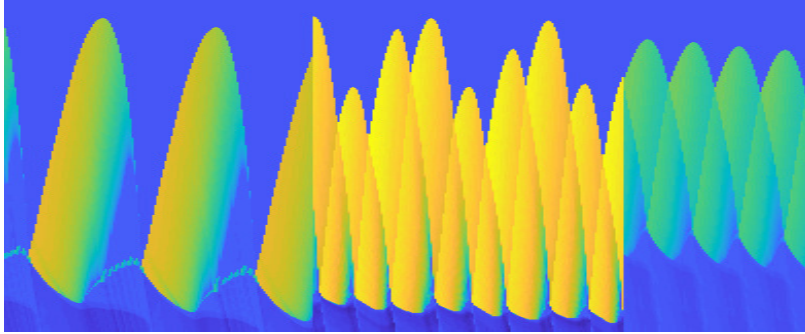
Figure 44. Image qualitatively illustrating the the F to 1O crossover. X-T plot of $\log(T)$ of the radiating regions. Images do not have same space/time scale. All images from simulations with $\gamma = 5/3$. Left: F mode, $M = 5$, $\theta = -1$. Middle: IF mode, $M = 8$, $\theta = -.15$. Right: 1O mode, $M = 4$, $\theta = -.25$.

time, as evaluating (6.31) and (6.32) requires about 5 lines of Matlab code and a few seconds of CPU time, not hours with an entire dedicated fluid code.

Such is potentially relevant to many parameters which, upon simulation start, enter a long period in which they are "trapped" in an intermodulated state with very slow amplitude evolution, until they cross a tipping point where abruptly one mode "wins" and very suddenly. Others, right on top of mode transitions, appear to enter a stable and permanent intermodulation that never decays purely to one mode or another. Such would indicate a third nonlinear fixed point where both amplitudes are nonzero.

Originally, analysis and mode categorization was done manually and led to the supposition that only one or perhaps two modes might be unstable at any given parameter, and that the only major intermodulation occurred between the F and 1O modes, as they are the only ones to reach very large amplitudes.

Improved (and, more importantly, unbiased) automated analysis has found that in many cases - especially for modes of oscillation higher than the 1O - multiple modes of oscillation are routinely detectable in saturated states.
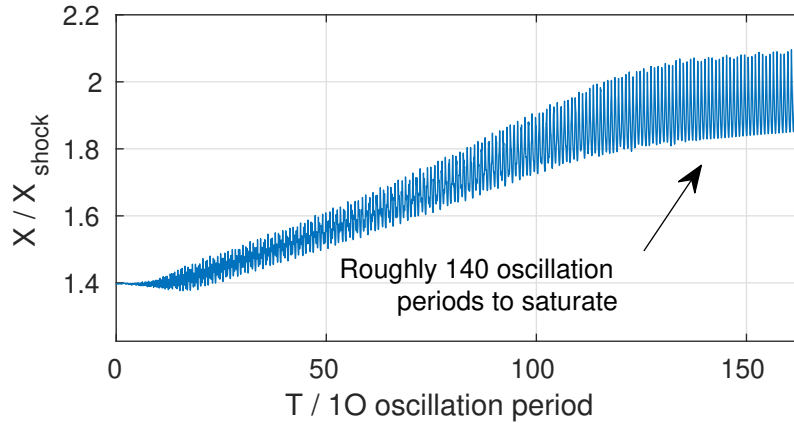
Figure 45. Image of the shock position for run parameters M=6.75, $\theta = -.35$, $\gamma = 9/7$ with a spatial resolution of 4096 cells. These parameters are very near the 1st to 3rd overtone transition, and this run takes over 150 oscillation cycles to reach a clean 1st overtone state.

Typically, any case lying near a mode-dominance transition will exhibit both modes present at appreciable amplitude, with the ultimate power spectral distribution smoothly shifting between them as the parameters are shifted to favor one or the other, as is illustrated in 44 for the crossover between the 1O and F modes. Both possible outcomes, that of coexistence of both modes with finite amplitudes as $t \to \infty$ and that of one amplitude vanishing, are observed. Moving away from the threshold, the outcome is (eventually) monochromatic as shown in figure 45, while in a small region near it both modes maintain finite amplitude, forming a non-repeating pattern (as their frequency ratios are not integer).

For parameters only susceptible to higher (2nd overtone and up) modes of oscillation, the time for saturation and the emergence of the final wave pattern can become extremely long. The final amplitudes are set by nonlinear limiting, and the weak growth rates and low saturation amplitudes of high modes imply very weak nonlinearity (as it must scale as the square of the amplitude or worse).

Remarkably, despite that the complex structures formed by radiatively unstable shocks consist of weak internal shocks crossing back and forth across the cooling region rather than any sort of linear wave-like oscillation, the simple acoustic-resonator prediction for mode frequencies (and the predictions based a linearized strong shock) both remain remarkably close to each other and the results of nonlinear simulations as found here and elsewhere.

Radiation cutoff problem. The radation cutoff formula described for the equilibrium generation works fine for the case in which radiation is in some sense "weak." However a resolution problem tends to arise at the base of strong shocks. This is because the postshock density of a strong isothermal shock (which state of the cold layer approaches) increases as M^2, and so radiation rate increases as $\rho^2 \propto M^4$. Thus is quickly becomes extremely difficult to truly resolve the cold dense base of high-M shocks, where the cooling rate increases so quickly that the majority of all density increase occurs within literally a handful of cells.

Realistically, this becomes a problem when $dx \times \partial_x \rho$ becomes comparable to ρ itself, i.e. the radiation calculation based on piecewise constant cells breaks down. Normally this algorithm is actually quite accurate: The second order correction is the gradient in radiation rate, but this cancels by symmetry so that the simple piecewise-constant method is actually 2nd order accurate.

In one dimension, this case in which there is sub-cell structure can be handled by identifying and tracking this cell for special treatment. However, much as Lagrangian grid transport is trivial in 1D but not in any higher dimension, this proposition quickly becomes untenable in multiple dimensions and/or with nontrivial flow geometry.

In this work, for 1D, the resolution problem was handled by simply increasing the resolution. The resolution required was highest with high-M shocks. It was also found to be higher for more negative values of θ, in particular for $\theta < 0$ for which the radiation rate becomes singular as $T \to 0$. It was also seen that more resolution was needed for shocks with higher adiabatic index (5/3). In the most difficult case surveyed - $M = 10$, $\gamma = 5/3$, $\theta = -1$, a total resolution as high as 32768 cells was used, and even then the solution exhibits marginal behaviors (even if the F mode pattern frequency is correct).

It should be noted that identifying the frequency spectrum peaks associated with modes is relatively easy to do reliably, especially given foreknowledge of what their frequencies are likely to be as is available for the 1D shock problem. Moreover, there is no requirement to reach a saturated state - the mere presence of the peak in the Fourier transform is sufficient.

However, comparable accuracy and reliability for mode *amplitudes* is more difficult to achieve as now the simulation is in fact required to reach the saturated state. This can potentially require a very large number of iterations to approach, and even then a mode that appears to have settled in may relatively abruptly undergo mode decay and be replaced by a new lower frequency oscillation pattern. This kind of changeover may take a hundred cycles for the new mode to slowly grow in amplitude, before abruptly jumping to 100% of all oscillation power in a relatively short time.

Accurate prediction of integrated luminosity fluctuations is made even more difficult because the above requirement for full saturation is compounded by relative difficulty in actually measuring the radiation rate in certain circumstances. Those circumstances are namely strong shocks with runaway cooling ($\theta < 0$). In

these cases, the radiation rate peaks so strongly at the very base of the shock that nearly complete cooling occurs when radiative loss is applied to the flow.

Because GPU-Imogen code solves the flow using operator splitting, either the saved full-timestep data will have just had flux transport applied (in which case it will be hot and the radiation rate, evaluated at this point in time, will be too high) or just had radiative loss applied (in which case it will be cold and the radiation rate measured at this point in time will be depressed). In fact, for strong shocks with runaway cooling, the base cells will cool completely during the radiation phases, so the measured radiation rate at the end of a timestep for those cells will be depressed all the way to zero. That this is the phenomenon occurring and not an error in flow calculation is supported by the observation that where this phenomenon's prevalence is worst - $\gamma = 5/3$ shocks with $M > \approx 5$ and $\theta \leq -.5$ - there are many simulations which reproduce consistent shock position amplitudes even as dramatic drops in measured integrated radiation rate occur. It is difficult to see how an error in simulation could cause one but not the other.

Backreflection of emitted waves at low θ. It is observed under conditions of low θ (meaning -0.5 or lower usually) that the shock quantities exhibit oscillations at frequencies lower than any cooling region mode. These appear to be due to the very large amplitude sound and entropy waves that the shock bouncing emits into the cold layer at low-θ parameters. The sound waves immediately steepen into weak shocks, and these reflect off of both the outbound train of entropy waves as they overtake them and off of the the downstream static boundary. The former case is entirely physical within the context of the simulation (if not within the context of being a reasonable downstream boundary for most physical systems). The latter, problematically, couples the cooling region acoustic

154

oscillator to an artificial one created by the cold layer boundary and the simulation grid boundary.

The best realistic solution to this seems to be to use a large cold layer, which makes the frequency of the second fake acoustic oscillator very low, such that the resulting sidebands in spectral analysis don't overlap with (predicted) real mode frequencies and impersonate them.

This problem only seriously afflicts low-θ simulations because the intensity of the sound waves launched grows when θ is low. As the downstream end boundary is static, the reflection coefficient of incoming sound waves is proportional to the square of their amplitude (the incoming amplitude brings one power of a, while the deviation from the equilibrium condition due to a brings the second). At low θ values, the outbound sound wave amplitudes have been seen to reach 30% or more, leading to reflection coefficients which can be on the order of 10%.

Analysis methodology.

Parameter refinement. A total of roughly 1000 simulations were run spanning the region $2 \leq M \leq 10$ and $-1 \leq \theta \leq 0.5$ for adiabatic indices of 5/3, 7/5, and 9/7. Initial parameter searches used relatively widely spaced $(\Delta M = 1, \Delta \theta = .25)$ gridded points. Parameter spacing near mode transitions was progressively refined to values of $\Delta M = .25$ and $\Delta \theta = .05$. When referring to changes in outcome depending on parameters, this will be referred to as "a square" below since this parameter spacing gives the appearance of a roughly square grid when plotted over the range of parameters surveyed. In total, the 1D simulations compose roughly 1TB of X-T data.

A region in which a mode dominates may be considered "cleanly resolved" in the scanned parameter space if squares with all four points dominated by the same mode are found. This is because there do not appear to be any "surprise" structures, such as islands of different modes, so that a square whose four points are all the same mode is taken as indicating that that mode dominates the entire inside of the square, and that extrapolation is from nearby points is valid.

The finest grid spacing was found to be enough to cleanly resolve the lower oscillation modes, but the regions dominated by modes higher than the 3rd overtone are generally comparable to, or narrower than, the spacing and are thus not resolved as plateaus in mode plots. The grid was not further refined as the separation between modes becomes so narrow that the time required to acheive consistent results becomes excessive.

Limits of simulation. Numerically, the very high modes become exceedingly difficult to resolve. To begin with, it is a case of detecting an ϵ perturbation on an O(1) equilibrium, so that the features being measured become hard to compute or see. As the oscillation becomes weaker, so do the shocks running up and down the cooling region. While even a Mach 2 or 1.1 shock is resolved in a handful of cells, this is not the case for a M=1.01 or M=1.001 shock; The self-steepening behavior that makes shock resolution possible depends on the self-steepening behavior of shocks, and this scales as the third power of $(M - 1)$, so that enormous numeric resolutions are required to prevent numeric dissipation from interfering. Because the growth rates are tiny, the simulation must also be run for a very long time. And to top it off, because the pattern frequencies are so high, the Nyquist sampling criteria requires saving a larger fraction of an enormous number of timesteps.

While it is not an answer, we submit that in truth the answer is unlikely to realistically matter. Of the 1000+ simulations run, perhaps a few dozen could be reliably characterized as exhibiting oscillation modes of 7th overtone or higher. The amplitude of these oscillations is always extremely small: The shock position is typically modulated by 0.5% or less, and the column integrated luminosity fluctuation is at most a few percent. Such a modulation depth of the emitted light as a function of time is tiny, and because the mode is subject to such rapid change if the shock parameters change even slightly, the very idea of a saturated mode may not realistically apply at all.

A default space resolution of 4096 cells was eventually settled on, with roughly 1000 to 1500 cells resolving the cooling layer, about 500 cells upstream to accomodate potential shock front oscillation (and/or slow upstream migration) and the balance in the cold layer. At shock strengths beyond Mach 6 and especially with runaway ($\theta < 0$) cooling, the resolution is scaled up to accomodate the increasing resolution requirement for resolving the base of the shock.

Denoting the radiation operation as R and flow as F, the propagator sequence $(R/2)(F/2)R(F/2)(R/2)$ is used to advance the simulation through one δt with second order accuracy in the Strang splitting. Because the timestep limitation is a nonlinear function of the state that must be recomputed every step when we have second time-order accuracy, adjoining $(R/2)(R/2)$ steps unfortunately cannot be computed at once in the way that they are in e.g. the Verlet method for the N-body equations because the timestep must be recomputed between them.

Both the upstream and downstream boundary conditions are static, equal to the incoming uniform flow and outgoing equilibrium cold layer states

respectively. At the downstream boundary, this causes sound waves to reflect with amplitude proportional to outbound amplitude squared. Normally the outbound amplitude is small enough (perhaps 10%) that reflection is minimal. In the case of strongly runaway radiation laws ($\theta <\approx -0.5$) the outbound sound wave amplitudes become large enough (up to perhaps 30%) to result in measurable reflections which cause a degree of "jitter" in some simulations.

In such simulations it is useful to utilize a large buffer zone. This is because lower boundary reflections effectively couple the desired cooling region oscillation to a second acoustic cavity formed by the cold layer boundary and the end of the grid. By making the buffer zone long, the resonant frequency of this cavity can be made quite low. As a result, the spectral side-bands at $\omega_{\text{shock}} \pm N\omega_{\text{cav}}$ can be kept near to ω_{shock} so they are not confused with real modes.

Simulations are run until a stable mode pattern emerges. The time required for this pattern to emerge depends on the physical instability level, with weakly unstable high modes requiring longer, as well as the proximity to mode transitions. For highly unstable modes as little as one to two dozen oscillation periods is often enough for the final wave pattern to settle in, after which it is typically run for a minimum of several dozen cycles in order to get a narrowly peaked spectrum graph. For less unstable simulations, or especially those very near to mode transition boundaries, runs may be extended for multiple hundreds of oscillation periods. In numeric terms, this typically equates to a minimum of half a million time steps, to in some cases involving weakly unstable strong shocks nearly ten million iterations.

Analysis process. Analysis of the simulations has been facilitated by the development of an almost automatic analysis routine in the form of the
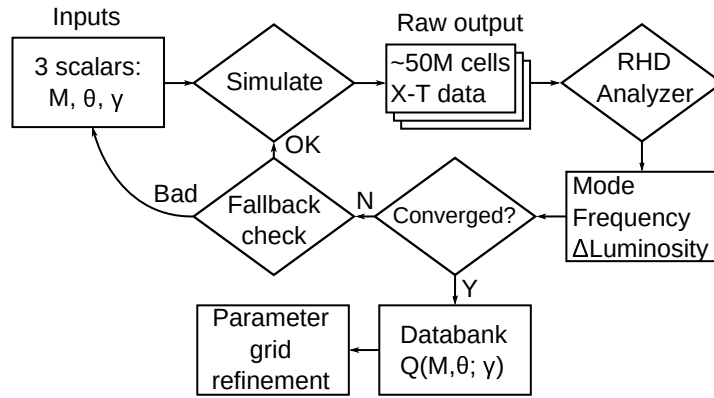
Figure 46. Flowchart depicting the input, generation and data-reduction phases of the 1D simulation bank

RHD_Analyzer class. At the end of a simulation, the analysis of the resulting

X-T dataset begins with the waterfall diagram, a typical well-behaved species

representative of which is shown in Figure 47.

The researcher is asked to identify the wave round-trip time; In the case

of a monochromatic mode, the number of peaks inside this interval is the mode

number (1 = F, 2 = 1O, etc). The tool then requests the interval to be Fourier

transformed, and tries to shift the endpoints to the nearest minima in order to

try and minimise broadening of the spectral peaks and other spectral spurs. The

tool will then tag the 10 largest spectral peaks and use a priori knowledge of what

frequencies various modes are found at in order to label those associated with

oscillation modes.

Most of this user input is only required once, as the analyzer stores the

manual-input data for future reference. If the simulation is resumed and run for a

longer time, the only manual intervention required is the new transform interval. If

reanalysis is desired after a change to the tool, all runs which have been
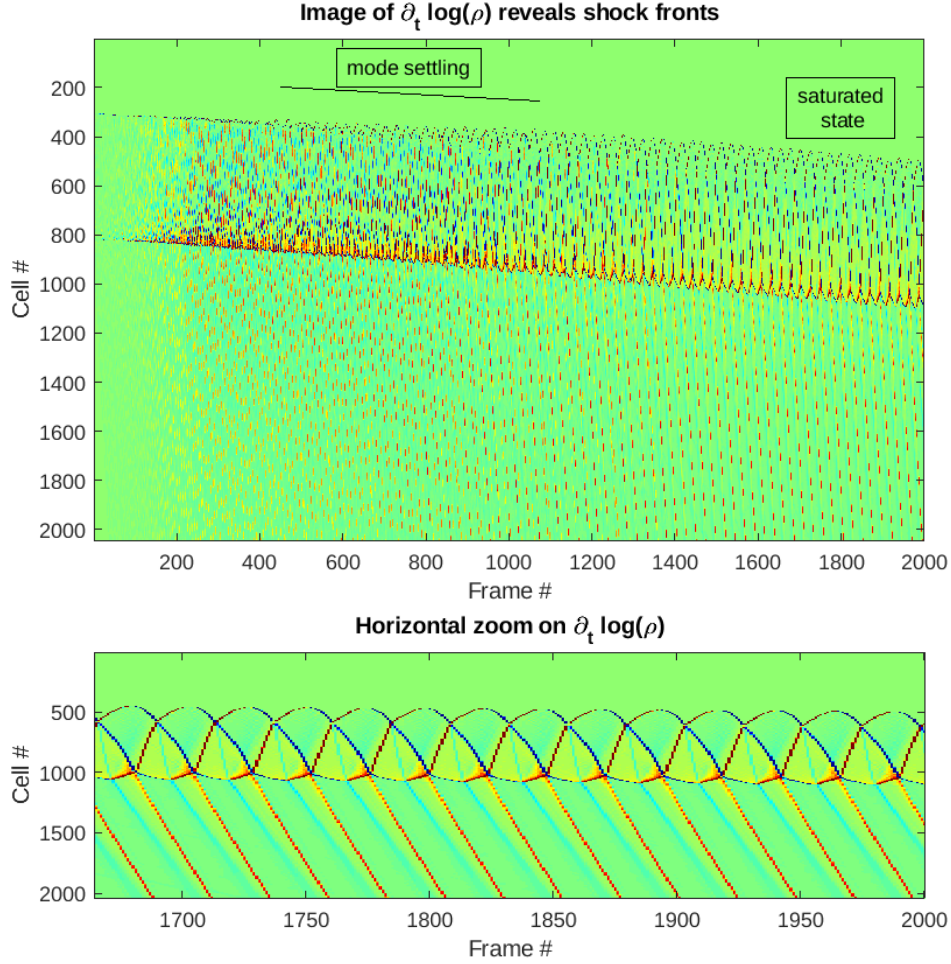
Figure 47. The first image shown by the RHD analysis workflow is $\partial_t \log(\rho)$. This reveals shock fronts, sound waves and entropic waves. These images are taken from a simulation with $M = 6.5$, $\theta = 0.25$ at $\gamma = 7/5$; If the eye is let to follow a line from the base (bottom) of the shock, up over and back down to the base, it can be seen that the spatial pattern repeats twice in this period and so this is a first overtone (1O) mode. This simulation took 40 oscillation periods to settle and ran for a total of 90.

previously analyzed can be automatically re-scanned.

The normalization with the time unit of x_{shock}/v_{in} yields normalized frequencies that are relatively close to constant for a given mode across a very wide range of parameters (Eq. (6.33)), but exhibit clear and predictable trends. A

160

small linear correction for the dependence of ω on θ exists, which from the values given can be seen to be only a handful of percent. The first term in a Laurent series in Mach, the correction proportional to $1/M$, is the real mover,

$$\hat{\omega} = \omega_{meas} * x_{shock}/v_{pre} \tag{6.33}$$

$$\hat{\omega} = \omega_{meas}\frac{x_{shock}}{v_{pre}} \times [(1 + a(\gamma)/M) \times (1 - b(\gamma)\theta)]^{-1} \tag{6.34}$$

$$\omega(n) \approx (2n + 1)\hat{\omega}_0 \tag{6.35}$$

where $(a, b)(5/3) = (1.75, .038)$, $(a, b)(7/5) = (2.5, .042)$ and $(a, b)(9/7) = (2.84, .06)$. This is the above referenced a priori knowledge. Based on this normalization, mode frequencies are predicted and spectral peaks tagged based on (6.35) below, using $\omega_0(\gamma = 5/3) = 0.256$, $\omega_0(\gamma = 7/5) = 0.186$ and $\omega_0(\gamma = 9/7) = .150$.

The correction to frequencies grows larger and larger at low Machs. Because shocks with $\gamma = 5/3$ can be unstable to very low Machs (as low as $M = 1.75$, though the radiation model is all but certainly unphysical at such parameters), the first correction for finite M in (6.35) may not be sufficient. An alternative formula obtained by numerical least squares is

$$\hat{\omega} = \omega_{meas} \left[\frac{v_{pre}}{x_{shock}} \times (1 + 1.14/M + 1.45/M^2) \times (1 - .02\theta)\right]^{-1} \tag{6.36}$$

and $\omega_0 = .261$; This formula yields accurate a priori frequency predictions for shock strengths as low as Mach 2. Examination of the residual left at this point indicates a very complex structure that would likely not be amenable to significant further improvement by this method. Moreover, the "structure" is comparable in amplitude to the random scatter in measured frequencies, meaning that a great deal of data curating work and extended simulations to narrow the Fourier peaks would be required to proceed.

Both complex normalizations, eq. 6.35 and 6.36, are extracted from empirical fits. Presumably, a linear prediction would be possible if linear analysis were applied to a shock calculated using the exact hydrodynamic jump conditions, or if they themselves were computed in a Laurent series in $1/M$.

This complex normalization is very useful for analysis purposes, but would cause all presented values to deviate from those computed using the normal formula $\hat{\omega} = \omega_{meas}/\frac{v_{pre}}{x_{shock}}$, so the normal formula is used for all presentations.

In the perfect world imagined by (6.35), mode frequencies would now equal positive odd integers with $\hat{\omega} = (2N+1)\omega_0, N \geq 0$. In fact, low mode frequencies are predictably and repeatably less. This may be expected as low modes are associated with large amplitudes, and a shift $\omega \to \omega_0 + \omega_1 A^2 + ...$ is expected. Thus, the analyzer is programmed to search for low modes at frequencies of $[.86, 2.85, 5, 7, ...]$ based on empirical observation. The deviation in the frequency of the 1O mode is found to be consistent across all 3 adiabatic indices. That of the F mode is assumed to be so, despite that no F modes were found except for $\gamma = 5/3$.

Once peaks have been identified in the FFT, the more difficult task of peak analysis and assigning peaks to modes, harmonics of modes and mode interaction begins. This job is handled by the `SpectralAnalyzer` class in several phases.

First, (6.35) is used to name spectral peaks. The width of the acceptance bin is set to 0.07, which encompasses the entire range of variations in actual frequency versus predicted. Following detection of a mode, its harmonic distortion terms are searched for among all remaining untagged peaks. The criteria for harmonic distortion terms are far more stringent,

$$|\frac{f}{f_0} - \text{round}(\frac{f}{f_0}| < \sigma(f, f_0) \tag{6.37}$$

162

where f is the possible harmonic, f_0 is the base tone and $\sigma(f, f_0)$ is the RMS of the peak fitter's returned Gaussian width for the f and f_0 peaks. Simply put, the peaks must be closer to an integer frequency ratio than the uncertainty in their positions. Harmonic distortion must be marked immediately because odd harmonic distortion creates peaks which land on the $(2N + 1)\omega_0$ ladder and look just like higher overtone peaks. So for example the 3rd harmonic of the 1O mode, which has frequency of roughly $9\omega_0$, would get marked as being the 4th overtone if it were not already marked as being a harmonic.

The second phase is necessitated by the same problem: Odd order intermodulation, like odd order harmonic distortion (of which it is a generalized case), creates frequency peaks which will appear at (nearly) the same locations as actual shock modes. In the case of shocks which oscillate in higher modes, the two effects are nearly impossible to disentangle. Because the shock oscillation modes do not lie *exactly* on an integer frequency ladder, technically a third order term created by two true modes will not have *exactly* the same frequency as an actual third shock mode. But in reality, the second and higher overtones come so close to the ladder that the frequency resolution required to distinguish the two separate peaks is not achieved.

In general it is observed that only rarely are more than two shock modes present at substantial amplitude, and these modes are generally adjacent (e.g. 2O and 3O, 4O and 5O, etc), even though it is nearly always an odd overtone that dominates. If the two tones are denoted A and B, there are four unique ways to

163

make a third order intermodulation:

$$2F_a + F_b : 2(2N + 1) + (2N + 3) = 6N + 5 = (6N + 4) + 1 \rightarrow (3a + 2)\text{overtone} \quad (6.38)$$

$$2F_a - F_b : 2(2N + 1) - (2N + 3) = 2N - 1 = 2(N - 1) + 1 \rightarrow (a - 1)\text{overtone} \quad (6.39)$$

$$2F_b + F_a : 2(2N + 3) + (2N + 1) = 6N + 7 = (6N + 6) + 1 \rightarrow (3b + 3)\text{overtone} \quad (6.40)$$

$$2F_b - F_a : 2(2N + 3) - (2N + 1) = 2N + 5 = 2(N + 2) + 1 \rightarrow (b + 1)\text{overtone} \quad (6.41)$$

The two sum formulae generate very high frequencies and seem to occur very weakly. The difference formulae yield the classic examples of third-order intermodulation distortion: With two carriers separated by a frequency δf, these close-in IMD products occur δf below the lower frequency carrier (the $a - 1$ overtone) and δf above the higher one (the $b + 1$ overtone). A third particular case consists of intermodulation between the Nth and 2Nth overtones,

$$2F_N - F_{2N} : 2(2N + 1) - (4N + 1) \rightarrow 1(= \text{F mode}) \quad (6.42)$$

For the 1st and 2nd overtones, this is equal to the first set of cases but this can also occur with e.g. the 2nd and 4th overtone, or 3rd and 6th. This situation is most often encountered with runs that oscillate at high overtones, and was only considered because early analysis tools falsely indicated that F modes were being detected where no F mode could possibly be. In all cases, the result is a frequency peak at ω_0 which is near enough to the location of the F mode peak at $0.86\omega_0$ that it is often mistaken for it. The fact that the 1O frequency is actually $2.86\omega_0$, placing the fake tone at $2 \times 2.86 - 5 = .72$, is unique in that the fake tone lies below rather than above the actual F mode frequency, but the distance is comparable.

In all of these cases, the fake shock mode is distinguished by two critera: The amplitude of the fake mode, as an intermodulation tone, will be smaller than either of the tones creating it. Second, the frequency of the fake peak will

164

exactly match the sum/difference formula, usually within a small fraction of the FFT frequency resolution. To give an example encounted during development testing, a 2O and 3O mode conspired to create a fake 1O mode differing from the difference formula prediction by only .0025, in an FFT with a resolution of .0097. Meanwhile the acceptance bins for marking modes a priori are .14 wide in the same normalization, meaning that a match a close as .00x is much more likely to be a harmonic product than a new tone.

The particular edge case of a run in which the F mode is much larger than the 1O mode amplitude, but the 1O mode still exists, has in a very few cases been observed to break the perturbative ordering rule (that higher harmonics are always weaker than lower ones) for shock displacement amplitudes: In this rare case the 1O - 2F interaction peak can actually be larger than the 1O peak itself, because the F mode amplitude is in this case very large. This case may result in both the F mode and the (1O-2xF) frequency peak being tagged as "the" F mode. This is rejected by counting the number of single peaks associated with a single mode type. If there is more than one, the largest is kept and others are rejected.

Once a good attempt has been made to identify and reject fake shock mode tones, the intermodulation analysis can be made to assign meaning to the remaining spectral peaks which are not base (shock mode) tones or harmonics of them. In the most general case if there are N identified base tones F_i, it would be necessary to test for every unknown peak f whether

$$|\Sigma\alpha_i F_i - f| < \epsilon, \alpha_i \in \mathbb{Z} \tag{6.43}$$

with a nonlinearity order equal to $\Sigma|\alpha_i|$. In analyzing shocks, given how rare it is to see more than two large-amplitude tones, it is restricted to consider the base frequencies only pairwise (for N(N-1) possible pairs) and values of α are restricted

165

from -3 to 3 inclusive. This is found to identify all, or nearly all, peaks in the considerable majority of simulations.

As with harmonic distortion, the concession to imperfect data lives in ϵ. In this case, ϵ is set to the RMS of the gaussian fit widths of the input F_i and of the f target peak.

The end result of the analysis, as depicted in 46, is a map that gives (mode, oscillation frequency, radiance fluctuation) as functions of (Mach, radiation θ, adiabatic γ) without requiring others to go through the intermediate steps involving 100s of GB of data analysis.

Mode analysis is computed by analyzing the shock front displacement because this represents a measurement that depends on a local value (the position
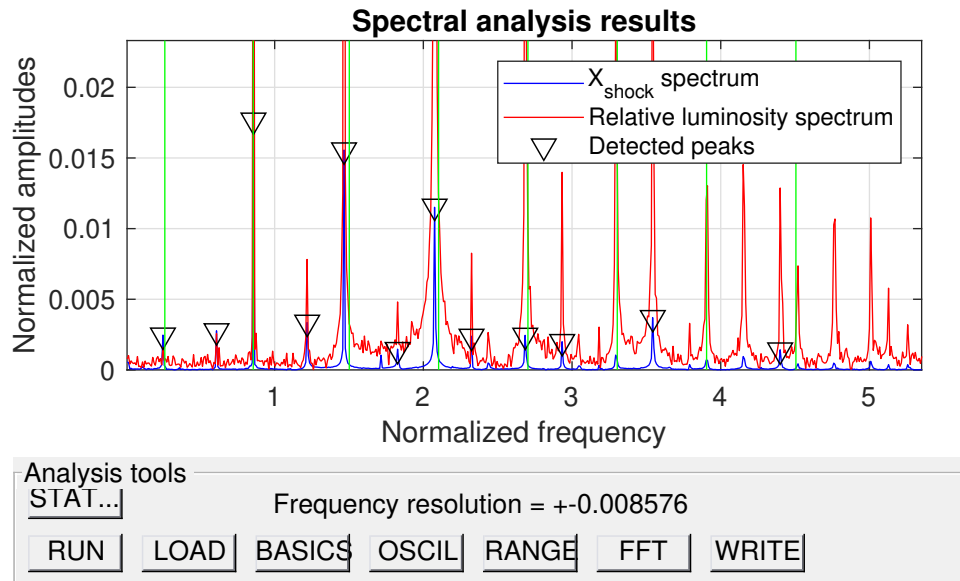

Figure 48. Screenshot of the 1D analyzer's output spectral graph, zoomed in to show the relative noise levels of X_{shock} (blue) and integrated luminosity (blue). This simulation has parameters $M = 4.25$, $\theta = -.4$, $\gamma = 7/5$; The transform was on roughly 2800 points.

of the adiabatic shock jump), and on a variable that is "clean." On the other hand, the astrophysical observable - periodic or quasiperiodic fluctuations in luminosity - is an integral over the cooling region of a viciously nonlinear function, and often has a noise floor an order of magnitude higher than the shock position does, despite the normalized amplitudes typically being rather similar. This situation is shown graphically in 48.

Detailed 1D results. Planar shocks are found to be subject to a variety of radial oscillatory instabilities depending on their strength and the radiation's temperature dependency. The result in terms of dominant mode as a function of Mach and θ is summarized in figure 49.

Interest is particular in the case of $\theta = 0.5$ as it corresponds to bremsstrahlung. For a gas with $\gamma = 5/3$, corresponding to a completely ionized postshock of a compact accretion column, the oscillation of a strong shock will be in the 1st overtone. In the case of a supernova remnant in the radiative phase, the cooling's temperature dependence will take on a wide range of values, including strongly runaway cooling once the postshock temperature is no longer sufficient to destroy all molecules (whereupon further cooling will permit more molecules with more molecular excitations to exist).
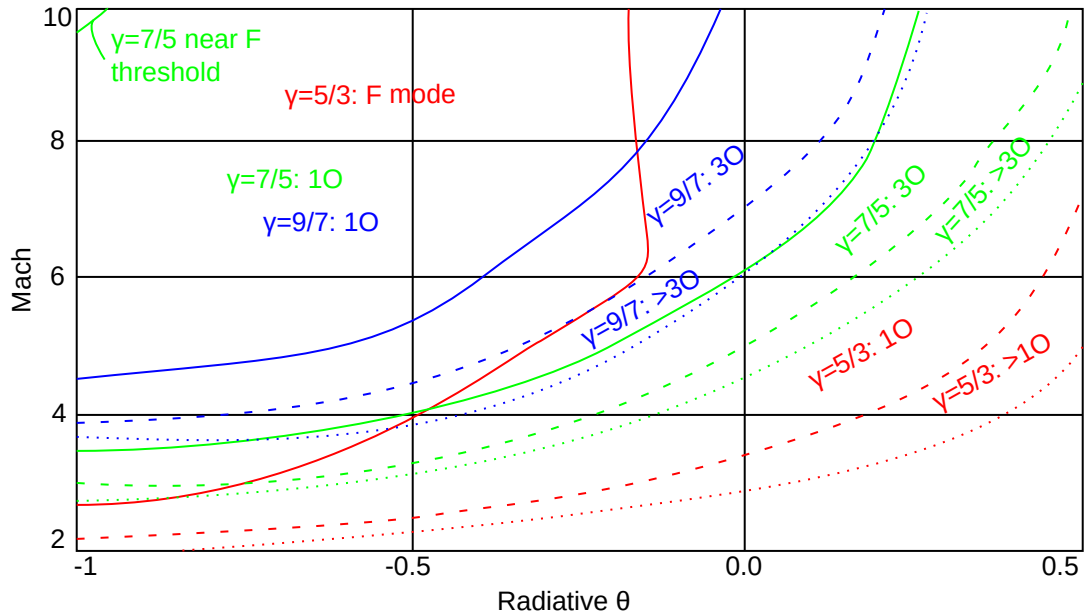
Figure 49. Summary of expected mode type for all three adiabatic indices as a function of cooling parameter θ and shock strength M. Dotted lines denote the threshold of stability, below which no oscillation is observed. Dashed lines denote parameters dominated by higher modes (mode type changing too fast to resolve; For $\gamma = 5/3$, anything above 1O, for $\gamma = 7/5$, anything above 3O, for $\gamma = 9/7$ anything above 5O). Solid lines indicate the threshold of the F mode (for $\gamma = 5/3$) or 1O mode (others) plateaus.

Results for $\gamma = 5/3$**.** At the parameters tested, $\gamma = 5/3$ is the only adiabatic index for which F modes are found to dominate any part of parameter space. The vast bulk of parameters tested in the region $(-1 \le \theta \le 0.5) \times (2 \le M \le 10)$ yielded F or 1O oscillation modes, with higher modes appearing only in a narrow region near the threshold of stability.
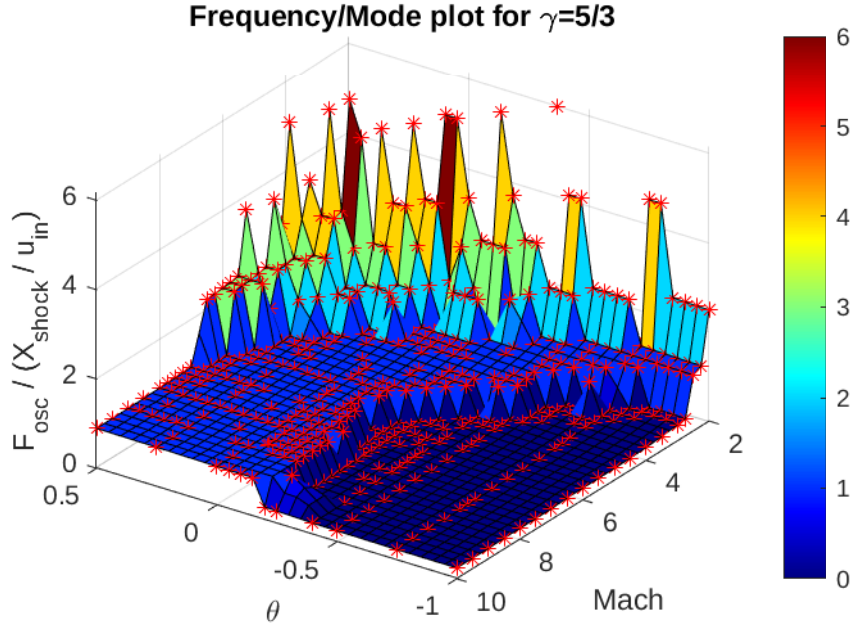
Figure 50. Dominant mode type and frequency plot for $\gamma = 5/3$

Empirical formulae have been found for the parts of parameter space containing F, 1O, and all higher modes. For $\theta <\approx -.2$ and shocks up to $M = 6.5$, it's found that

$$\text{mode}\left[M >\approx 3 + 6(\theta + 1)^2\right] = \text{F} \tag{6.44}$$

and for $M >\approx 6.5$ the line separating F and 1O becomes steep, with the critical θ remaining around -.15 at Mach 10. Similarly, for shocks up to about $M = 5$, the high mode oscillations are confined in a narrow band near to the theshold of instability,

$$\text{mode}\left[2 + .8(\theta + 1)^3 <\approx M <\approx 2.25 + 1.6 * (\theta + 1)^2\right] > \text{1O} \tag{6.45}$$

for θ up to about 0.4. Above $M = 5$ and $\theta = .4$ the slope $dM/d\theta$ of the line between 1O and higher modes becomes fairly large. The critical strength for a $\theta = 0.5$ shock to oscillate in the 1O mode is about $M = 7.5$. This is notable

for meaning that the oscillation mode of a strong $\gamma = 5/3$ shock emitting Bremsstrahlung is firmly within the first-overtone region.

As can be seen in figure 51, the boundary between the F and 1O modes is not exactly the perfectly unambiguous line one would wish it to be. Because the amplitude of the pure F mode is large, so is nonlinear modulation with other modes. As parameters are swept from pure F mode (e.g. $M = 10, \theta = -.5$) to pure 1O mode (e.g. $M = 10, \theta = .5$), there is a large region where both modes are present at large amplitude (the 'incomplete F mode'). Even well into the region where a mode is called '1O' there is generally a detectable spectral peak at slightly under 1/3 the 1O pattern frequency, meaning that the F mode remains weakly unstable well into that regime.

The range of parameters over which the F and 1O modes are both unstable is wide enough that it is actually resolved and the transition from pure F to pure 1O can be readily observed on the grid of computed results. In the regime where they are comparably unstable, a third order intermodulation is observed at $f = f_{1O} - 2f_F$. This leads to the appearance that power "sloshes back and forth" between the two modes at a slow rate. Because the position amplitude is dominated by the F mode, the visual result resembles that of an AM radio waveform.

This regime of competing oscillations may be observed to either end with a repeating envelope pattern at a fixed amplitude, or (as the parameters shift away from the transition) ultimately end with the exponential decay of one component or the other, yielding a pure F or 1O mode. The origin of the envelope lays in the non-integer frequency relation between F and 1O (3xF and 1O differ in frequency by about .3 in normalized units). Thus roughly every 6 F mode cycles, the

170
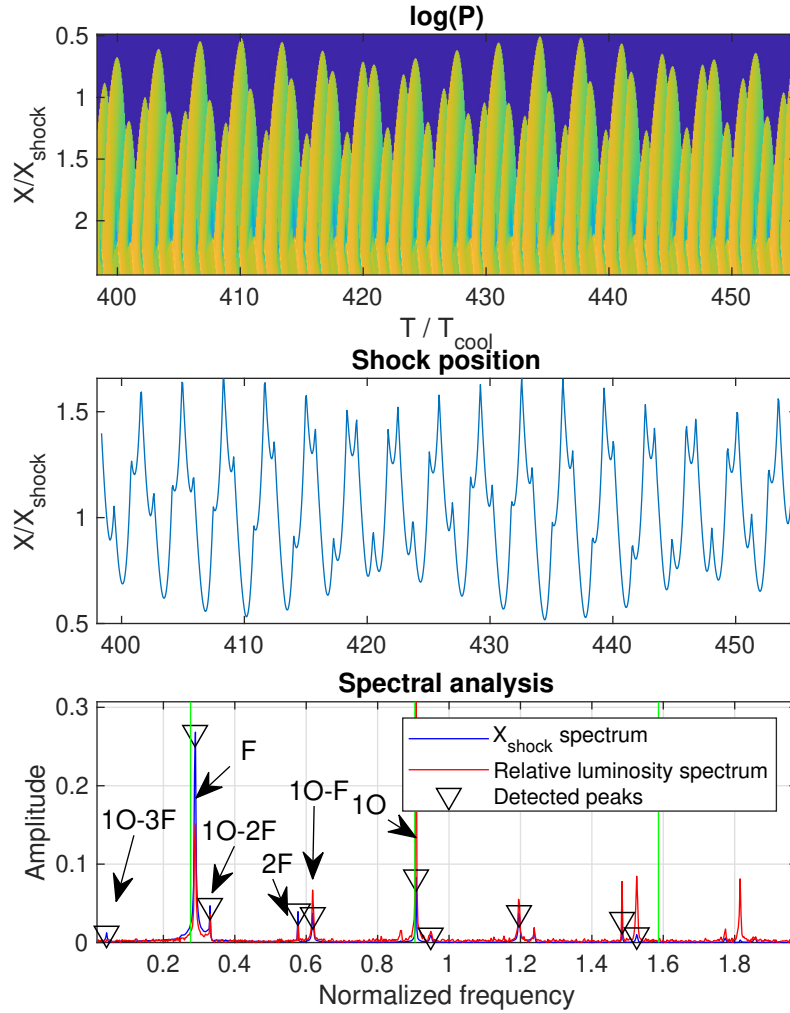
Figure 51. Plot showing one of the F/1O borderland simulations which exhibits intense and complex intermodulation, including long-period amplitude oscillation.

peaks of the 1O mode oscillation go from adding constructively with the F mode (increasing its amplitude) to adding destructively and back, yielding the envelope.

The region occupied by all modes higher than 1O is only a few "squares" (0.25 Mach by .05 θ, the finest resolution of the examined parameter grid) wide in total, and no plateaus of higher modes are resolved.

For the most part, any given mode's luminosity fluctuation has a similar power-ordering as the shock position does when observing harmonic distortion - power is a decreasing function of the harmonic, though for luminosity very much more slowly than with shock position. The F mode is the only reversal, often having considerably more luminance in its 3rd harmonic.

While the mode type changes dramatically over parameters, the luminance fluctuation does not. From a maximum normalized value in the (large M, negative θ) corner of parameters that approaches 100%, it undergoes a remarkably smooth decrease towards zero at the threshold of instability. If only the power in the dominant mode is graphed, the surface exhibits notches at mode transitions; This is because multiple modes tend to share power at transitions, and if the RMS luminance of all mode peaks is graphed instead, the result is quite a bit smoother.

We find it notable that while the mode type, and correspondingly the
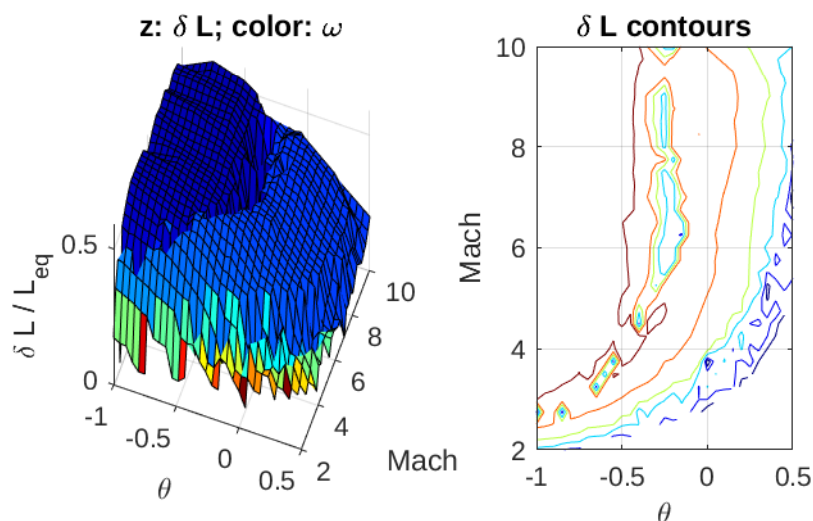
Figure 52. The luminance fluctuation in the dominant mode for $\gamma = 5/3$. Left: 3D surface shows gap where emission fluctuation is spread into intermodulation tones. Right: Contour graph
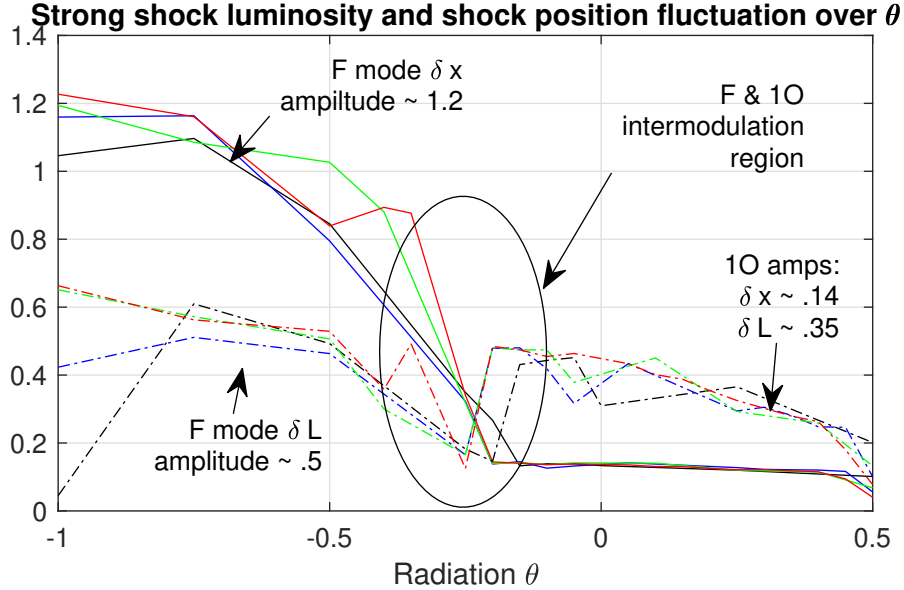
Figure 53. Graph of normalized shock front position (solid) and luminance (dash) fluctuations across θ for M = 10 (black), 9 (blue), 8.5 (green), 8 (red); Some glitches in the luminosity graph reflect the difficulty of obtaining clean data in the high-M regime.

structure of the instability's saturated wave pattern and its frequency, jump considerably over the range of surveyed parameters, the radiance fluctuation overall remains much smoother. For strong shocks, it appears to correlate strongly with the radiative θ, with a small step down in magnitude at the F to 1O transition.

It is fascinating to observe that F modes with strongly runaway cooling (low θ) will often form "baby" radiative shocks inside the F mode envelope with every oscillation cycle. During the outward overshoot phase, the flow length is long enough to acheive complete cooling. Because the flow maintains a speed well above the final cold layer value, this returns it to supersonic speed and forms a second "baby shock." The baby shock appears to oscillate in either the F or 1st

overtone mode, and usually manages somewhere under 10 oscillations before the main envelope implodes onto it.
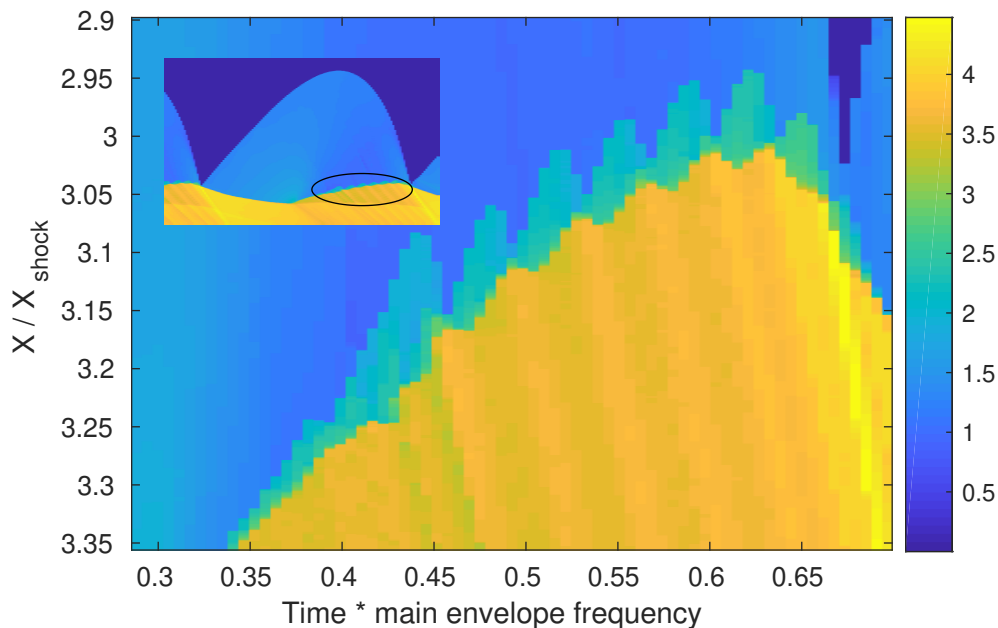
Figure 54. A 'baby shock' formed inside the main envelope, imaged in $\log(\rho)$. This one is from a shock with M=5 and $\theta = -1$, and itself oscillates in the F mode. Where the main oscillation has a frequency of .26, the baby shock has a frequency of roughly 3, and the luminance spectrum indeed shows a series of peaks in that area which surely correspond to this structure.

Results for $\gamma = 7/5$**.** The results for $\gamma = 7/5$ show that the mode transition boundaries, and the threshold of stability, all move toward the high-M low-θ corner compared to the $\gamma = 5/3$ case. The F mode is complete wiped out; Only near $M = 10, \theta = -1$ is even a hint of the F mode seen (the beginning of the 'intermodulation' seen between the F and 1O modes for $\gamma = 5/3$). The relative behaviors when viewed alongside the $\gamma = 5/3$ transition suggest that F modes might emerge for $\gamma = 7/5$ around $\theta = -1.2$ or so at M=10.
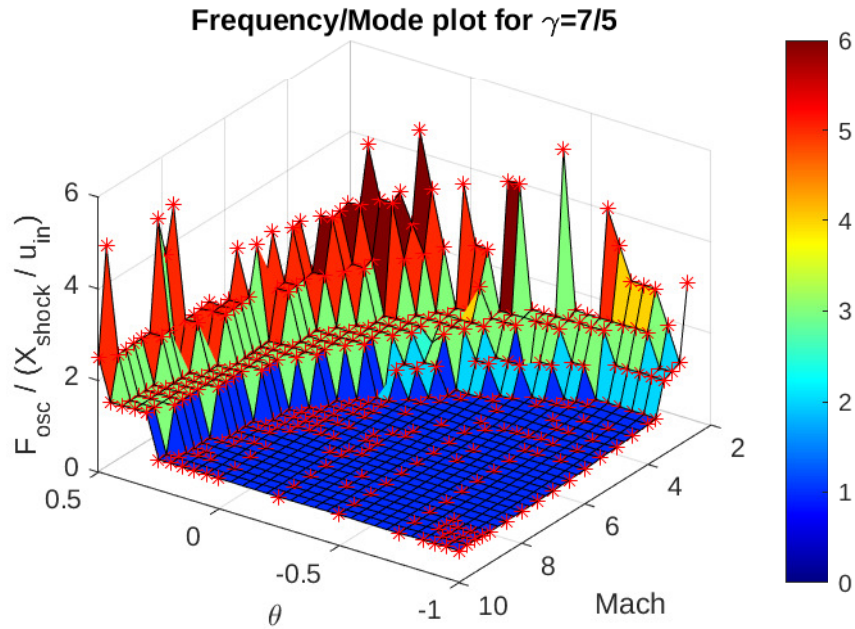
Figure 55. Mode type and frequency plot for $\gamma = 7/5$

The bands occupied by higher oscillation modes grow wider. The 3O band becomes about 2-3 squares wide, which is enough to be a clearly resolved plateau, while the 5O band appears to be about 1 square wide.

As with $\gamma = 5/3$ the preference is overwhelmingly for odd overtones (1O/3O/5O/...). While even overtone frequencies are detectable in spectral analyses, rarely do they form the dominant mode; The few times they do are usually in weaker shocks. This may be the result of a 'phase instability.' An even overtone, in an unfortunate turn of terminology, contains an odd number of waves, which prefer to be separated by $360/N$ degrees of phase.

Figure 56. The luminance fluctuation in the dominant mode for $\gamma = 7/5$. Left: 3D surface. Right: Contour graph in intervals of .1.

The 3rd overtone plateau is observably wide for $\gamma = 7/5$. Unlike the F to 1O transition for $\gamma = 5/3$, this mode change is associated with a distinct step down in luminance power at the tone frequency. For strong shocks, this stepdown is from approximately 30% amplitude to approximately 20% amplitude.

Results for $\gamma = 9/7$**.** Oscillation modes and thresholds for instability again shift up in M and down in θ. Instability at high θ values is very difficult to find: Even at $M = 9$ the largest θ to exhibit instability is 0.2, extending only to 0.25 at $M = 10$. This is in keeping with the general trend that increasing the internal energy content available renders cooling induced instability less likely by lengthening the cooling time. As with $\gamma = 7/5$, the preference for odd overtones is overwhelming.
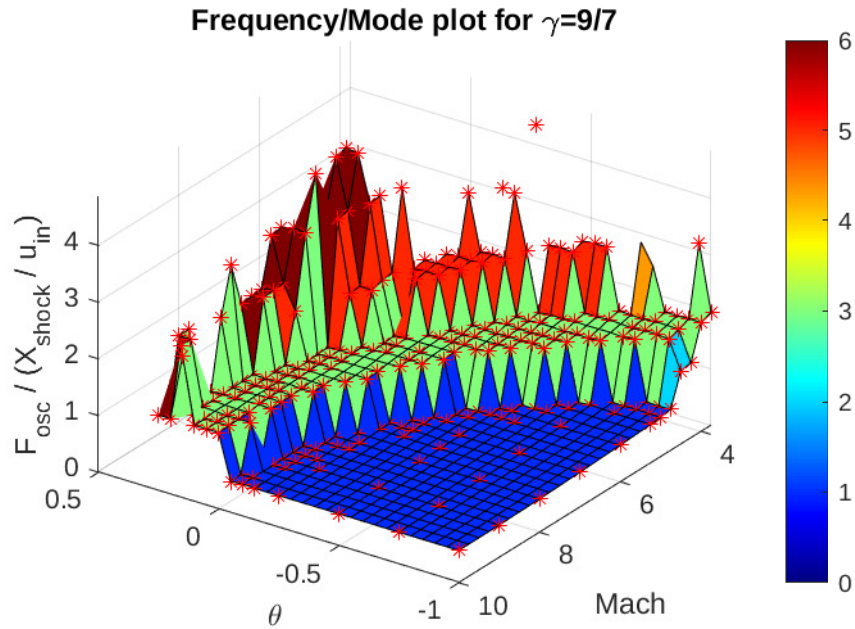
Figure 57. Mode type and frequency plot for $\gamma = 9/7$

The $\gamma = 9/7$ data yields several well-resolved step functions in the shock oscillation frequency, position modulation amplitude and integrated luminance, going from 1O to 3O to 5O (and from there to 7O and higher modes).

As with $\gamma = 7/5$, the luminance fluctuation jumps down as the mode number goes up in addition to the smooth decrease associated with increasing θ. Strong shocks changing from 1st to 3rd to 5th mode oscillation see the luminance fluctuation drop from roughly 30% to 20% to 10%.

It is somewhat more difficult to ascribe the behavior of $\gamma = 9/7$ runs to single monochromatic oscillations, however, as they have a much more marked tendency to exhibit oscillation in multiple modes when saturated.
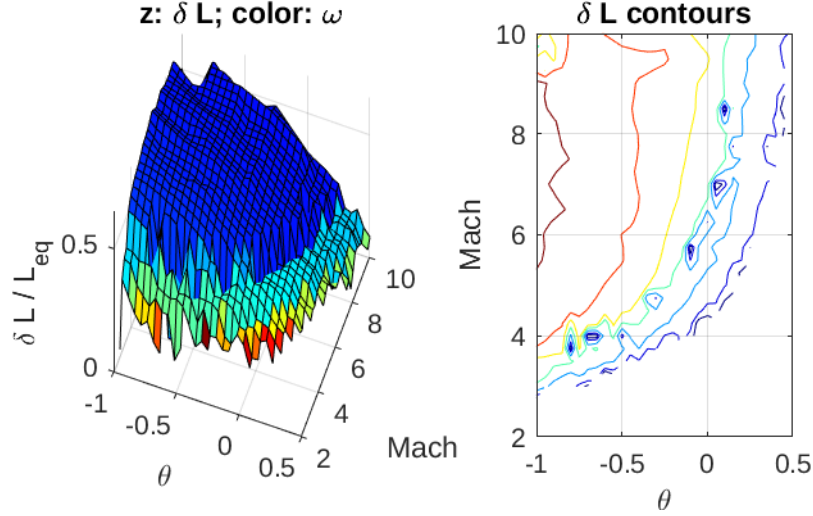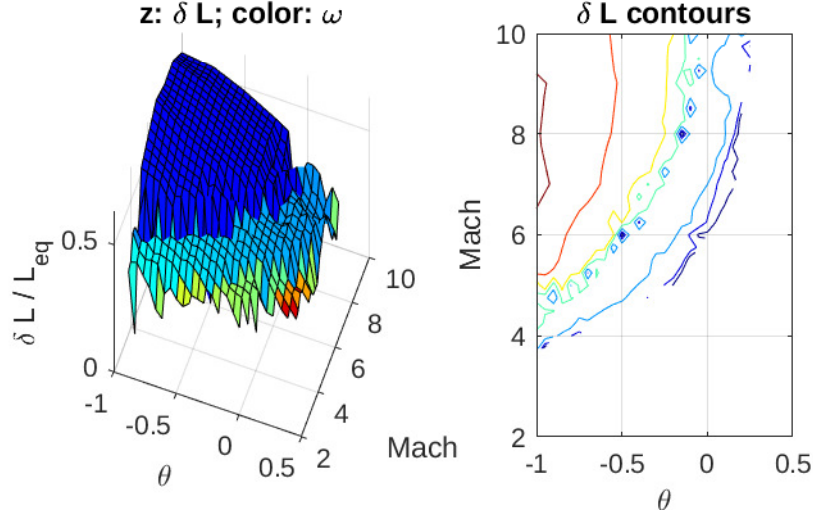
Figure 58. The luminance fluctuation in the dominant mode for $\gamma = 9/7$. Left: 3D surface. Right: Contour graph in intervals of .1.

Observables for radiating planar shocks. From Gehrels and Williams (1993), the basic takeaway for us is that plasma temperatures exceeding roughly 10^5K up to about 5×10^8K in cosmic gas are all characterized by local radiation temperature dependence exponents θ in $\Gamma \propto n^2 T^\theta$ which range from values as high as about 0.4 to ones as low as -1. We find that gas shocks, especially strong shocks which would generate such temperatures to begin with, are nearly always unstable to radial oscillations of some form under these conditions.

We also note that for temperatures below about 1 or $2 \times 10^5 K$ the radiation rate is a very strongly increasing function of T ($\theta > 2$) such that gas shocks under these conditions should be stable against radial oscillations.

According to Gehrels and Williams (1993), shock temperatures above roughly 2×10^7K will be primarily emitting bremsstrahlung continuum radiation while those below are dominated by line emission, while the emissivity near

178

2×10^7K itself is nearly constant ($\theta \approx 0$). In the line range, Fe and Si emission characteristics should be detectable, and these are in fact responsible for the fluctuations in the overall $\theta = -1$ trend at "intermediate" temperatures.

Observations of 2D planar shock simulations. Several simulations of two dimensional planar shocks were performed to determine their susceptibility to transverse structure formation in the nonlinear regime. Shocks with relatively modest resolution requirements were chosen, and the following three parameter points were tested: M=6, $\theta = -.5$, $\gamma = 5/3$ as a representative clean F mode. M=6, $\theta = 0$, $\gamma = 5/3$ as the representative 1O mode. M=6, $\theta = 0.1$, $\gamma = 7/5$ as the repesentative 3O mode.

These simulations were run at a longitudnal resolution 2048 (512 shock cells) and a transverse resolution 10240 (5:1 box aspect). The wide box aspect is necessitated because from dimensional analysis $k_y \approx k_x$ and there is no reason to assume k_y is preferred to be substantially larger than k_x. As the linear wavelength of the F mode is 4 times the length of the cooling column, even a 5:1 aspect may be suspected of quantizing the available wave modes.

Fully 3D simulations would naturally be preferred but the required resolution could not be accomodated with available resources. Even if the transverse grid spacing were doubled so that only 5000 transverse cells were needed, this would in 3D result in a 2000x5000x5000 = 50 billion cell grid and the simulations would emit around 5-10PB of data each.

It is found that the F mode simulation picks the N=1 deformation, the lowest that is permitted by the circular boundary conditions in the Y direction. The 1O oscillator picks the N=2 transverse mode, indicating adequate transverse resolving power. The 3O oscillator shows some signs of structure growth at a

transverse wavenumber N=14, but after the time necessary for the F and 1O simulations to dissolve into complete turbulence, the amplitude of the transverse structure in the 3O mode remains *extremely* small (pressure fluctuations roughly .2%).

The generalized expectation is that the observable (volume-integrated) luminosity fluctuation will be far smaller in oscillations with $k_\perp \neq 0$, as components that are 180 degrees out of phase will mostly or entirely cancel.

In both the F and 1O oscillations, in their linear phase, the transverse structure indeed appears to take on a form resembling

$$\psi(x, y, t) = \psi_{1D}(x, t + a(t)\sin(k_y y)) \tag{6.46}$$

Meaning that we simply observe the 1D function, with a slowly growing phase difference across it width. This most visibly manifested when visualized as the sinusoidal bowing of the shock front, and in turn as the warping of the originally straight lines of the sound waves emitted into the cold layer.

The curvature of the shock front, alone, introduces $v_\perp$ where none existed before. Of course transverse momentum is conserved so that on average there is none, which is also why the bowing of the shock takes the form of a standing wave. However, this alone is not enough to cause the observed turbulence in the cold layer.

The key element relates to the reflection of the (curved) shock off of the cold layer. When the amplitude function $a(t)$ referred to above is small, each reflection inverts the phase of the entire bow. This is simple to see: The part advanced "forward in time" will be further down, rebound first, and be moving up while the delayed part is still falling down. This is depicted schematically and with images of the actual simulation in figure 59.
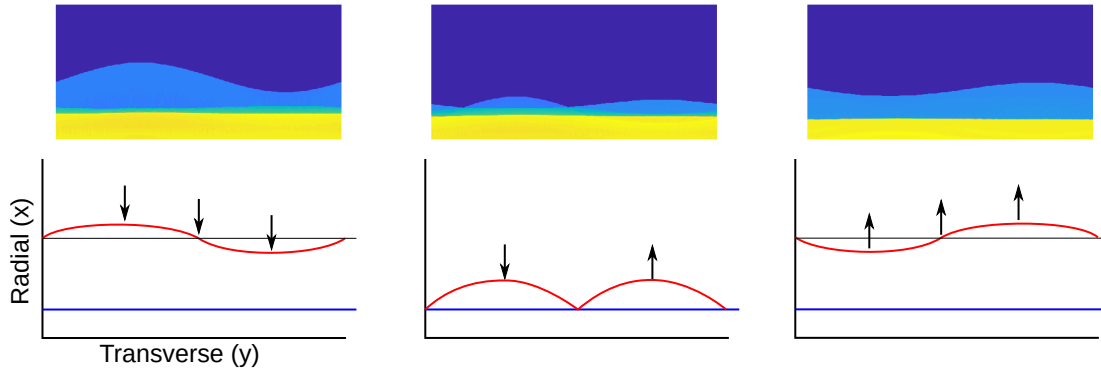
Figure 59. Image of the bow shock and the reversal of the displacement phase when the sinusoidally curved cooling layer collapses onto and rebounds off of the cold layer. The angled shock front at the nodes of the sinusoid creates v_y there that blows sideways across the cold layer, seeding turbulence formation

Through this early part of this process, the cold layer remains "indifferent." The displacement velocity caused by a given momentum impact scales as $1/\rho$, and the cold layer (at the tested parameters of $M = 6$) is roughly 50 times denser than the preshock gas. Thus it experiences only a very small warping.

However, as the amplitude $a(t)$ grows and the out-of-phase parts of the shock become effectively further displaced from each other in time, the impact of the curved shock fronts causes a dramatic nonlinear effect.

It is well known that the streamlines of gas impacting an oblique shock bend away from the normal. To see why, consider simply that normal *momentum* is conserved while transverse *velocity* is conserved. The fact that this deflects gas away from peaks and into valleys leads directly to the unconditional stability of the ideal hydrodynamic shock.

The nodes of the warping of the shock front are the locations of maximum angle, and these lead to the strongest sideways wind ($v_\perp$) occuring there when the shock rebounds. In the same way a gale blowing across a body of water drives

181

waves across the water, this sideways wind drives up Kelvin-Helmholtz turbulence at the boundary of the cold layer.

Meanwhile at the maxima of the bowing, the quasi one dimensional oscillation continues (with an ever growing phase discrepancy at alternating maxima) as if nothing else were going on.

The turbulence at the cold boundary damps as the shock front rebounds, and there apparently exists a critical amplitude $a(t) = a_{\text{crit}}$ below which the resulting wave/vorticity generation damps away between each oscillation cycle and above which self-sustaining turbulence is induced.

The self-sustaining turbulence generally "bursts" and begins destroying the planarity of the cold boundary after a vortex stands about its own radius above the mean cold layer boundary. This is enough that the impact of the angled shock upon the curved density boundary generates a massive amount of vorticity due to $(\nabla \rho) \times (\nabla P)$. Afterwards, the curvature of the cold layer and the incoming cooling layer begin generating their own turbulence via the Kelvin-Helmholtz shearing mechanism, and this continues to power the complete disruption of the cold layer even after the destruction of the smooth wave-reflecting cold boundary causes all shock oscillation to shut down.

There does not appear to be any clear bound on the growing random displacement of the cold layer. Both the F mode and 1O mode simulations were ultimately ended because the distance from the top of the adiabatic shock to the bottom of the cooling layer were nearly as large as the height of the grid, where the equilibrium height of both shocks was one quarter the height of the grid.
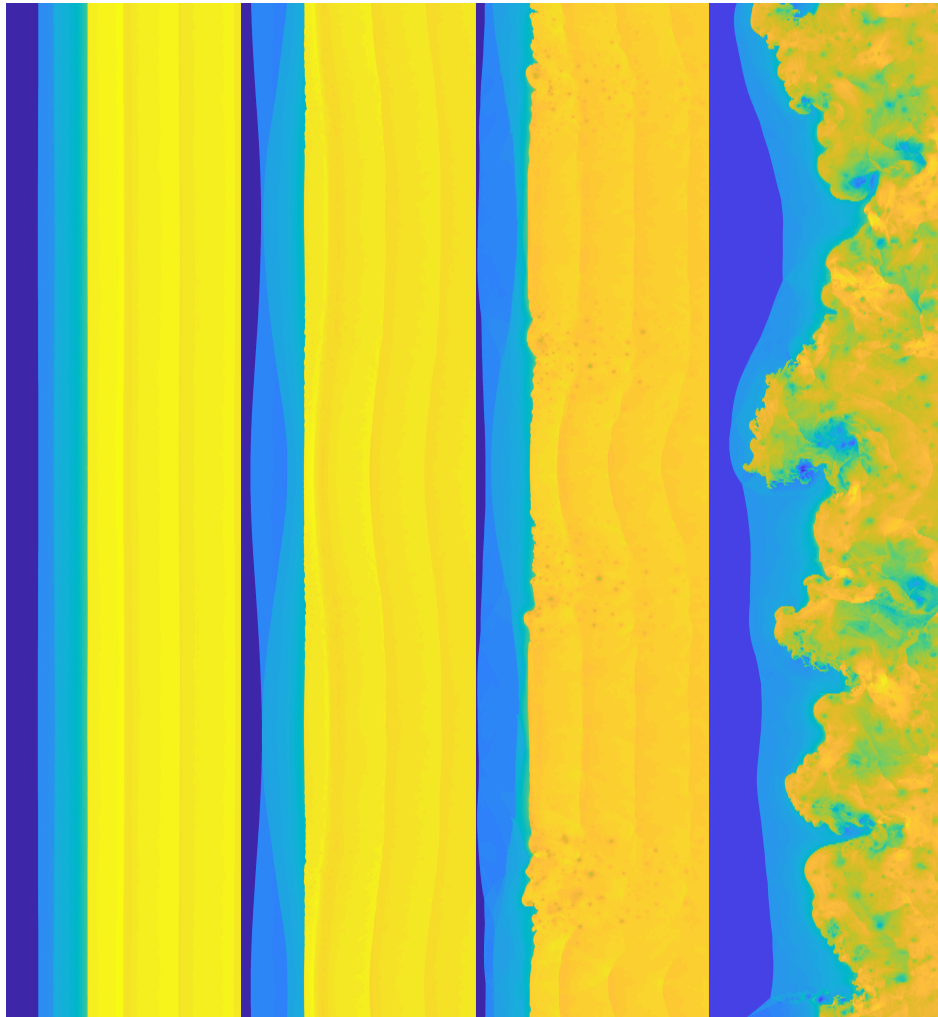
Figure 60. Four snapshots of $\log(\rho)$ of the 1st overtone 2D simulation's descent into chaos. Left: $45t_{\mathrm{cool}}$, with only a few signs of out-of-phase oscillation. 2nd: $102t_{\mathrm{cool}}$, with a clear transverse structure. 3rd: $127t_{\mathrm{cool}}$, the sideways (vertical) winds from the oblique shock impacts at the nodes of the standing transverse structure are generating Kelvin-Helmholtz turbulence. Last: $156t_{\mathrm{cool}}$, the cold layer has dissolved into turbulence and all coherent oscillation has shut down.
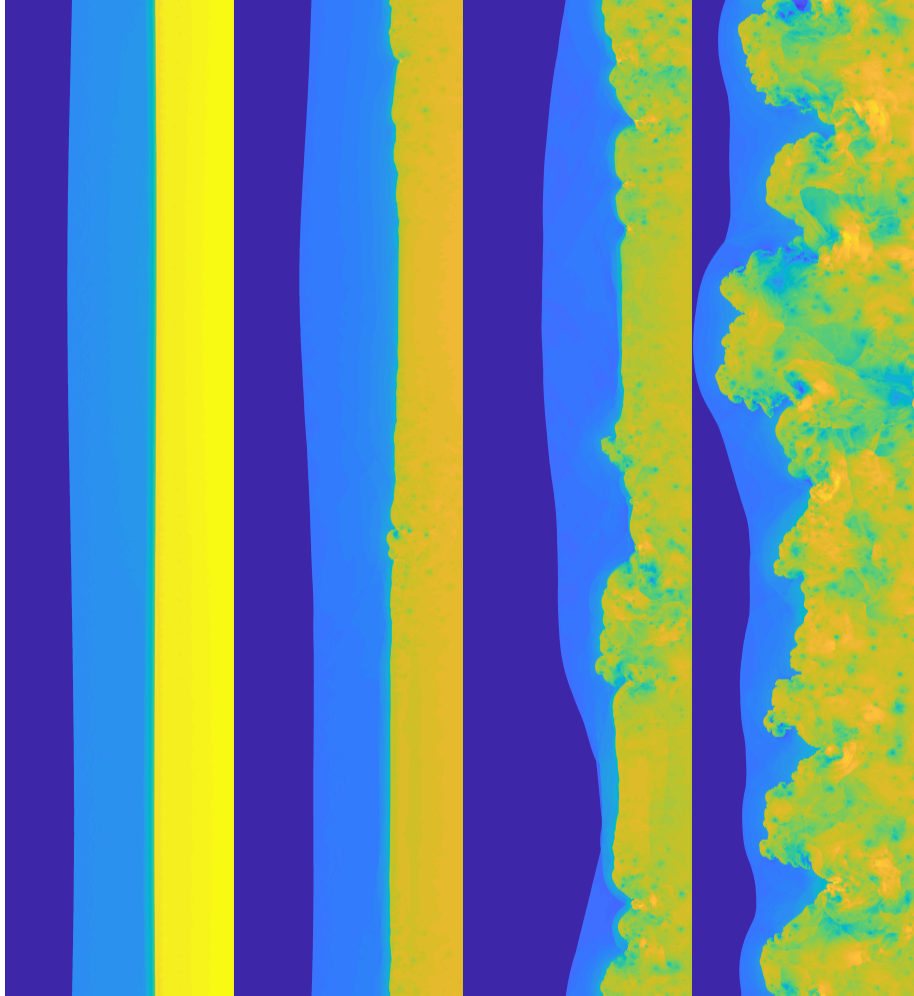
Figure 61. Four snapshots of $\log(\rho)$ of the F mode 2D simulation's descent into chaos. From left to right, after 69, 84, 96 and 113 t_{cool}. First the bowing in the $n_y = 1$ mode becomes apparent. Once the bowing reaches appreciable amplitude, the (here) vertical winds created by the angled shock front whips up Kelvin-Helmholtz turbulence. Areas over the roughly flat part of the cold boundary determinedly try to keep oscillating. The disruption of the cold layer shuts down all oscillation.
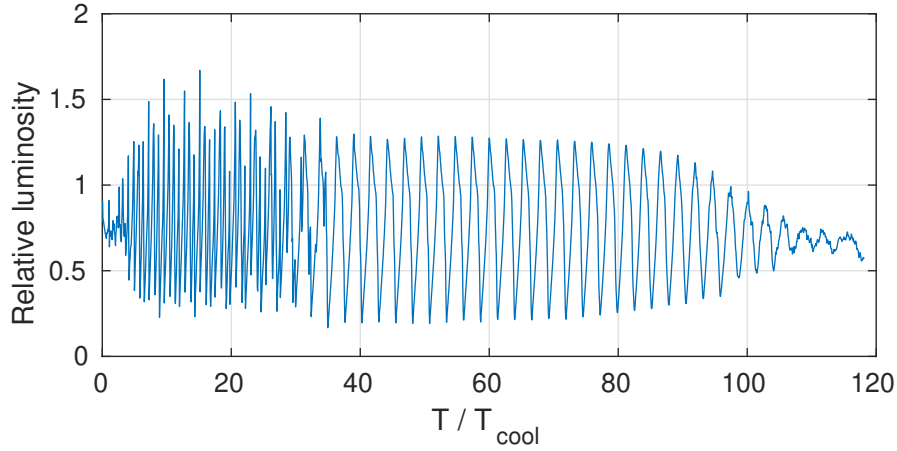
Figure 62. Plot of the luminosity fluctuation of an F mode shock simulated in 2D for 105 cooling times. Starting from a gently salted equilibrium, the planar $(n_y = 0)$ F mode oscillation takes $35t_{cool}$ to reach its full amplitude. An $n_y = 1$ structure begins growing and at roughly $75t_{cool}$ it begins to drive the formation of turbulence in the cold layer. After the outbreak of full turbulence, coherent oscillation shuts down quickly.
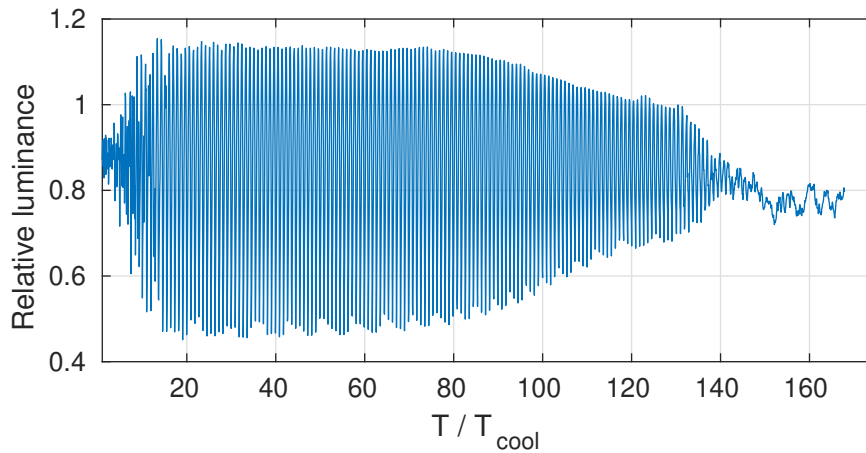
Figure 63. Plot of the luminosity fluctuation of a 1st overtone shock simulated in 2D for 167 cooling times. Starting from a gently salted equilibrium, the planar $(n_y = 0)$ 1st overtone oscillation rings up in about 15 T_{cool}. The loss of luminance to the out-of-phase $(n_y = 2)$ oscillation takes off around $80t_{cool}$. The out-of-phase component eats into the integrated fluctuation until around $130t_{cool}$ at which point the disruption of the cold layer shuts down coherent oscillation completely.

Both the F and 1O simulations grow clear transverse structure, and it was not too difficult to run them far enough to watch both descend into turbulence. The 3O simulation is a different character entirely. There is definite evidence that some transverse structure is growing (with a transverse wavenumber around $N = 14$), however it appears that it will require several million iterations to reach an amplitude of even a few percent, let alone nonlinearity. The planar 3O mode in this simulation, it is worth noting, required a similar time just to reach its own saturation.

The much reduced susceptibility of the higher overtones to transverse structure formation and its inducement of turbulence suggests that if the adiabatic index of the cooling region could be surpressed enough to compel 3O oscillation, this could yield at least intermittent coherent oscillation of a strong shock.

Tests of a global 3D model. Three 3D bow shock simulations were performed. One had no radiation, and exhibited the essentially stable structure that was expected, outside of the Kelvin-Helmholtz instability in the shearing layer. The radiating simulations had two very different radiation laws - one proportional to $T^{.5}$ and one proportional to $T^{-0.5}$. While the two radiating simulations were quantitatively different in both the intensity and period of instability caused by the radiation, the simple presence or absence of radiation (when the radiation timescale was comparable to the flow timescale) caused a fundamental *qualitative* change towards quasiperiodic instability of the bow layer.

The simulations were performed at resolutions of 768^3 (450 million voxels) on two nodes with 2 K80 processor cards each, achieving a simulation rate of .45 steps per second.

Equilibrium structure. In all three cases, the initial non-equilibrium initially evolved towards a time-independent equilibrium structure.

Subsolar point
(saddle point
in flow)

Equilibrium bow size
is smaller with radiation

Shock heated termination
region maintains pressure
support

Cooling loss leads to
shear layer becoming
cold, dense layer
(secularly converging
flow lines exaggerated)

Leading shock
Shear discontinuity
Inner shock
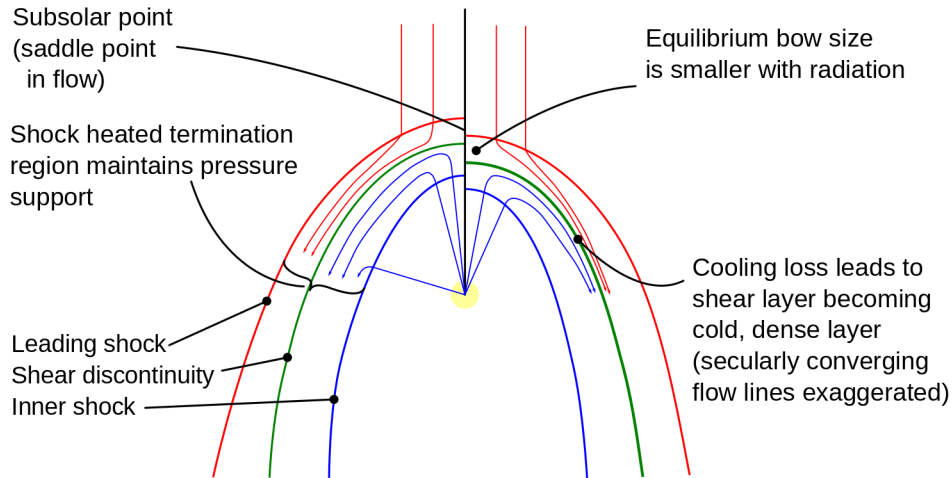
Figure 64. Qualitative diagram depicting differences in the equilibrium structures of radiating vs nonradiating bow shocks.

This equilibrium structure consists inside of a simple adiabatic radial outflow as a simplistic model of a stellar wind. This collides with the inner shock where the outflow drops to subsonic speed, and (in the areas facing the oncoming flow) stop and begin flowing away from the subsonic point.

The inner and outer shocked gas shells are in contact and fall sideways at different speeds, creating a Kelvin-Helmholtz unstable shearing layer between them.

Both radiating and nonradiating bows form similar structures dynamically, best described by the pressure structures. Radially, pressure is maximal at the subsolar point, with a strong gradient direction away from the shearing layer serving to brake the progress of gas towards the shearing layer. In the transverse

187

direction, a pressure gradient points away from the subsolar point (which thus has the maximum pressure obtained), serving to cause fluid to accelerate away from the subsolar point and avoiding endless accumulation of gas there.

Radiating flows exhibit a comparatively secular formation of a very thin cold layer near the subsonic point where fluid resides long enough to cool.

Behavior of nonradiative bow flow. When the bow flow is not let to radiate, the only source of instability is the KH instability of the shearing layer. This is indeed seen to waver and emit rolling structures (which in real conditions would correspond to the turbulent mixing layer), however there is no larger-scale instability nor is there any periodicity to the overturning eddies other than their own circulation rate.

That is, the inner/outer shock structure is never substantially disturbed by the rolling eddies and turbulence in the shearing layer.

Behavior of radiative bow flows. The ratio of import for the radiating simulations is the radiation cooling time divided by the flow time. If radiation is slow, the limit of a simple nonradiative simulation is approached because no internal energy is lost before the flow moves off the grid.

Ultimately, the origin of the unstable behavior is the _subsolar point._ If outflow is uniformly radially away from the star, and oncoming flow is uniform, then the line connecting the outflow and incoming flow lines traces a saddle point of the velocity field: A particle flowing along the axis nominally becomes trapped at the subsolar point, and gas near there resides there for a relatively long time.

Dynamically, the equilibrium flow always holds itself in pressure balance. If radiation causes the temperature of the shocked layer to drop, then the density of the middle of the shocked layer - the shearing layer - must increase in order to

maintain pressure suppport. The extent of this density increase becomes greater and greater approaching the subsolar point, where gas can have a much longer residence time.

In both radiating simulations, the subsolar point is observed to eventually accumulate a very dense knot of matter that undergoes runaway cooling, such that it can essentially "wander" without being pushed back against by pressure - as any gas that it absorbs cools immediately.

As long as it remains inside the shocked region, it does not fundamentally destabilize the system. However the moment its curved surface makes contact with either shock front, the ram pressure imparts a large torque (c.f. Richtmeyer-Meshkov instability). This initiates a cascade of intense dynamic turbulence as the pressure-sapping cold layer is disrupted and spread.

The chaotic, turbulent flow appears to continue for as long as there are any dense, pressure-sapping knots of matter within the bow region to power it. Once the existing knots drift away or are disrupted (and the turbulent flow prevents the formation of new ones), the turbulence dies away and the original largely laminar stable bow re-emerges and settles into an equilibrium form again, after which the cold dense layer can then be seen to re-emerge.

Both radiating simulations ran long enough to observe multiple cycles of this: Disruption of the laminar bow structure, dissolution of the bow region into turbulence, followed by clearing and reformation of the stable bow.

These observations were made possible by visualizating the output data, amounting to roughly 6TB per simulation, using the **Paraview** 3D parallel visualization system.
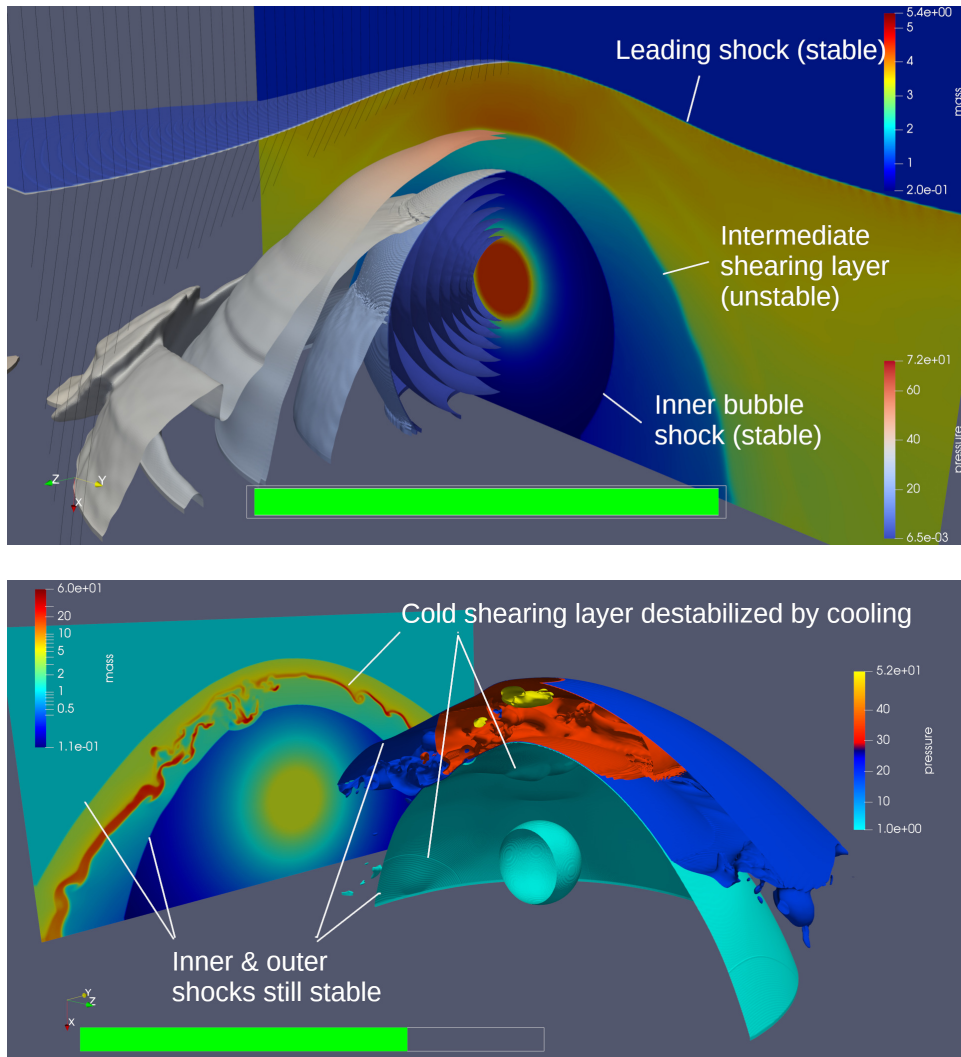
Figure 65. Quantitative difference between radiating and nonradiating simulations. Radiating simulations form a cold gas layer which eventually destabilizes near the subsolar point and totally disrupts the otherwise relatively stable bow structure that forms.

REFERENCES CITED

Allen, M. D., & Raabe, O. G. (1985, Jan). Slip Correction Measurements of Spherical Solid Aerosol Particles in an Improved Millikan Apparatus. *Aerosol Science and Technology*, *4*(3), 269–286. Retrieved from `http://dx.doi.org/10.1080/02786828508959055` doi: 10.1080/02786828508959055

Armitage, P. J. (2011, Sep). Dynamics of Protoplanetary Disks. *Annual Review of Astronomy and Astrophysics*, *49*(1), 195–236. Retrieved from `http://dx.doi.org/10.1146/annurev-astro-081710-102521` doi: 10.1146/annurev-astro-081710-102521

Batten, P., Clarke, N., Lambert, C., & Causon, D. M. (1997, Nov). On the Choice of Wavespeeds for the HLLC Riemann Solver. *SIAM Journal on Scientific Computing*, *18*(6), 1553–1570. Retrieved from `http://dx.doi.org/10.1137/S1064827593260140` doi: 10.1137/s1064827593260140

Blondin, J. M., Wright, E. B., Borkowski, K. J., & Reynolds, S. P. (1998, June). Transition to the Radiative Phase in Supernova Remnants. *The Astrophysics Journal*, *500*, 342–354. doi: 10.1086/305708

Brown, P. P., & Lawler, D. F. (2003, Mar). Sphere Drag and Settling Velocity Revisited. *Journal of Environmental Engineering*, *129*(3), 222–231. Retrieved from `http://dx.doi.org/10.1061/(ASCE)0733-9372(2003)129:3(222)` doi: 10.1061/(asce)0733-9372(2003)129:3(222)

Caliari, M., & Ostermann, A. (2009, Mar). Implementation of exponential Rosenbrock-type integrators. *Applied Numerical Mathematics*, *59*(3-4), 568–581. Retrieved from `http://dx.doi.org/10.1016/j.apnum.2008.03.021` doi: 10.1016/j.apnum.2008.03.021

Chapman, S., Cowling, T. G., & Park, D. (1962, May). The Mathematical Theory of Non-Uniform Gases. *American Journal of Physics*, *30*(5), 389–389. Retrieved from `http://dx.doi.org/10.1119/1.1942035` doi: 10.1119/1.1942035

Chevalier, R. A., & Imamura, J. N. (1982, October). Linear analysis of an oscillatory instability of radiative shock waves. *The Astrophysical Journal*, *261*, 543–549. doi: 10.1086/160364

Colella, P., & Woodward, P. R. (1984, September). The Piecewise Parabolic Method (PPM) for Gas-Dynamical Simulations. *Journal of Computational Physics*, *54*, 174–201. doi: 10.1016/0021-9991(84)90143-8

Cunningham, E. (1910, Mar). On the Velocity of Steady Fall of Spherical Particles through Fluid Medium. *Proceedings of the Royal Society A: Mathematical, Physical and Engineering Sciences*, *83*(563), 357–365. Retrieved from `http://dx.doi.org/10.1098/rspa.1910.0024` doi: 10.1098/rspa.1910.0024

Dumbser, M., Moschetta, J.-M., & Gressier, J. (2004, Jul). A matrix stability analysis of the carbuncle phenomenon. *Journal of Computational Physics*, *197*(2), 647–670. Retrieved from `http://dx.doi.org/10.1016/j.jcp.2003.12.013` doi: 10.1016/j.jcp.2003.12.013

Einfeldt, B. (1988, Apr). On Godunov-Type Methods for Gas Dynamics. *SIAM J. Numer. Anal.*, *25*(2), 294–318. Retrieved from `http://dx.doi.org/10.1137/0725021` doi: 10.1137/0725021

G. Stokes, G. (1850, 11). On the Effect of Internal Friction of Fluids on the Motion of Pendulums. *, 9*.

Gehmeyr, M., Cheng, B., & Mihalas, D. (1997, Oct). Noh's constant-velocity shock problem revisited. *Shock Waves*, *7*(5), 255–274. Retrieved from `http://dx.doi.org/10.1007/s001930050081` doi: 10.1007/s001930050081

Gehrels, N., & Williams, E. D. (1993, November). Temperatures of Enhanced Stability in Hot Thin Plasmas. *The Astrophysical Journal*, *418*, L25. doi: 10.1086/187107

Godunov, S. K., & Ryabenki, V. (1964). *Theory of Difference Schmes.* North Holland.

Gresho, P. M. (1991). Incompressible fluid dynamics - Some fundamental formulation issues. *Annual Review of Fluid Mechanics*, *23*, 413–453. doi: 10.1146/annurev.fl.23.010191.002213

Harten, A. (1983, March). High Resolution Schemes for Hyperbolic Conservation Laws. *Journal of Computational Physics*, *49*, 357–393. doi: 10.1016/0021-9991(83)90136-5

Harten, A., Lax, P. D., & Leer, B. v. (1983, Jan). On Upstream Differencing and Godunov-Type Schemes for Hyperbolic Conservation Laws. *SIAM Review*, *25*(1), 35–61. Retrieved from `http://dx.doi.org/10.1137/1025002` doi: 10.1137/1025002

Hyman, J. M., & Larrouturou, B. (1982, Jan). The numerical differentiation of discrete functions using polynomial interpolation methods. *Applied Mathematics and Computation*, *10-11*, 487–506. Retrieved from `http://dx.doi.org/10.1016/0096-3003(82)90204-1` doi: 10.1016/0096-3003(82)90204-1

Imamura, J. N., Wolff, M. T., & Durisen, R. H. (1984, Jan). A numerical study of the stability of radiative shocks. *The Astrophysical Journal*, *276*, 667. Retrieved from `http://dx.doi.org/10.1086/161654` doi: 10.1086/161654

Kamm, J. R. (2000). Evaluation of the Sedov-von Neumann-Taylor Blast Wave Solution.

Kamm, J. R., & Timmes, F. X. (2007). *On efficient Generation of Numerically Robust Sedov Solutions* (Tech. Rep.).

Kennedy, C. A., Carpenter, M. H., & Lewis, R. (2000, Nov). Low-storage, explicit Runge–Kutta schemes for the compressible Navier–Stokes equations. *Applied Numerical Mathematics*, *35*(3), 177–219. Retrieved from `http://dx.doi.org/10.1016/S0168-9274(99)00141-5` doi: 10.1016/s0168-9274(99)00141-5

Ketcheson, D. I. (2008, Jan). Highly Efficient Strong Stability-Preserving Runge–Kutta Methods with Low-Storage Implementations. *SIAM Journal on Scientific Computing*, *30*(4), 2113–2136. Retrieved from `http://dx.doi.org/10.1137/07070485X` doi: 10.1137/07070485x

Laibe, G., & Price, D. J. (2011a, November). *Dusty gas with SPH - I. Algorithm and test suite.* Retrieved from `http://arxiv.org/abs/1111.3090v1;http://arxiv.org/pdf/1111.3090v1` doi: 10.1111/j.1365-2966.2011.20202.x

Laibe, G., & Price, D. J. (2011b, November). *Dusty gas with SPH - II. Implicit timestepping and astrophysical drag regimes.* Retrieved from `http://arxiv.org/abs/1111.3089v1;http://arxiv.org/pdf/1111.3089v1` doi: 10.1111/j.1365-2966.2011.20201.x

Laibe, G., & Price, D. J. (2014, October). Dust and gas mixtures with multiple grain species - a one-fluid approach. *Monthly Notices of the Royal Astronomical Society*, *444*, 1940–1956. doi: 10.1093/mnras/stu1367

Liska, R., & Wendroff, B. (2003, Jan). Comparison of Several Difference Schemes on 1D and 2D Test Problems for the Euler Equations. *SIAM Journal on Scientific Computing*, *25*(3), 995–1017. Retrieved from `http://dx.doi.org/10.1137/S1064827502402120` doi: 10.1137/s1064827502402120

Mannel, T., Bentley, M. S., Schmied, R., Jeszenszky, H., Levasseur-Regourd, A. C., Romstedt, J., & Torkar, K. (2016, November). Fractal cometary dust – a window into the early Solar system. *Monthly Notices of the Royal Astronomical Society*, *462*(Suppl 1), S304–S311. doi: 10.1093/mnras/stw2898

Meru, F., Juhasz, A., Ilee, J. D., Clarke, C. J., Rosotti, G. P., & Booth, R. A. (2017, March). *On the origin of the spiral morphology in the Elias 2-27 circumstellar disc.* Retrieved from `http://arxiv.org/abs/1703.05338v1;http://arxiv.org/pdf/1703.05338v1` doi: 10.3847/2041-8213/aa6837

Moler, C., & Van Loan, C. (2003, Jan). Nineteen Dubious Ways to Compute the Exponential of a Matrix, Twenty-Five Years Later. *SIAM Review*, *45*(1), 3–49. Retrieved from `http://dx.doi.org/10.1137/S00361445024180` doi: 10.1137/s00361445024180

Pringle, J. E. (1981). Accretion discs in astrophysics. *Astronomy & Astrophysics Annurev*, *19*, 137–162. doi: 10.1146/annurev.aa.19.090181.001033

Robertson, H. P., & Russell, H. N. (1937, Apr). Dynamical Effects of Radiation in the Solar System. *Monthly Notices of the Royal Astronomical Society*, *97*(6), 423–437. Retrieved from `http://dx.doi.org/10.1093/mnras/97.6.423` doi: 10.1093/mnras/97.6.423

Roe, P. (1981, Oct). Approximate Riemann solvers, parameter vectors, and difference schemes. *Journal of Computational Physics*, *43*(2), 357–372. Retrieved from `http://dx.doi.org/10.1016/0021-9991(81)90128-5` doi: 10.1016/0021-9991(81)90128-5

Saffman, P. G. (1965, Jun). The lift on a small sphere in a slow shear flow. *Journal of Fluid Mechanics*, *22*(02), 385. Retrieved from `http://dx.doi.org/10.1017/S0022112065000824` doi: 10.1017/s0022112065000824

Schure, K. M., Kosenko, D., Kaastra, J. S., Keppens, R., & Vink, J. (2009, October). A new radiative cooling curve based on an up-to-date plasma emission code. *Astronomy & Astrophysics*, *508*(2), 751–757. doi: 10.1051/0004-6361/200912495

Shu, C.-W., & Osher, S. (1989, Jul). Efficient implementation of essentially non-oscillatory shock-capturing schemes, II. *Journal of Computational Physics*, *83*(1), 32–78. Retrieved from `http://dx.doi.org/10.1016/0021-9991(89)90222-2` doi: 10.1016/0021-9991(89)90222-2

Sod, G. A. (1978, April). A survey of several finite difference methods for systems of nonlinear hyperbolic conservation laws. *Journal of Computational Physics*, *27*, 1–31. doi: 10.1016/0021-9991(78)90023-2

Stokes, G. G. (1851). *On the effect of the internal friction of fluids on the motion of pendulums* (Vol. 9 part ii). Pitt Press Cambridge.

Strang, G. (1968, September). On the Construction and Comparison of Difference Schemes. *SIAM Journal on Numerical Analysis*, *5*, 506–517. doi: 10.1137/0705041

Strickland, R., & Blondin, J. M. (1995, Aug). Numerical Analysis of the Dynamic Stability of Radiative Shocks. *The Astrophysical Journal*, *449*, 727. Retrieved from `http://dx.doi.org/10.1086/176093` doi: 10.1086/176093

Sweby, P. K. (1984, October). High Resolution Schemes Using Flux Limiters for Hyperbolic Conservation Laws. *SIAM Journal on Numerical Analysis*, *21*, 995–1011. doi: 10.1137/0721062

Takahashi, K., & Yamada, S. (2013, October). *Exact Riemann solver for ideal magnetohydrodynamics that can handle all types of intermediate shocks and switch-on/off waves.* Retrieved from `http://arxiv.org/abs/1310.2330v1;http://arxiv.org/pdf/1310.2330v1` doi: 10.1017/S0022377813001268

Toomre, A. (1964, May). On the gravitational stability of a disk of stars. *The Astrophysical Journal*, *139*, 1217. Retrieved from `http://dx.doi.org/10.1086/147861` doi: 10.1086/147861

Toro, E. F., Spruce, M., & Speares, W. (1994, Jul). Restoration of the contact surface in the HLL-Riemann solver. *Shock Waves*, *4*(1), 25–34. Retrieved from `http://dx.doi.org/10.1007/BF01414629` doi: 10.1007/bf01414629

Tucker, W. H., & Gould, R. J. (1966, April). Radiation from a Low-Density Plasma at $10^{6\circ}$ - $10^{8\circ}$ K. *The Astrophysical Journal*, *144*, 244. doi: 10.1086/148601

van Leer, B. (1982). Flux-vector splitting for the Euler equations. *Lecture Notes in Physics*, 507–512. Retrieved from
`http://dx.doi.org/10.1007/3-540-11948-5_66` doi: 10.1007/3-540-11948-5_66

Vides, J., Nkonga, B., & Audit, E. (2015, Jan). A simple two-dimensional extension of the HLL Riemann solver for hyperbolic systems of conservation laws. *Journal of Computational Physics*, *280*, 643–675. Retrieved from
`http://dx.doi.org/10.1016/j.jcp.2014.10.013` doi: 10.1016/j.jcp.2014.10.013